POLITECNICO DI TORINO

Collegio di Ingegneria Chimica e dei Materiali

Corso di Laurea Magistrale in
Ingegneria Chimica e dei Processi Sostenibili

Tesi di Laurea Magistrale

Methylene Blue removal from wastewater using renewable adsorbent materials

Relatori

Prof.ssa Demichelis Francesca
Prof. Deorsola Fabio Alessandro

Candidata

Chiara Ragusa

Novembre 2023

Riassunto

Numerose industrie, come per esempio quella tessile e cartaria, utilizzano giornalmente elevate quantità di coloranti sintetici, che, rispetto ai coloranti di origine naturale, risultano meno costosi e permettono di ottenere più sfumature di colore. Questo vasto utilizzo porta alla generazione di grandi volumi di acque di scarico, per esempio pari a circa 1-10 milioni di litri al giorno esclusivamente per l'industria tessile di Cina, Regno Unito e Stati Uniti d'America (Hamad & Idrus, 2022). Tali acque, inquinate da coloranti sintetici, non possono essere gestite attraverso l'impiego di trattamenti biologici convenzionali a causa della complessa struttura molecolare dei coloranti utilizzati e della loro natura aromatica, che li rende non biodegradabili.
Inoltre, un'ulteriore sfida consiste nel trovare trattamenti implementabili su larga scala, a basso costo, in grado di evitare la produzione di inquinanti secondari dovuti a reazioni di ossidazione e degradazione, e adatti a rimuovere anche basse concentrazioni di inquinante.

Tra le tecniche alternative più studiate per la rimozione di tali coloranti da effluenti acquosi si annovera in particolare l'adsorbimento, un tipo di trattamento promettente in quanto rispetta i requisiti elencati e presenta alte efficienze di rimozione, un design semplice e facilità di utilizzo con grande adattabilità. La scelta del materiale adsorbente dipende dall'inquinante da rimuovere ed influenza le prestazioni di questo tipo di trattamento.

Nel presente lavoro di tesi, l'inquinante utilizzato è un colorante cationico organico, il Blu di Metilene (MB), che, se rilasciato nell'ambiente, può creare problemi dal punto di vista tossicologico, ambientale ed estetico. A grandi dosi può avere effetti negativi sulla salute e la sua presenza in un corpo idrico può impedire la penetrazione dei raggi solari e ridurne l'ossigenazione. A livello puramente visivo anche piccole dosi, pari a meno di 1 ppm, sono chiaramente percepibili e, dunque, indesiderate. La massima concentrazione rilasciabile è regolamentata da limiti di legge, atti a contenere l'impatto di tale inquinante e a cui gli impianti di trattamento devono sottostare.

Per quanto riguarda il materiale adsorbente, sono stati selezionati diversi materiali innovativi che fossero economici, rinnovabili e non tossici, come il biochar (BC) e l'hydrochar (HC) prodotti a partire da biomassa di scarto. Il carbone attivo commerciale è stato utilizzato come riferimento per la valutazione delle prestazioni; esso, infatti, è un materiale adsorbente ampiamente diffuso, che, nonostante sia molto efficace, presenta degli svantaggi a livello economico riguardo ai costi di produzione, motivo per cui si ricercano materiali sostitutivi non convenzionali e poco costosi.

Il biochar è stato prodotto a partire da lolla di riso tramite pirolisi, un processo di conversione termochimica condotto in assenza di ossigeno. La lolla di riso, proveniente da S.P. S.p.a., è l'involucro esterno dei chicchi di riso che viene generato come sottoprodotto durante la fase di sgranatura dei cereali. La biomassa è stata pesata e poi posta nel reattore di pirolisi in cui, dopo una prima fase di inertizzazione, è stata pirolizzata ad una temperatura di 600 °C per un tempo di residenza pari ad 1 ora sotto un flusso di gas inerte. In particolare, sono state condotte due diverse pirolisi utilizzando azoto ed anidride carbonica come gas inerti, dalle quali sono stati prodotti due tipi di biochar, denominati rispettivamente biochar N_2 e biochar CO_2.

La velocità di riscaldamento di 15 °C/min ha seguito un programma di riscaldamento regolato da un controllore di temperatura PID e, a fine reazione, il residuo solido della biomassa di partenza è stato lavato per rimuovere eventuali impurità e poi essiccato a 105 °C fino al raggiungimento di un peso costante. In questo modo è stato possibile ottenere il biochar desiderato e, in base alla quantità di lolla di riso di partenza, sono state calcolate le rese in peso, rispettivamente di 32,1% e 31,1% per il biochar CO_2 ed N_2.
Le condizioni operative scelte definiscono il tipo di pirolisi: per temperature comprese tra 350 e 700 °C e per velocità di riscaldamento non elevate, si ha una pirolisi *lenta* che, a differenza della pirolisi *flash* e *fast*, permette di ottimizzare la produzione di residuo solido carbonioso, il biochar, a scapito della formazione degli altri prodotti, cioè bio-olio e gas di pirolisi. La velocità di riscaldamento contenuta, infatti, previene lo sviluppo di reazioni di pirolisi secondarie e riduce il rapido rilascio di gas, mentre tempi di residenza lunghi promuovono la ripolimerizzazione dei costituenti del biochar.
Infine, le condizioni operative influenzano anche le proprietà fisico-chimiche del biochar prodotto, come area superficiale, dimensione dei pori, gruppi funzionali e contenuto di carbonio, le quali dipendono anche dalla biomassa iniziale.

L'hydrochar, invece, è il prodotto di una carbonizzazione idrotermale (HTC) condotta a 240 °C per 60 minuti, sempre a partire da lolla di riso. Quest'ultimo è un processo che, a differenza della pirolisi convenzionale, prevede l'utilizzo di acqua subcritica come mezzo reagente. La biomassa è stata sommersa in acqua ad una percentuale di 20% in peso in un sistema confinato, in cui la pressione è stata aumentata, passando da un valore iniziale di 2 barg ad uno finale di 6,5 barg, per mantenere l'acqua allo stato liquido anche per temperature maggiori di 100 °C. Tra i prodotti, oltre all'hydrochar di interesse, si ottiene bio-olio miscelato con acqua, anidride carbonica ed altri prodotti liquidi e gassosi, recuperati separatamente in più fasi. La separazione tra fase acquosa e fase solida è stata effettuata tramite filtrazione, mentre per rimuovere la fase oleosa impregnata nel solido sono stati condotti lavaggi con acetato di etile; infine, il solido è stato essiccato a 105 °C per rimuovere tracce di solvente e poi pesato per determinare la resa in peso rispetto alla biomassa secca di partenza, in questo caso pari al 47,8%.
In caso di utilizzo di biomassa umida in partenza, è evidente un vantaggio rispetto alla pirolisi, in quanto si riesce ad ottenere l'hydrochar senza necessitare di un pretrattamento di essiccazione della biomassa, che spesso risulta energivoro.

Per comprendere meglio le proprietà fisico-chimiche dei materiali adsorbenti ottenuti e il meccanismo di adsorbimento che essi seguono, prima di intraprendere gli esperimenti di adsorbimento sono state impiegate diverse tecniche di caratterizzazione dei materiali.
Il microscopio elettronico a scansione ad emissione di campo (FESEM) permette la visualizzazione di forma e dimensione della struttura porosa del materiale e in questo caso ha messo in evidenza una dimensione dei pori visibili pari a 3 - 8 μm di diametro per entrambi i tipi di biochar, nell'intervallo attribuibile ai macropori. L'hydrochar, invece, presenta una superficie irregolare con pori visibili più piccoli e il carbone attivo mostra blocchi granulari molto fini, con pori non visibili a parità di ingrandimento.
La determinazione dell'area superficiale specifica e della distribuzione della dimensione dei pori, effettuata tramite l'analisi BET, mostra la presenza di micropori in tutti i materiali e dei valori pari a circa 180, 85, 22 e 1460 m^2 di superficie per grammo di materiale adsorbente, rispettivamente biochar

CO_2, biochar N_2, hydrochar e carbone attivo. Da un confronto in letteratura risultano valori conformi, con valori leggermente alti per quanto riguarda il carbone attivo.
L'analisi elementare CHNSO specifica la composizione del campione che, come atteso, presenta una percentuale di carbonio più alta rispetto alla lolla di riso di partenza, con una minor quantità di ossigeno. La composizione di biochar CO_2 e biochar N_2 risulta pressoché identica, con una percentuale lievemente maggiore di ossigeno per il secondo, mentre, paragonandoli con il carbone attivo, quest'ultimo arriva ad avere anche l'80% di carbonio e risulta il meno ossigenato.
In ultima analisi, per capire il meccanismo di adsorbimento è opportuno individuare il pH corrispondente al punto di carica zero (PZC) di ciascun materiale. Se la superficie presenta sia gruppi acidi sia gruppi basici, può possedere carica superficiale positiva o negativa in base al pH della soluzione, che induce la dissociazione di gruppi superficiali. Per questo motivo, gli ioni H+ e OH- sono chiamati *charge determining ions*, in quanto permettono di manipolare la carica superficiale. Quando essa è esattamente pari a zero, significa che il grado di dissociazione acida e basica è lo stesso e la concentrazione di *charge determining ions* corrispondente è definita come PZC. In particolare, se il pH è inferiore al pH corrispondente al PZC, la carica superficiale diventa positiva e gli anioni in soluzione vengono attratti, e viceversa nel caso di pH superiore. Infatti, nel caso dell'adsorbimento di MB questo concetto assume particolare importanza, in quanto esso è un inquinante cationico e si può ottenere un miglioramento nell'efficienza di rimozione rendendo la superficie del materiale adsorbente negativa, portando il pH della soluzione ad un valore superiore al pH del PZC.
Nell'ambito dei materiali studiati, il pH_{PZC} è risultato pari a 8,67 per il carbone attivo, circa 8 per l'hydrochar e circa 9 per entrambe le tipologie di biochar, e diventa una caratteristica molto significativa per quanto riguarda lo studio dell'effetto del pH sull'adsorbimento.

In seguito alla caratterizzazione del materiale, si possono effettuare prove di adsorbimento per correlare le proprietà ricavate con le efficienze di rimozione risultanti dagli esperimenti, di cui devono essere definite le condizioni operative.
Oltre al tipo di materiale adsorbente, la rimozione del Blu di Metilene in soluzione acquosa dipende da diversi fattori, tra cui la concentrazione iniziale del colorante stesso, la concentrazione del materiale adsorbente, la temperatura, il tempo di contatto, la velocità di agitazione e il pH. In questo lavoro di tesi, in particolare, si analizzano gli effetti del dosaggio di adsorbente, del pH e del tempo di contatto. Tutti gli esperimenti sono stati condotti in discontinuo a partire da soluzioni acquose a concentrazione iniziale di Blu di Metilene pari a 50 mg/L, a temperatura ambiente e agitate ad una velocità costante di circa 270 giri al minuto per un totale di 6 h per esperimento, ciascuno condotto in triplicato.
Per la determinazione degli intervalli entro cui far variare i parametri da analizzare è stato effettuato un ampio confronto bibliografico.

L'effetto della concentrazione iniziale di adsorbente è stato studiato usando tre diversi dosaggi (0,25, 0,5 e 1 g/L) per ciascuno dei quattro materiali. La quantificazione della concentrazione residua di Blu di Metilene in soluzione è avvenuta tramite l'impiego di uno spettrofotometro. È stata misurata, infatti, l'assorbanza della soluzione servendosi della retta di taratura dello strumento per ricondursi al valore di concentrazione corrispondente.

I risultati ottenuti sono illustrati in *Figura I*, dove si denota generalmente una correlazione positiva tra rimozione di inquinante e dosaggio di adsorbente.

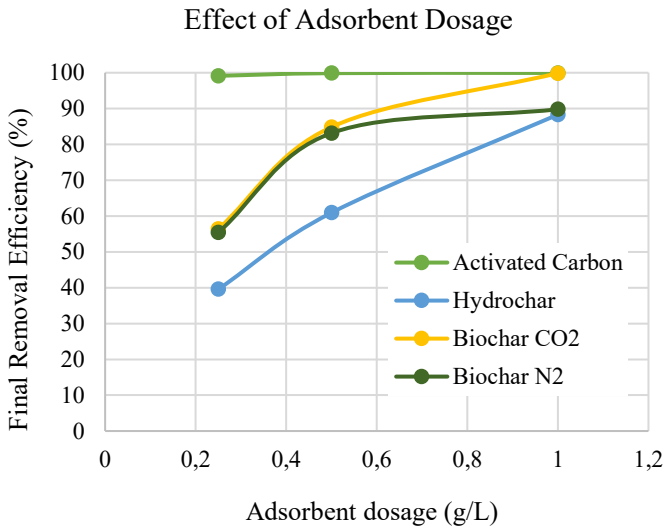

Figura I: Effetto del dosaggio di adsorbente sull'efficienza di rimozione

All'aumentare del dosaggio, l'efficienza di rimozione mostra un aumento graduale dovuto ad una maggiore area superficiale e ad un maggior numero di siti di adsorbimento disponibili sull'adsorbente. Inoltre, l'adsorbimento tende a raggiungere un equilibrio quando uno specifico valore di dosaggio viene superato, come si può notare per il biochar N_2 che raggiunge il valore di saturazione ad un dosaggio pari a circa 1 g/L. Nell'intervallo studiato, invece, l'hydrochar è ancora lontano dal raggiungimento dell'equilibrio, il biochar vi si avvicina a 1 g/L, mentre il carbone attivo necessita di un intervallo di valori più basso per mostrare la sua tendenza all'equilibrio, dato che a 0,25 g/L è già all'equilibrio. Questo grafico può essere utilizzato per determinare il dosaggio ottimale, cioè il punto in cui un ulteriore aumento della concentrazione iniziale di adsorbente non comporta più un miglioramento significativo dell'efficienza di rimozione, indicando il raggiungimento dell'equilibrio.

Per valutare l'effetto del pH, sono stati condotti esperimenti con soluzioni di MB mantenute rispettivamente a pH = 7, 10 e 11,5 per tutta la durata della prova. In questo caso, il dosaggio di materiale adsorbente è stato fissato a 0,5 g/L in ogni prova. All'aumentare del pH, si ottengono efficienze di rimozione più elevate tanto più il pH supera quello corrispondente al PZC del materiale. Oltre questo valore, infatti, le interazioni elettrostatiche tra materiale adsorbente negativamente caricato e colorante cationico diventano predominanti e si ottiene un adsorbimento migliore. A livelli di pH più bassi, invece, la carica superficiale diventa positiva, quindi, a causa di forti forze repulsive tra il colorante e l'adsorbente, la percentuale di rimozione decresce.
Lo stesso andamento si osserva per la capacità di adsorbimento q_e, definita come la quantità di colorante adsorbito (mg) rispetto alla massa di adsorbente (g) impiegato. Come mostrato in *Figura IIa*, per esempio per il biochar CO_2 a pH naturale e a pH = 10 non ci sono variazioni significative nella capacità di adsorbimento, ma quando il pH supera il valore di pH_{PZC} di 9,07, si verifica un rapido aumento. In realtà, questo effetto dovrebbe essere visibile già a pH = 10, considerando il valore di pH_{PZC} di questo materiale. Tuttavia, questa discrepanza potrebbe essere dovuta ad imprecisioni nel calcolo del pH_{PZC} che

potrebbe essere più alto di 9,07, o ad imprecisioni nella misurazione del pH durante gli esperimenti a livelli di pH alterati, in cui si è arrivati a sovrastimare erroneamente il pH della soluzione, che invece era probabilmente inferiore al pH_{PZC} del materiale.
Per affinità di materiale e di pH_{PZC}, si può presumere che lo stesso andamento sia seguito dal biochar N_2, nonostante l'assenza del punto intermedio a pH = 10. Anche per l'hydrochar si nota un miglioramento dopo aver superato il pH_{PZC}.

In *Figura IIb* è riportato il grafico di q_e in funzione del pH secondo(Kannan & Sundaram, 2001), in cui è possibile avere un'idea dell'andamento completo della curva per un intervallo più ampio di valori di pH. L'andamento è lievemente crescente per pH inferiori al pH_{PZC}, mentre si denota un tratto lineare con aumento di pendenza, più o meno accentuato, in corrispondenza del superamento del pH_{PZC}. Questo risulta essere in accordo con quanto osservato durante il lavoro di tesi, in cui è stato analizzato esattamente questo tratto. Per valori crescenti di pH si denota nuovamente un andamento crescente, a pendenza decisamente ridotta.

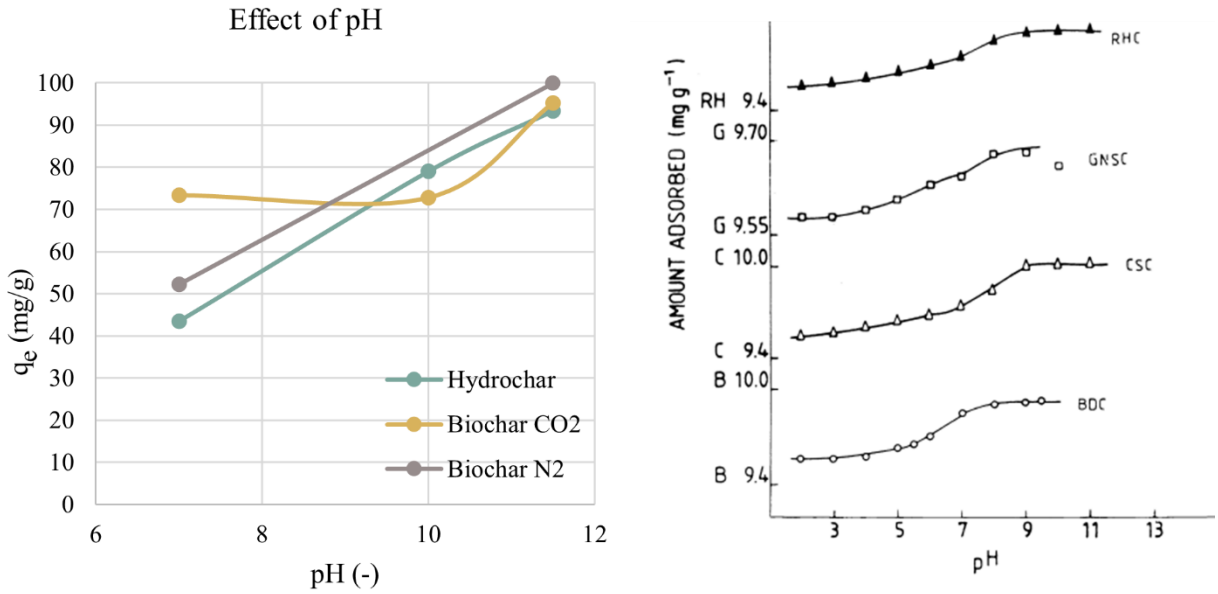

Figura II: Effetto del pH sulla capacità di adsorbimento secondo il presente studio (*Fig. IIa*) e secondo Kannan e Sundaram, 2001 (*Fig. IIb*)

L'effetto del tempo di contatto è stato valutato campionando ad intervalli regolari durante un periodo totale di 6 ore: ogni 5 minuti durante la prima ora, ogni 15 minuti nelle due ore successive ed ogni 30 minuti per il tempo rimanente. Durante la prima ora si verifica un adsorbimento più rapido a causa dell'elevato gradiente di concentrazione di MB, agente come forza spingente, tra la soluzione e i siti attivi del materiale adsorbente. Tuttavia, con il passare del tempo, il gradiente di concentrazione diminuisce poiché le molecole di MB si accumulano sui siti attivi, e la velocità di adsorbimento rallenta fino al raggiungimento dell'equilibrio, in cui le molecole di MB che desorbono sono in equilibrio dinamico con quelle che si ri-adsorbono.
Ciò suggerisce che durante la fase iniziale dell'adsorbimento è disponibile un numero sufficiente di siti attivi che vengono gradualmente occupati nel tempo, limitando un ulteriore adsorbimento.

In *Figura III* viene riportato come esempio l'andamento dell'efficienza di rimozione del biochar CO_2 in funzione del tempo, per tre diverse concentrazioni iniziali di materiale adsorbente:

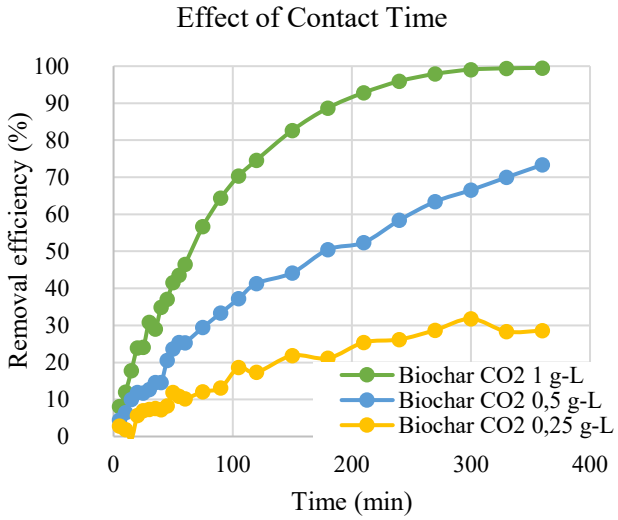

Figura III: Effetto del tempo di contatto sull'efficienza di rimozione a tre diverse concentrazioni iniziali di adsorbente

Trascorse 16 ore, è stato effettuato un ulteriore campionamento per valutare la quantità di MB adsorbita all'equilibrio, su cui basare l'analisi di tipo termodinamico.
A partire dai campionamenti è stata poi condotta un'analisi di tipo cinetico e termodinamico secondo l'utilizzo di modelli non lineari, corredata da una fase preliminare di identificazione degli outliers e da una successiva fase di validazione dei modelli identificati.

Un outlier può essere definito tale tramite un'analisi puramente grafica identificando i punti che maggiormente deviano dall'andamento generale, oppure tramite un'analisi numerica basata sui residui standardizzati, definiti come il rapporto tra i residui e la radice quadrata dell'MSE, cioè l'errore quadratico medio. I residui rappresentano lo scostamento tra i valori sperimentali di capacità adsorbente e quelli predetti dal modello, come definiti in seguito. In questo lavoro di tesi, un outlier è un valore di q_e che presenta un residuo standardizzato al di fuori dell'intervallo [-2,2], e la sua identificazione ed eliminazione è un passaggio importante, soprattutto per quanto riguarda l'influenza che esso determina sulle tecniche di validazione del modello.

Come modelli cinetici, sono stati analizzati i modelli di pseudo-primo ordine e pseudo-secondo ordine nella versione non lineare (*eq. I e II*):

$$q(t) = q_e\left(1 - e^{-k_1 t}\right) \qquad \textit{eq. (I)}$$

$$q(t) = \frac{q_e^2 k_2 t}{1 + q_e k_2 t} \qquad \textit{eq. (II)}$$

Dove q_e indica la quantità di MB adsorbita per unità di adsorbente all'equilibrio e k_1 e k_2 sono delle costanti. La scelta di utilizzare i modelli nella loro forma non lineare è in accordo con (Revellame et al., 2020), in cui vengono messi in evidenza diversi "modeling pitfalls" che vengono frequentemente

ignorati durante le analisi cinetiche e che tendono a favorire il modello di pseudo-secondo ordine durante il fitting dei dati sperimentali. La conversione dei dati cinetici per adattarli ad un modello lineare, infatti, introduce incertezze e distorsioni spesso ignorate: per esempio, la linearizzazione del modello dello pseudo-primo ordine in scala logaritmica porta a una discontinuità all'equilibrio, favorendo il modello lineare dello pseudo-secondo ordine anche per i set di dati che seguono naturalmente lo pseudo-primo ordine; questa discontinuità causa anche una disparità nel numero di punti dati utilizzabili per il fitting dei due modelli, in quanto lo pseudo-secondo ordine ha accesso a un maggior numero di punti. Inoltre, si verifica una notevole distorsione a favore del modello di pseudo-secondo ordine quando tutti i punti sperimentali sono vicini all'equilibrio. In questi casi, lo pseudo-primo ordine viene automaticamente escluso, mentre lo pseudo-secondo ordine presenta un fitting lineare quasi perfetto.

L'impiego di modelli non lineari, invece, rimuove qualsiasi eventuale necessità di conoscere parametri a priori, elimina le discontinuità e permette un confronto diretto tra primo e secondo ordine usando lo stesso numero di dati sperimentali. La modellizzazione non lineare si basa sulla minimizzazione di una funzione obiettivo, in questo caso la somma dei residui quadratici (SSR o SSE), definita come:

$$SSR = \sum_{i=1}^{n}\left(q_{t,exp} - q_{t,calc}\right)^2 \qquad \textit{eq. (III)}$$

Per ottenere il valore minimo, le equazioni dei modelli non lineari sono state applicate ai dati sperimentali inizializzando i parametri del modello secondo una prima stima fornita dall'applicazione dei modelli lineari. In seguito, tramite iterate successive, i parametri sono stati variati gradualmente e, attraverso il *Solver* di Microsoft Excel, sono stati trovati i valori corrispondenti al valore minimo della funzione obiettivo, assicurandosi che fosse un valore di minimo assoluto e non locale. Infine, per valutare la qualità del fitting ottenuto, sono stati calcolati i valori di R^2.

Prendendo come riferimento il carbone attivo, i risultati ottenuti dall'applicazione dei due diversi modelli cinetici sono mostrati graficamente in *Figura IV* per i casi a diverso dosaggio:

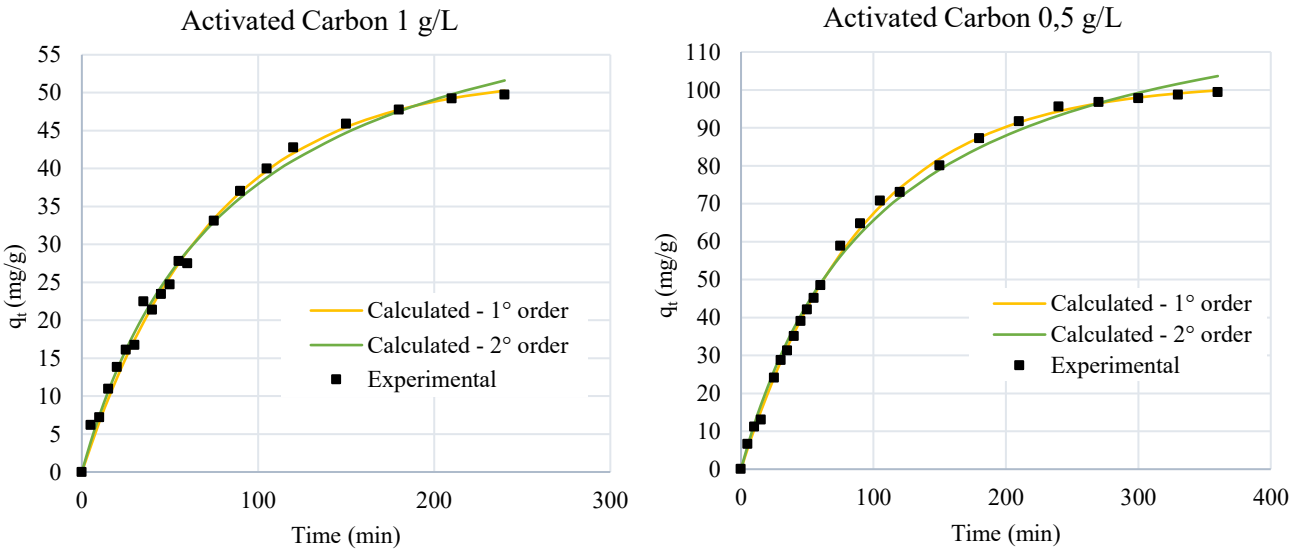

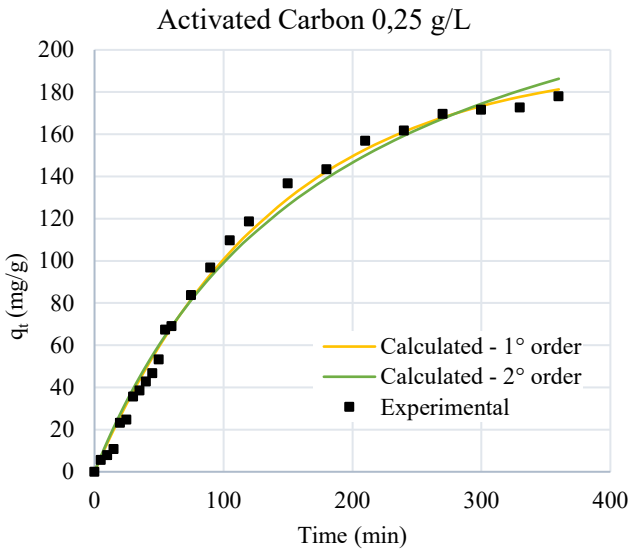

Figura IV: Applicazione dei modelli cinetici di pseudo-1° ordine e pseudo-2° ordine ai dati di adsorbimento sperimentali del carbone attivo a 1 g/L *(Fig. IVa),* a 0,5 g/L *(Fig. IVb)* e a 0,25 g/L *(Fig. IVc)*

In questo caso, il miglior modello approssimante i dati sperimentali è nettamente di tipo pseudo-primo ordine. Oltre ad avvalersi di un'analisi puramente grafica, è possibile confermare questa deduzione qualitativa in modo quantitativo osservando i valori di R^2 e confrontando il valore di q_e calcolato dal modello con quello derivato sperimentalmente. In *Tabella I* vengono riportati i valori attinenti al carbone attivo usato come esempio:

C_o (g/L)	$Q_{e,exp}$ (mg/g)	Pseudo-First Order Model			Pseudo-Second Order Model		
		k_1 (1/min)	$Q_{e,calc}$ (mg/g)	R^2 (-)	k_2 (g/mg.min)	$Q_{e,calc}$ (mg/g)	R^2 (-)
1	50,0	0,0136	**52,3**	**0,9982***	0,00017	69,5	0,9956*
0,5	99,9	0,0108	**101,9**	**0,9990**	0,00007	133,4	0,9955
0,25	198,3	0,0072	**195,9**	**0,9940**	0,00002	281,9	0,9896

Tabella I: risultati dell'analisi cinetica per il carbone attivo. * indica l'utilizzo dell'R^2 adjusted per tenere conto del diverso numero di dati sperimentali utilizzati durante l'applicazione dei modelli.

La qualità del fitting è migliore per il modello di pseudo-primo ordine, come evidenziato dai valori di R^2 molto prossimi ad 1 e dalla miglior corrispondenza tra valori di q_e calcolato e q_e sperimentale rispetto al modello del pseudo-secondo ordine.

La stessa procedura è stata seguita per gli altri materiali adsorbenti in analisi.
I risultati mostrano una cinetica dello pseudo-secondo ordine per l'hydrochar. Tuttavia, nonostante dei buoni risultati quantitativi, tramite un'analisi grafica si evince che ciò può essere ritenuto effettivamente valido solo per il caso con concentrazione iniziale di adsorbente pari a 1 g/L. Negli altri due casi, invece, i valori sperimentali sembrano avere un andamento non perfettamente approssimabile da questi tipi di modelli, evidenziato anche da un valore di R^2 più basso; sono presenti deviazioni da analizzare

ulteriormente, per cui potrebbe essere necessario utilizzare un modello diverso in grado di approssimare la cinetica in modo ancora più preciso.

Il biochar CO_2 mostra un migliore accordo tra i valori di q_e quando si utilizza un modello cinetico dello pseudo-primo ordine, ad eccezione del caso a minor concentrazione di materiale adsorbente. In questo caso, infatti, si ottiene un valore di q_e (92 mg/g) più vicino a quello sperimentale (112,8 mg/g) utilizzando un modello del pseudo-secondo ordine, ma non si tratta ancora di una buona approssimazione, in quanto mostra una differenza di oltre 20 mg/g. I valori di R^2 sono tutti molto elevati e rispecchiano quanto osservato dalla suddetta analisi q_e. Per i valori di concentrazione di biochar pari a 1 e 0,5 g/L, le curve presentano un buon andamento, mentre il caso a 0,25 g/L mostra alcune discrepanze, che potrebbero essere la causa della deviazione del valore di q_e calcolato rispetto a quello sperimentale. In generale, dunque, il biochar CO_2 segue una cinetica del pseudo-primo ordine.

Per quanto riguarda il biochar N_2, in base ai valori di q_e il modello dello pseudo-primo ordine si adatta bene ai dati sperimentali per il caso di 1 g/L, mentre nei restanti due casi è il modello del pseudo-secondo ordine a prevalere. La cinetica, quindi, sembra essere del secondo ordine a basse concentrazioni e del primo ordine a concentrazioni più elevate, richiedendo un'analisi più approfondita del fenomeno con ulteriori prove.

A seguito dell'individuazione dei migliori modelli approssimanti, particolare attenzione è stata posta alla loro validazione, testandone le ipotesi di randomicità e di distribuzione normale dei residui che sono alla base della modellizzazione. Una valutazione basata soltanto sui valori di R^2 e di q_e calcolati sarebbe errata, in quanto l'R^2 fornisce solo informazioni sulla qualità del fitting di un modello, ma non sul fatto che le variabili indipendenti considerate siano effettivamente la vera causa della variazione della variabile dipendente o sul fatto che il modello sia corretto.
Tramite un test di randomicità dei residui, invece, è possibile verificare la natura puramente casuale dell'osservazione sperimentale: se si ottiene un grafico di residui rispetto al q_e (o tempo) in cui è possibile riconoscere un andamento nei residui al variare della previsione della variabile indipendente q_e (o del tempo), significa che nel residuo ricade una parte deterministica che il modello non è stato in grado di catturare completamente ed è quindi necessario estendere e/o modificare il modello. Oltre alla randomicità, è anche importante confermare che i residui del modello seguano una distribuzione normale. Affidarsi esclusivamente alla randomicità è insufficiente: sono necessari anche i test di normalità per valutare correttamente l'adeguatezza del modello.

Tuttavia, una piccola deviazione dal comportamento ideale dei residui non significa automaticamente che il modello debba essere scartato. Quando si confrontano i modelli, si dovrebbe preferire quello che si avvicina di più al comportamento residuo previsto, cioè un andamento lineare nei normal probability plots tra i residui e la loro probabilità, e una fascia orizzontale senza alcun andamento riconoscibile nei randomness plot.

Sulla base di ciò, sono stati analizzati i diversi materiali. In *Figura V* viene riportato un esempio di comportamento ideale e uno non ideale, per entrambi i test effettuati.

A sinistra è possibile osservare un andamento non propriamente lineare del biochar N_2 con dosaggio a 0,25 g/L, soprattutto nella parte centrale del grafico, che è quella a cui si deve prestare maggiore attenzione durante l'interpretazione. A destra, invece, l'esempio dell'hydrochar a 0,5 g/L, con un andamento pressoché lineare.

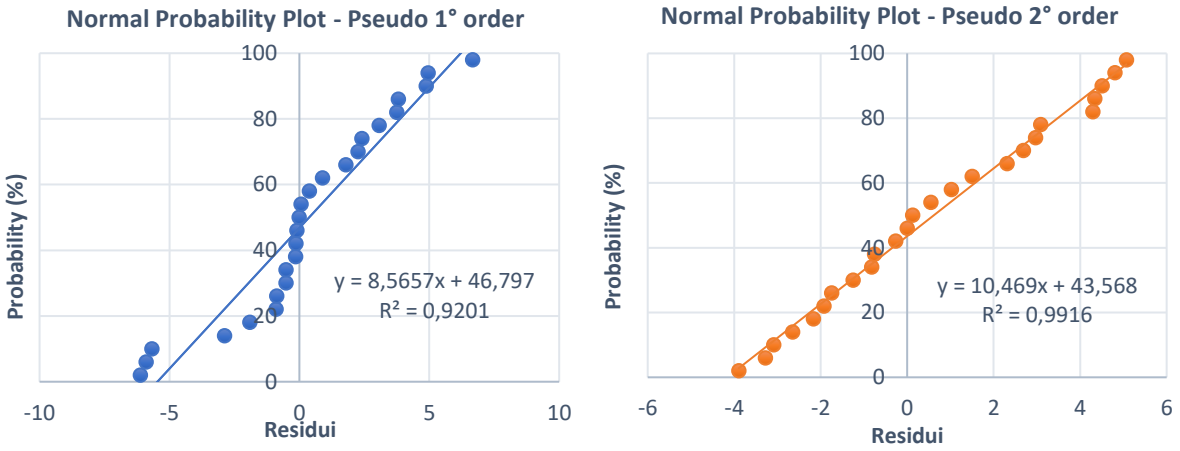

Figura V: Esempio di normal probability plot non ideale *(Fig. Va)* e approssimativamente ideale *(Fig. Vb)*

Riguardo i randomness plot, un esempio soddisfacente è quello del Biochar CO_2 a 0,25 g/L mostrato in *Figura VIa*, in cui nessuna tendenza è riconoscibile. In *Figura VIb*, invece, per l'hydrochar a 0,25 g/L è chiaramente individuabile un andamento dei residui in funzione della variabile indipendente e questo conferma quanto detto durante la precedente analisi riguardo la necessità di testare un modello di tipo diverso che possa approssimare meglio i dati sperimentali per questo materiale.

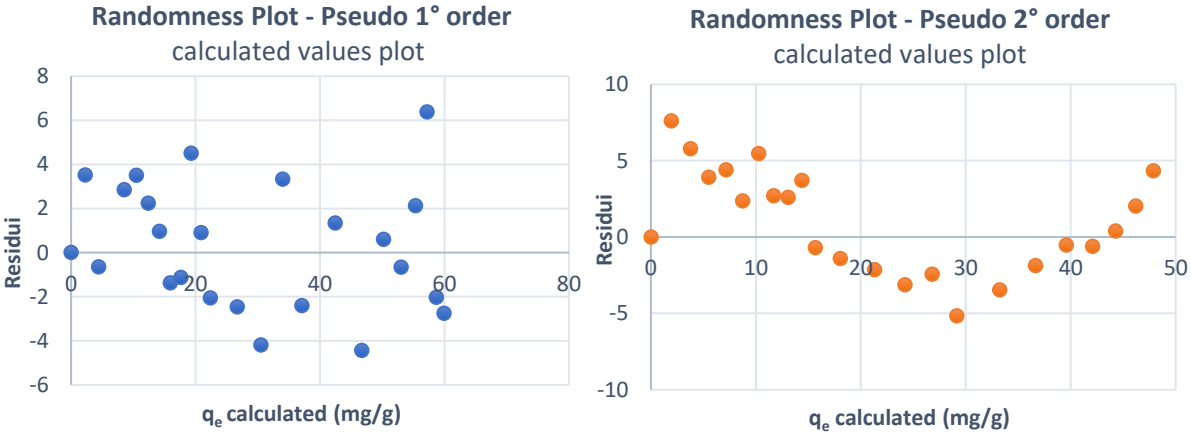

Figura VI: Esempio di randomness plot ideale *(Fig. VIa)* e non ideale *(Fig. VIb)*

A parte questo caso specifico riguardante l'hydrochar gli altri materiali presentano risultati soddisfacenti, permettendo la validazione dei modelli individuati.

L'analisi termodinamica mira a identificare l'isoterma di adsorbimento che meglio segue l'andamento dei punti sperimentali di capacità di adsorbimento all'equilibrio (q_e). È stato effettuato un confronto tra le isoterme di Langmuir e Freundlich non linearizzate (rispettivamente *eq. IV e V*) e la scelta del modello approssimante migliore si è basata nuovamente sul valore del coefficiente di determinazione R^2.

$$q_e = \frac{(q_{max} K_L C_e)}{(1+K_L C_e)} \qquad \textit{eq. (IV)}$$

$$q_e = K_F C_e^{\frac{1}{n}} \qquad \textit{eq. (V)}$$

Dove C_e indica la concentrazione all'equilibrio in soluzione (mg/L), q_{max} la capacità massima di adsorbimento e K_L è la costante energetica di Langmuir relativa al calore di adsorbimento. Il termine n indica l'affinità adsorbato-adsorbente, mentre K_F è la costante di Freundlich con unità di misura $(mg/g)(L/mg)^{1/n}$ che fornisce informazioni sull'energia di legame.

La procedura seguita per l'applicazione di questi modelli termodinamici non lineari è la stessa impiegata per i modelli cinetici e in *Figura VII* viene mostrato il grafico relativo al biochar CO_2, preso come esempio:

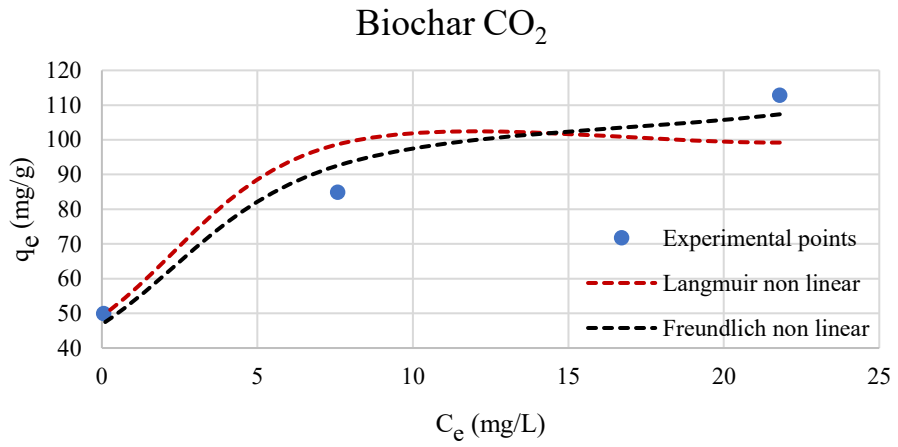

Figura VII: Applicazione dei modelli termodinamici di Langmuir e Freundlich ai dati sperimentali relativi al biochar CO_2

L'isoterma di Freundlich segue meglio l'andamento dei punti sperimentali in confronto all'isoterma di Langmuir e ciò è evidenziato anche dai valori di R^2 mostrati in *Tabella II,* che racchiudono le informazioni riguardanti l'analisi termodinamica degli altri materiali.
Anche l'hydrochar segue l'isoterma di Freundlich come il biochar CO_2, mentre il biochar N_2 e il carbone attivo sono meglio approssimati dall'isoterma di Langmuir.

Material	Langmuir Isotherm			Freundlich Isotherm		
	k_L (L/mg)	Qmax (mg/g)	R^2 (-)	k_F $(mg/g)(L/mg)^{1/n}$	n(-)	R^2 (-)
Hydrochar	0,1446	91,5	0,8790	22,4625	2,78	**0,9502**
Biochar CO_2	15,9558	99,5	0,7677	69,6645	7,13	**0,9508**
Biochar N_2	0,0926	167,6	**0,9016**	25,0994	2,06	0,8488
Activated Carbon	9,5290	247,6	**0,9762**	288,6651	2,28	0,9495

Tabella II: risultati dell'analisi termodinamica: confronto tra i diversi materiali

Infine, i dati termodinamici ricavati sono stati impiegati nella progettazione di un adsorbitore monostadio operante in discontinuo. Per il design di un adsorbitore batch, i bilanci di materia tra le correnti in ingresso e in uscita e l'introduzione delle equazioni dei modelli termodinamici all'interno dei bilanci stessi, corredate dei valori appena stimati, portano alla definizione della quantità di adsorbente necessaria per un certo volume di effluente da trattare, parametrizzato in base all'efficienza di rimozione da raggiungere a partire da una concentrazione iniziale di 50 mg/L di MB.

Il grafico mostrato in *Figura VIII* include un confronto tra tutti i materiali analizzati. Il materiale che permette la rimozione di MB usando una massa minore è sicuramente il carbone attivo.

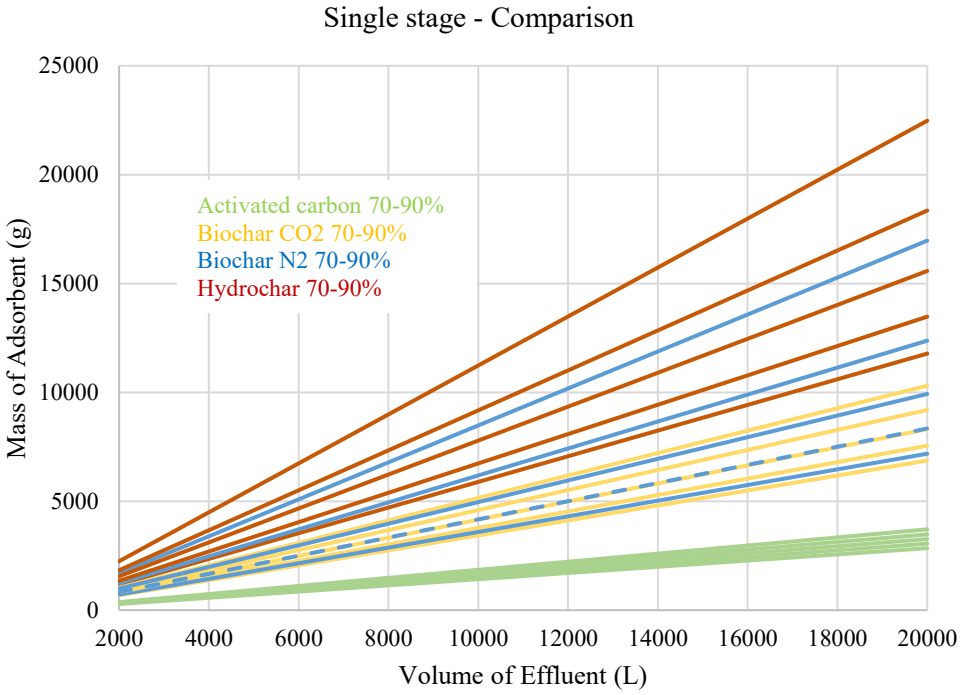

Figura VIII: Confronto tra materiali adsorbenti riguardo la massa di adsorbente necessaria in base al volume di effluente da trattare. Le curve sono parametrizzate in ordine crescente in funzione all'efficienza di rimozione (70-75-80-85-90%)

D'altra parte, con una pendenza leggermente più ripida è presente il biochar CO_2, che, quasi come il carbone attivo, non mostra particolari differenze di pendenza tra il caso di rimozione del 70% (linea inferiore) e quello del 90% (linea superiore). In particolare, si è notato che il caso a rimozione dell'80% è approssimativamente sovrapponibile al caso a rimozione del 75% per il biochar N_2 (linea tratteggiata). Pertanto, a parità di volume da trattare, è possibile utilizzare la stessa quantità di biochar CO_2 e di biochar N_2, ottenendo rispettivamente l'80% e il 75% di rimozione degli inquinanti.

Le linee rette del biochar N_2 mostrano pendenze molto variabili che vanno dalla minima alla massima rimozione, esattamente come nel caso dell'hydrochar, che peraltro è il meno efficiente, poiché necessita di una massa di oltre 20 kg per un volume di 20 000 L per un'efficienza di rimozione del 90%.

A conclusione di quanto emerso durante lo studio di tesi, vengono infine riportati i grafici di confronto tra materiali diversi a parità di concentrazione iniziale di materiale adsorbente (*Figura IX*):

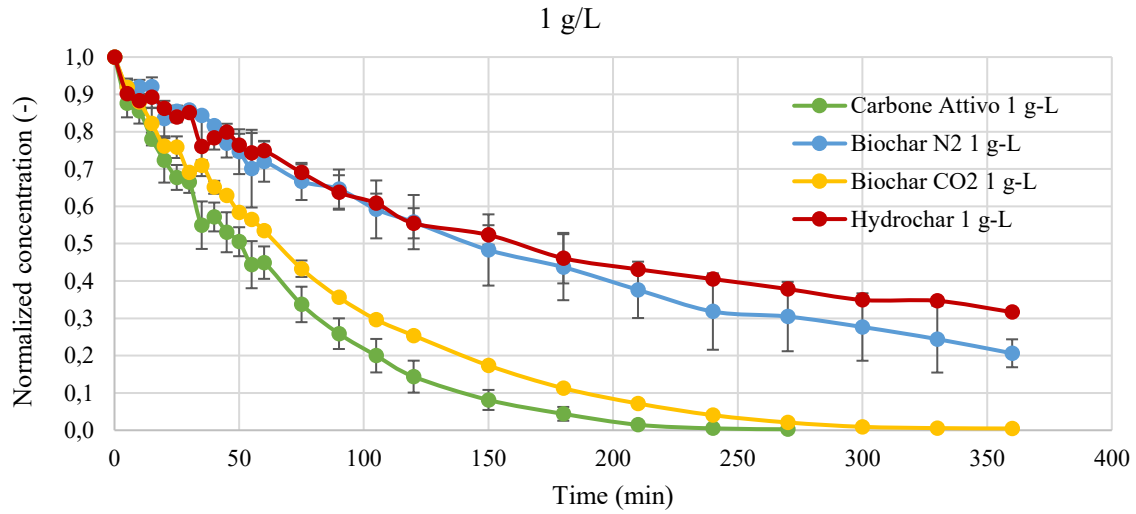

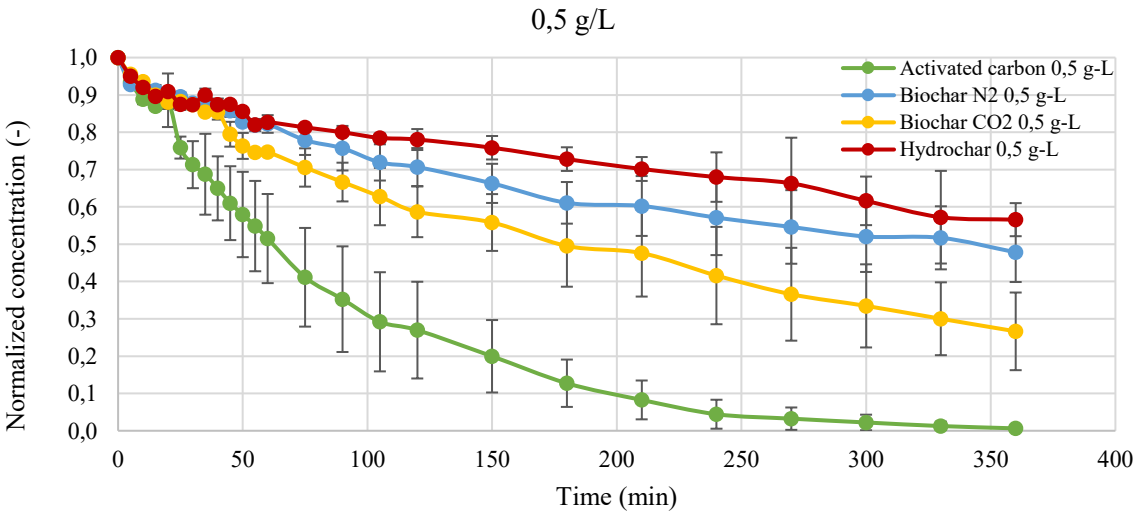

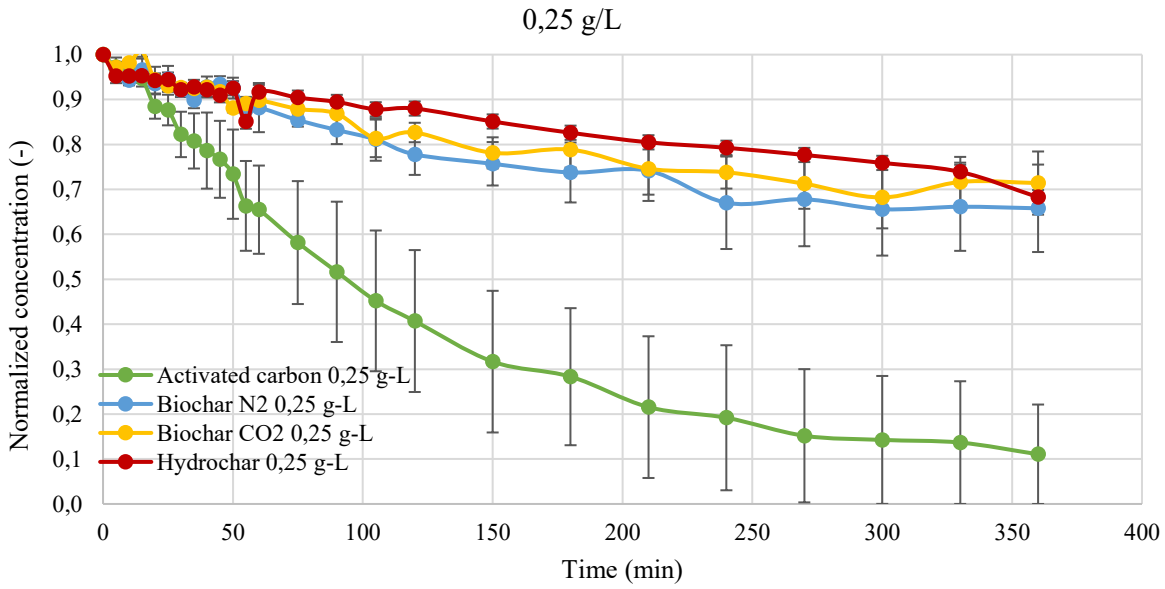

Figura IX: Grafici di confronto tra materiali diversi a parità di concentrazione iniziale di materiale adsorbente. *Figura IXa* riporta i dati a C_0 = 1 g/L, *Figura IXb* i dati a C_0 = 0,5 g/L e *Figura IXc* i dati a C_0 = 0,25 g/L

Le concentrazioni mostrate sull'asse delle ordinate sono state normalizzate a 1 per eliminare l'influenza di piccole variazioni della concentrazione iniziale di MB durante la preparazione della soluzione iniziale. I dati di concentrazione normalizzati sono stati mediati tra i duplicati o triplicati disponibili.

In tutti e tre i casi a diverse concentrazioni, il materiale con le migliori prestazioni è il carbone attivo commerciale. Gli altri materiali innovativi mostrano prestazioni inferiori, sebbene un buon risultato sia ottenuto dal biochar CO_2 ad una concentrazione iniziale di 1 g/L. In questo caso, la curva del biochar CO_2 è molto vicina a quella del carbone attivo per tutto l'esperimento. Le prestazioni peggiori sono quelle dell'hydrochar; andamenti molto simili sono seguiti dal biochar N_2 che, a differenza del biochar CO_2, a C_0 = 1 g/L non mostra alcun miglioramento delle prestazioni e continua a essere molto simile all'hydrochar.

Nel caso di concentrazioni più basse, le prestazioni dell'hydrochar, del biochar CO_2 e del biochar N_2 sono quasi sovrapponibili, con un'inversione tra il biochar CO_2 e il biochar N_2 rispetto agli altri casi, in quanto il biochar N_2 ha ora prestazioni leggermente migliori rispetto al biochar CO_2; questo, tuttavia, non è affatto osservato nei casi a C_0 = 0,5 g/L e C_0 = 1 g/L, dove il biochar CO_2 è il materiale che si avvicina di più al carbone attivo disponibile in commercio e che quindi può rappresentare il materiale alternativo adatto alla rimozione del Blu di Metilene proposto come obiettivo di questo lavoro di tesi.

Un'ulteriore analisi può essere condotta tenendo conto dell'effetto del pH, confrontando dunque le curve riferite agli esperimenti condotti a dosaggio di adsorbente pari a 0,5 g/L con quelle condotte alla stessa concentrazione, ma con un pH di 11,5 indicate con linee tratteggiate (*Figura X*).

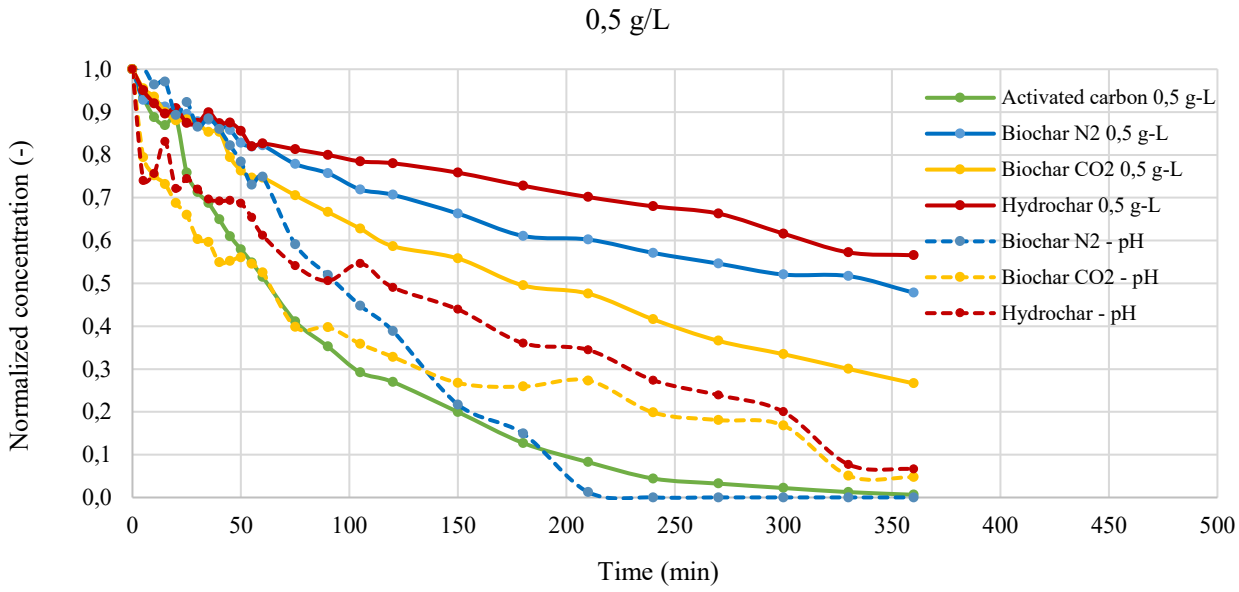

Figura X: Confronto tra prove sperimentali a pH naturale e a pH = 11,5 a parità di dosaggio di adsorbente

Ne consegue che i casi con soluzione a pH modificato mostrano generalmente prestazioni migliori, per via delle maggiori interazioni elettrostatiche. In particolare, durante i primi 60 minuti dell'esperimento, il biochar CO_2 mostra una rimozione di MB più pronunciata rispetto al materiale standard preso come riferimento, cioè il carbone attivo, ottenendo una curva più bassa. Con l'aumentare del tempo, questo vantaggio si annulla e il biochar CO_2 raggiunge una concentrazione finale leggermente inferiore rispetto a quella ottenuta dall'hydrochar.

Un andamento particolare si riscontra nel biochar N_2 con soluzione a pH = 11,5: durante la prima ora, la pendenza della curva è moderata, mostrando poi un incremento che porta questo materiale a superare significativamente tutti gli altri analizzati; il biochar N_2 in queste condizioni di pH modificato riesce a raggiungere la completa rimozione dell'inquinante intorno ai 200 minuti dall'inizio dell'esperimento, mostrando un tasso di rimozione superiore anche al carbone attivo, che tende all'asintoto della completa rimozione solo intorno alle 6 ore di esperimento.
Variando il pH, dunque, il biochar N_2 rivela prestazioni paragonabili allo standard commerciale del carbone attivo, proponendosi come valida alternativa.

In futuro, si rendono necessari studi più approfonditi per valutare la biomassa più adatta a questo tipo di applicazione e le relative condizioni di pirolisi e/o carbonizzazione idrotermale. A questo è correlato anche un ampliamento dello studio di adsorbimento che prenda in considerazione l'effetto delle altre condizioni operative non analizzate nel corso di questa tesi, l'eventuale applicazione su coloranti di natura diversa, per esempio di origine anionica, e un'analisi di tipo economico approfondita per quantificare i benefici introdotti dall'uso di questi materiali emergenti rispetto all'impiego del carbone attivo commerciale. Inoltre, risulta interessante e stimolante l'applicazione di questo metodo di rimozione del MB in continuo e lo studio su un'eventuale possibilità di rigenerazione del materiale adsorbente.

Table of Contents

Figures index

Tables index

1. Introduction

The production of synthetic dyes is currently growing due to their extensive use in various industries, such as the textile and clothing, paper, cosmetics and pharmaceuticals ones. Globally, the production of synthetic dyes is estimated to be about **$7 \cdot 10^5$ tons per year**, including mainly Aniline Blue, Alcian Blue, Basic Fuchsin, Methylene Blue, Crystal Violet, Toluidine Blue, and Congo Red. Compared to the use of dyes of natural origin, the use of synthetic dyes allows for a greater number of colour shades and, above all, is less expensive. This extensive use leads to the generation of large volumes of wastewater: the textile industry in China, the UK and the USA alone produces around **1-10 million litres** of dye-polluted water every day, which must be treated until it reaches the legal limits to be discharged into the receiving water body (Hamad & Idrus, 2022).

However, such waters cannot be managed using biological treatments that are conventionally applied to wastewater, as synthetic dyes are difficult to biodegrade due to their complex structure and often aromatic nature. In fact, they persist in the environment if not properly treated, also due to their high stability to various factors, such as the effect of light, temperature, water and other substances, e.g. detergents and soaps, and very frequently have negative environmental and toxicological effects.

Among the most widely employed dyes there is Methylene Blue (MB), mainly used as a dye for paper and leather in the **paper industry** and as a dye for wool, silk and cotton in the **textile industry**. Approximately 67% of the dye market is related to the textile industry, which generates approximately 120 cubic metres of contaminated wastewater per ton of manufactured fibre. Other industries that use it during their production activities, although in smaller quantities, include the cosmetics, pharmaceutical and food industries, where it is used as an indirect food additive.

At high concentrations, this dye represents a risk to human health and ecosystem, as it is toxic, carcinogenic and has a recalcitrant nature. The release of wastewater containing MB above threshold levels can have toxic health effects such as respiratory disorders, dermatological effects and gastrointestinal complications. Methylene blue can also inhibit plant growth, prevent the passage of light, reduce the protein content of some microalgae, and alter the normal ecosystem balance of the receiving water body, adversely affecting photosynthetic processes, COD, BOD and dissolved oxygen levels.

Another point to consider concerns the management of clean water, especially in developing countries where the shortage of clean water has been associated with the widespread textile industry, which generates large volumes of wastewater on a daily basis that are not properly treated before being released into the environment. Finally, the characteristic blue colour of MB has a strong visual impact as it is perceptible even at low concentrations, therefore making the water bodies in which it is present aesthetically unappealing.

So, due to the increasing attention on the use of water resources, to the difficulty in degrading this pollutant and to its negative effects on health and the environment, it became necessary to search for an efficient method of removing MB from industrial wastewater. It is important that this treatment is implementable on a large scale, cost-effective, effective even at low pollutant concentrations and, finally, able to avoid the production of secondary pollutants due to oxidation and degradation reactions.

1.1 State of the art

MB has a strong affinity for water under normal conditions and, since it is hardly biodegradable, it is difficult to remove using conventional treatments to which industrial wastewater is normally subjected.

Among the main methods specifically designed for dye removal, currently in use, there are:

- **Biological** methods: aerobic or anaerobic, they make use of specific microorganisms such as algae, yeasts, fungi, and bacteria that can decompose dyes. It is a cost-effective and environmentally friendly technology, but it requires large areas for installation and is highly sensitive to reaction conditions, inflexible and time consuming; moreover, synthetic dyes have a complex chemical structure that is not easily biodegradable. (Hamad & Idrus, 2022)

- **Chemical** methods: they are divided into non-photochemical and photochemical methods; the former mainly include ozonation and Fenton systems, while the latter include advanced oxidation processes assisted electrochemically, by UV light or by catalysts. Ozonation uses the highly reactive O_3 ozone for degradation, which, however, is not stable and has low solubility in water, with reaction intermediates and by-products that are hazardous. In Fenton systems, highly reactive hydroxyl radicals and Fe^{3+} are generated from H_2O_2 and Fe^{2+}. The same radicals are also formed during advanced photochemical processes using UV light, for photocatalytic effects or through electrolytic processes and attack the MB, generating non-toxic products. Chemical-physical methods include coagulation-flocculation, which, by adding chemicals to the influent, generate flocs separated by gravity. It is an efficient process, but has high costs associated with the use of these chemicals and the generation of large volumes of polluted sludge for disposal. (Hamad & Idrus, 2022)

- **Physical** methods: they include filtration processes (membranes, nano/micro/ultrafiltration), ion exchange membranes, reverse osmosis, electrolysis and, finally, adsorption. Technologies using membranes have good removal efficiencies, but the major drawback is the phenomenon of fouling, which leads to very frequent maintenance and, consequently, to large costs associated with membrane cleaning and replacement. By comparison, the most widely used technology is adsorption. (Hamad & Idrus, 2022)

Adsorption can be divided into two types: chemical and physical. In chemical adsorption, strong bonds are formed between molecules or ions of adsorbate and adsorbent and the bond is typically the result of an exchange of electrons, so it is irreversible. Physical adsorption, on the other hand, tends to be reversible, as it is based on weak intraparticle Van der Waals bonds, and is the most common type. The main physical forces involved include van der Waals forces, hydrogen bonds, polarity, dipole-dipole, ∏-∏ interaction, etc.(Yagub et al., 2014).

It is a simple operation and has a comparably cheap application. It can be applied on a large scale, as it can treat relatively high flow rates with good removal efficiency and also does not lead to the development of hazardous secondary chemicals. The flexibility of this method allows it to be applied to different types of contaminants from different sources.
This method involves the use of an adsorbent material to remove MB from wastewater.

The scheme in *Figure 1* shows the main removal methods, with a focus on adsorption and some of the employed materials:

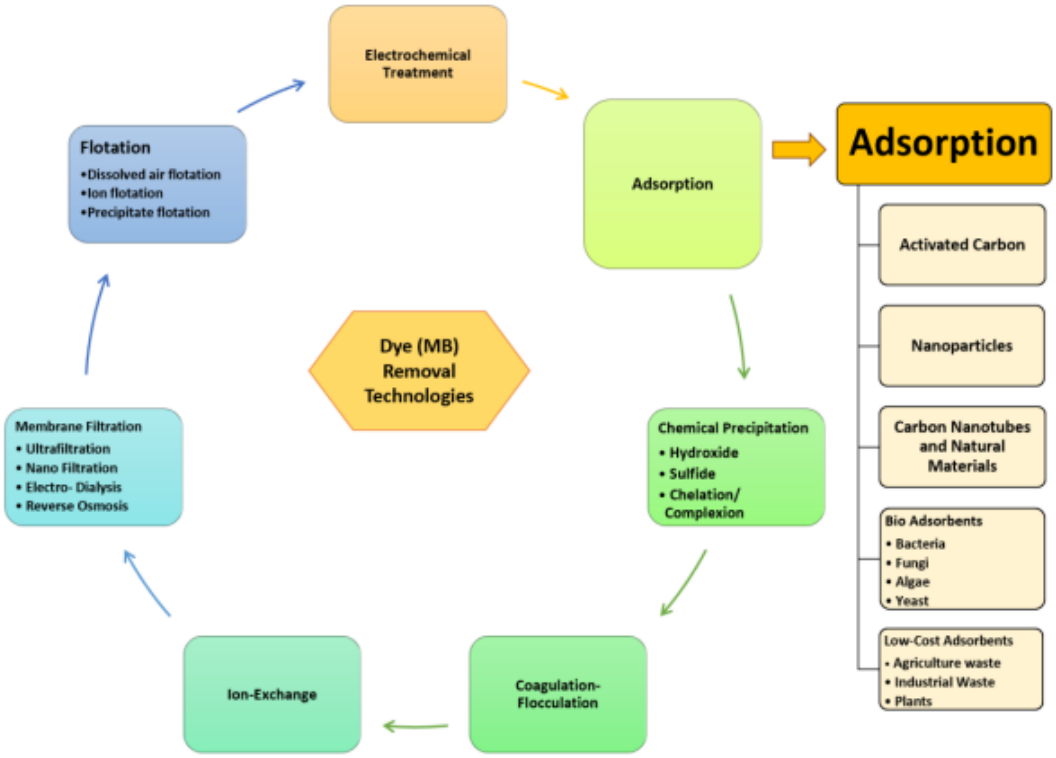

Figure 1: Schematic diagram of MB removal technologies *(Hamad & Idrus, 2022)*

There are several types of adsorbents applied for adsorption, but the most widespread and currently used is commercial activated carbon (CAC). It comes in two forms, granular and powdered, but is associated with high production and regeneration and disposal costs.
It is the commercial standard and is derived from carbonaceous materials such as wood, coconut husk, bamboo, lignite or coal. It is produced through a carbonization step followed by an activation step, either physical or chemical, to increase the specific surface area and porosity, or to form functional groups in order to have a greater external active area. During physical activation, the material is treated with hot gases, which is why it is also called gas activation. The gases used are steam, CO_2 or ozone at a temperature above 700 °C. In a first step, selective decomposition takes place towards the unstructured parts of the carbonised material and an opening of the pores of the carbon structure. In a second step, there is an enlargement of the pores (Cha et al., 2016).

In chemical activation, on the other hand, the pores are opened using chemicals, i.e. by immersing the starting material in a chemical solution of an acid, base or salt, e.g. H_3PO_4, KOH, NaOH, $ZnCl_2$, $CaCl_2$. The carbon is doped with one of these chemical agents (activating agents) and micropores are then formed by dehydration and oxidation. Compared to physical activation, it has higher efficiencies, but involves problems with corrosion of the equipment due to the substances used, which are also very expensive and difficult to recover. Both activations can be performed in series (Cha et al., 2016).

The removal method of adsorption, therefore, is cheap and industrially suitable, but the conventionally used material presents an economic problem due to its cost of production.
With regard to adsorption, therefore, research has focused on finding alternative materials to activated carbon that are competitive in terms of performance, but at a lower cost. An adsorbent material can be defined as low-cost if it requires minimal processing and its precursor has high availability, either in nature or as a by-product of other processes (Hamad & Idrus, 2022).
Another important factor concerns the sustainability of the selected adsorbent materials.

Among the main materials studied for adsorption there are, according to (Hamad & Idrus, 2022):

- Activated carbon
- Bioadsorbents (algal, bacteria, fungal, other biomass)
- Natural materials (clay minerals, zeolite)
- Carbon nanomaterials (graphene, carbon nanotube and derivatives)
- Agricultural waste derived adsorbents

Among these, the only materials that can be considered low-cost adsorbents are agricultural waste derived adsorbents, bioadsorbents and natural materials; in particular, starting from agricultural waste material provides a double benefit, i.e. purification of the water itself and waste management (Yagub et al., 2014).

In this case, the starting substance is lignocellulosic in nature and is pre-treated according to the type of waste, such as fruit peels, seeds, leaves, straw, sawdust. Then, the biomass undergoes a process, which can be for example pyrolysis, hydrothermal carbonization, torrefaction, gasification, and among the products biochar is obtained, i.e. the adsorbent material derived from the initial biomass.
Eventually, the biochar so obtained can be subjected to physical or chemical activation treatments, such as those for the production of activated carbon, increasing its adsorbing capacity but also its production costs. Finally, the biochar resulting is used for various applications: in water treatment, it is used not only for the removal of dyes such as MB, but also for the removal of heavy metals (Gupta et al., 2022).

In this thesis work, the removal of MB through the use of materials derived from agricultural waste, in particular rice husk, was investigated. Compared to activated carbon, using biochar means lower production costs and fewer steps, resulting in a highly efficient, cost-effective and environmentally safe product. Using biomass also means using a renewable starting material, and the fact that it is waste biomass promotes circularity.

In *Figure 2* is shown the scheme for obtaining biochar from waste biomass:

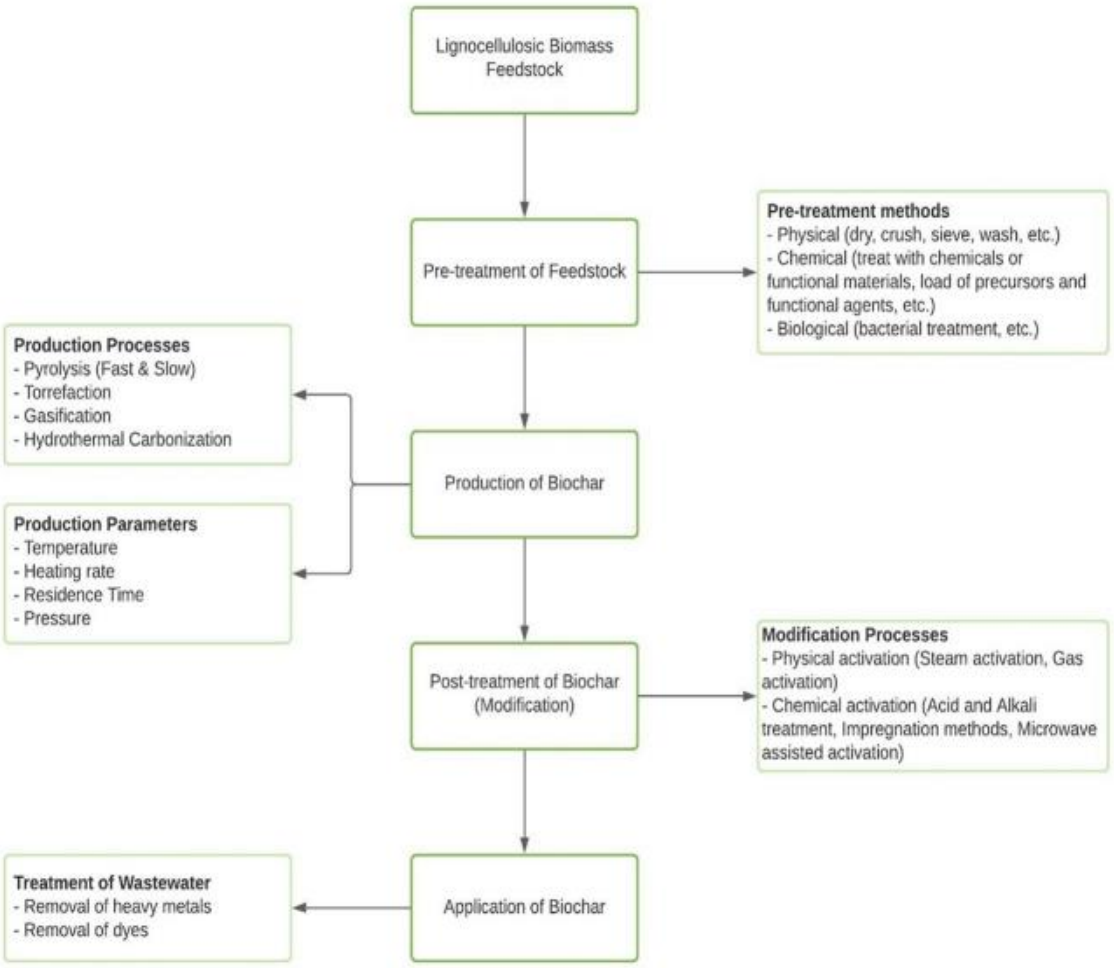

Figure 2: Scheme of biochar production starting from lignocellulosic biomass (Gupta et al., 2022)

2. Pyrolysis

As previously said, for the production of biochar, there are mainly four different processes (Gupta et al., 2022):

- Pyrolysis (pyrochar)
- Gasification
- Torrefaction
- Hydrothermal carbonization (hydrochar)

They share the operating principle, but differ in the amount of oxygen used, heating rate and final temperature, from which derives the different quantity and quality of biochar produced.

Pyrolysis is the most well-known and most frequently used thermal process for the conversion of organic waste material into biochar and is defined as the thermochemical decomposition of biomass at relatively high temperature in absence of oxygen (Kambo & Dutta, 2015).

During the pyrolysis process, the properly prepared biomass is heated in an oxygen-free environment until the temperature required for the pyrolysis reactions to take place is reached. Specifically, the biomass is subjected to a first decomposition reaction leading to the formation of a thermally stable solid product and liquids, followed by a secondary decomposition (cracking and repolymerisation) in which unstable volatile compounds are converted into gaseous products (Pandey et al., 2020). The secondary decomposition process releases the volatile species, while the non-volatile carbonaceous solid phase is collected as biochar. Afterwards, part of the gaseous phase is condensed, resulting in a viscous dark-coloured liquid that is homogeneous, hydrophilic and consists of a complex mixture of compounds resulting from the depolymerization of cellulose, hemicellulose and lignin, according to the starting biomass (Kambo & Dutta, 2015), (Rangabhashiyam & Balasubramanian, 2019).

The entire sequence of reactions to which the biomass undergoes occurs at different temperatures and at different stages throughout the process, in successive stages or overlapping, as different components are pyrolyzed at different temperatures. The main reactions are (Gupta et al., 2022):

- Drying (25 - 150 °C): is the preliminary step in the pyrolysis process that takes place during the heating of the biomass and is necessary for the removal of the moisture present in the biomass itself through evaporation;
- Dehydration: the removal of non-free water, i.e. chemically bound to the compounds, takes place;
- Depolymerization: there is a break down of the biomass components, which converts the polymers into the corresponding monomers; it occurs at a higher temperature than dehydration, as the following reactions, as it requires heat for the breaking of bonds;
- Isomerization: the structure or spatial arrangement of atoms in molecules is changed, resulting in isomers;
- Aromatization: non-aromatic compounds are converted to aromatics;
- Decarboxylation: a carboxyl group is removed from molecules participating in this reaction and carbon dioxide is released;
- Charring: it represents the process of incomplete combustion of solids subjected to high heat and leads to the formation of a carbonaceous solid residue, called char.

Pyrolysis, therefore, yields more than one product, as there is a gaseous phase (syngas) that is released during the reactions, also known as **pyrolysis gas**, consisting mainly of hydrogen, carbon monoxide, carbon dioxide and light hydrocarbons and used to provide heat for the process due to its high calorific value, then a liquid hydrocarbon phase, containing paraffins, isoparaffins, olefins, aromatic hydrocarbons and other substances depending on the starting biomass, and which can be considered as a **bio-oil**, and, finally, a carbonaceous solid part, the **biochar** (*Pirolisi e Pirogassificazione Delle Biomasse*, 2023).

Generally, the biochar produced represents about 30% by weight of the starting biomass and contains more than half of the carbon that was contained in it, so during pyrolysis the carbon content is increased by removing oxygen and hydrogen present in the biomass. This biochar yield depends mainly on the heating rate, as a higher value implies a higher gas release and therefore a lower solid yield.

As far as process parameters are concerned, different types of pyrolysis are determined depending on how the process is conducted, and the proportion in the production of bio-oil, syngas and biochar and its physicochemical properties (surface area, pore size, carbon content, functional groups), which are also influenced by the type of biomass input, also depends on this (Pandey et al., 2020).
The distinction between different pyrolysis categories is based on pyrolysis temperature, time and heating rate, and includes:

- **Slow pyrolysis** (350-700 °C): also referred to as "conventional carbonization," is conducted at relatively low temperatures, slow heating rates, and extended residence times, ranging from hours to days. This method is primarily aimed at biochar production. It's a thermodynamically controlled process in which reactants and products have enough time to reach thermodynamic equilibrium. During slow pyrolysis, the yield of biochar is higher when using biomass with elevated levels of lignin and ash, along with larger particle sizes. These conditions promote increased biochar yield by facilitating cracking reactions that reduce the production of liquids or bio-oils (Gupta et al., 2022).

- **Fast pyrolysis** (400-600 °C): This process aims to achieve high yields of bio-oil compared to solid or gaseous products. It's an instantaneous decomposition with very high heating rates (up to 1000 °C/min) and short residence times (less than 2 seconds) to minimize the reformation of intermediate compounds that would reduce bio-oil yields. It's a kinetically controlled process where the attainment of equilibrium is not waited for.
  After heating, a significant amount of volatile molecules and aerosols is rapidly released from the biomass particles, potentially causing them to disintegrate. These volatile components are then removed from the reaction zone either through vacuum extraction (in the case of vacuum pyrolysis) or by using high-flow rates of an inert sweep gas. This process is highly efficient for biofuel production since these volatile components are all condensed through rapid quenching (Brewer & Brown, 2012).

- **Flash pyrolysis** (> 750 °C): it has contact times of less than one second and temperatures above 700 °C, so as to maximize the gas phase achieved.

The operating conditions can be summarized in *Table 1* (Pandey et al., 2020):

S No.	Pyrolysis process	Temp.(in °C)	Heating rate (°C/min)	Aeration	Time	Target product
1.	Slow pyrolysis	350–700	2–7	O_2 free or limited	Hrs-days	Biochar
2.	Fast pyrolysis	400–600	>300	O_2 free	Sec	Bio-oil
3.	Flash pyrolysis	750–1000	>1000	O2 free	Sec	Bio-oil
4.	Gasification	800–1600	–	O_2 free or limited	Sec-min	Syngas
5.	Torrefaction	200–300	<1	O_2 free	Min-hrs	Torrefied biomass

Table 1: Different pyrolysis processes, conditions and targets (Pandey et al., 2020)

In summary, according to (Pandey et al., 2020), the effect of pyrolysis operating conditions on biochar is:

- **Effect of temperature**: biochar yield decreases as the temperature increases. Conversely, higher temperatures result in increased biochar surface area and carbon content.

- **Effect of heating rate**: higher heating rates encourage secondary pyrolysis reactions, which lower char yield. Lower heating rates, on the other hand, prevent secondary pyrolysis and promote higher char yield. A high heating rate also promotes rapid volatilization and so, the porosity, while a slower heating rate (<10 °C/min) promotes the formation of a stable matrix after decomposition, preventing the release of volatile compounds.

- **Effect of residence time**: the impact of residence time is usually related to heating rate and pyrolysis temperature. At the same pyrolysis temperature, increasing residence time leads to reduced biochar yield. In the case of slow pyrolysis, longer residence times favour higher char yield by aiding in the repolymerization of char constituents. At a consistent pyrolysis temperature, longer residence times lead to a reduction in biochar volatile matter content and an increase in fixed carbon content.

3. Hydrothermal Carbonization (HTC)

Hydrothermal carbonization, also known as “wet pyrolysis”, is a thermochemical process for the conversion of biomass into a carbon-rich solid product called hydrochar (Kambo & Dutta, 2015).

The term 'wet' denotes the fact that, unlike conventional pyrolysis, the biomass is submerged in water. It is sealed in a confined system at a pressure of approximately 2 to 6 MPa and heated to 180 to 260 °C for a time ranging from 5 to 240 minutes (Kambo & Dutta, 2015), following a process in which the water acts as a reacting medium. The pressure is increased to maintain water a liquid state when the temperature is higher than 100 °C (Cha et al., 2016).

For temperatures above 260 °C, the hydrothermal degradation process can be divided into two further categories, as shown in *Figure 3* (Kambo & Dutta, 2015):

- Hydrothermal liquefaction (HTL): in this case, the desired product is not hydrochar, but in a liquid phase, since as the hydrothermal temperature rises, the hydrochar yield obtained in the process decreases;
- Hydrothermal vaporization or gasification (HTV/HTG): this is referred to also as a supercritical water gasification and the main product is in gaseous phase.

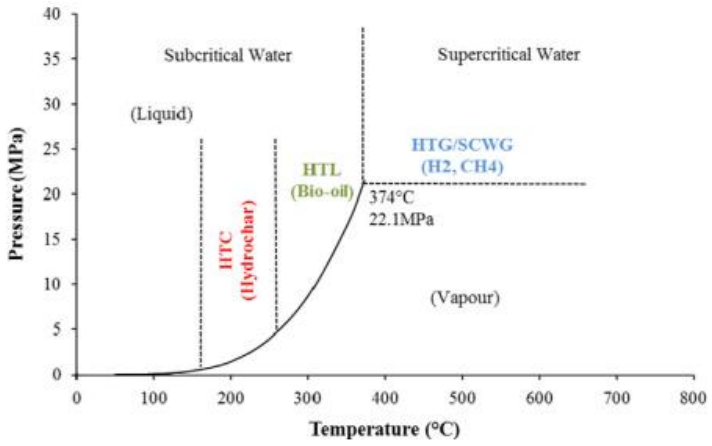

Figure 3: Classification of hydrothermal processes based on pressure-temperature phase diagram of water (Kambo & Dutta, 2015)

In fact, when the biomass undergoes hydrothermal carbonization, it produces different types of products: bio-oil (liquid product) mixed with water, carbon dioxide, other gaseous and aqueous products, and biochar, that in this case is called hydrochar and it’s the solid product of interest for the HTC process (Gupta et al., 2022).

Hydrochar is produced through a sequence of reactions made possible through the action of the subcritical water, which is liquid water below its critical point (equal to 374 °C at 22,1 MPa, according to the phase diagram) that in this case acts like a solvent to enhance the solubility of biomass compounds (Kambo & Dutta, 2015).

These reactions include biomass hydrolysis, dehydration and isomerization, following a proposed reaction network illustrated in *Figure 4*.

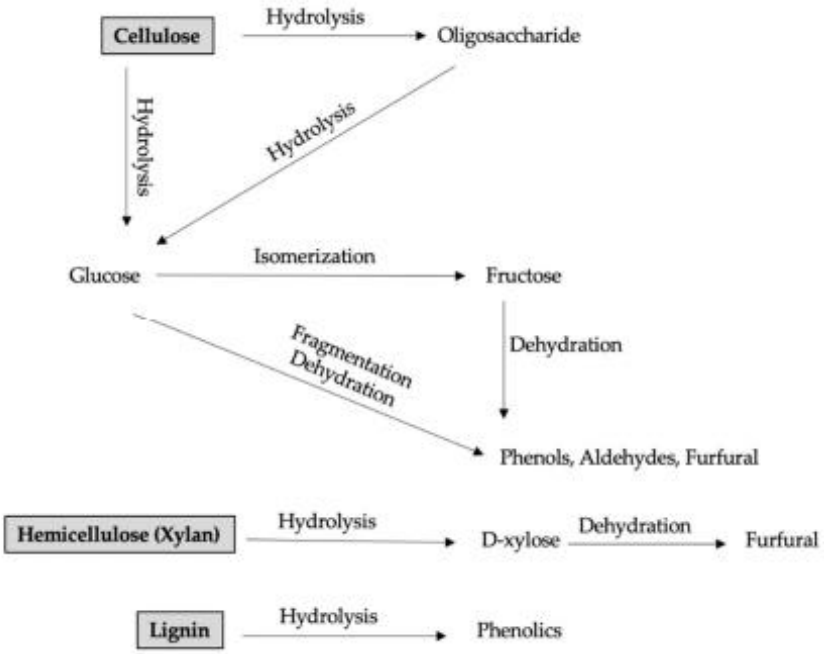

Figure 4: Reaction network of HTC (Masoumi et al., 2021)

Hydrolysis step reduces the activation energy for hemicellulose and cellulose, facilitating their degradation and depolymerization into oligomers and monomers, that are more water-soluble substances than the starting polymers (Kambo & Dutta, 2015). Then, after isomerization and dehydration steps, some intermediates like furfural are produced and the last step is the polymerization in order to obtain the hydrochar (Masoumi et al., 2021).

Since the water needs to be present throughout the entire process, the process itself is not affected by the presence of moisture in the starting biomass. Therefore, an advantage of HTC process is the fact that the drying step is not required, differently from the pyrolysis process, allowing the employment of wet biomass without the need for this energy-intensive step for the elimination of water (Kambo & Dutta, 2015).

However, the HTC process may require substantial quantities of water if employed for full-scale operation and this could result in an uneconomical process. For example, to produce one metric ton of dry hydrochar at 260°C starting from miscanthus are required approximately 12 metric tons of liquid water, assuming a 50% mass yield of hydrochar and a ratio between dry biomass to water equal to 1:6. On an industrial scale, this amount of process water required might outweigh the advantages of hydrochar concerning production costs. Therefore, the solution can be recycling process water, as this is the more practical approach to enhance the overall efficiency of the system (Kambo & Dutta, 2015).

Furthermore, another advantage is that HTC allows the production of hydrochar almost without liquid product (it can go as low as 5% wt), so that the separation from the reaction solution is easy (Kambo & Dutta, 2015).

4. Biochar and Hydrochar comparison

The chars (denominated as biochar and hydrochar) obtained through the two different processes have different physical and chemical characteristics that have an impact on possible applications, including carbon capture, soil improvement, bioenergy production and adsorption from polluted wastewater. For example, a biochar with a low carbon and high ash content is not appropriate for energy production due to its low heating value, just as a biochar with a small surface area and limited adsorption capacity is not suitable for agriculture and wastewater treatment (Kambo & Dutta, 2015).

The reaction temperature is the parameter that most influences the biochar and hydrochar yield and their physicochemical properties, as different reaction mechanisms prevail during pyrolysis and HTC depending on the temperature. Hydrothermal carbonization, which occurs at low temperatures due to the availability of hot water as a reaction medium, favours mechanisms that result in less carbon conversion than pyrolysis. This ultimately results in a higher H/C and O/C atomic ratio for hydrochar than for biochar (Masoumi et al., 2021).

The presence of subcritical water during HTC also causes the starting biomass hemicellulose to decompose faster, resulting in a lignin-rich product. Since lignin has a higher energy density than hemicellulose, the hydrochar obtained has a higher HHV (High Heating Value) than biochar.
The HHV of hydrochar is also related to the formation of reaction intermediates, such as 2,5-HMF, which have a similar heating value to lignin and precipitate in the porous structure of hydrochar (Kambo & Dutta, 2015). Due to the presence of water as a reaction medium, the inorganic compounds in the initial biomass are demineralized, causing a reduction in the ash content of hydrochar compared to biochar (Masoumi et al., 2021).

Regarding surface and structure characteristics, biochar produced by slow pyrolysis at 500-600 °C contains aromatic groups, while hydrochar produced at 200-250 °C contains more alkyl groups.
In fact, both chars, at the end of the process, show a similar fundamental molecular structure, with a generally enhanced surface area, porosity and aromatic nature with respect to the initial biomass, but the surface features substantially differ from each other.
Hydrochar has a surface with a high degree of aromatization, has higher cation exchange capacity and contains a higher number of oxygen functional groups with respect to biochar, leading to a high affinity for water and a slightly higher acidity (Kambo & Dutta, 2015).
Biochar has a more alkaline pH due to the presence of possible metals and inorganic compounds that, unlike hydrochar, have not been demineralized by water, and due to the loss of carboxyl and hydroxyl groups during pyrolysis (Masoumi et al., 2021).

Compared to biochar, hydrochar shows a lower surface area and porosity. Biochar has a specific surface area that is proportional to the reaction temperature, but can have a lower specific surface area than hydrochar in the case of excessively high temperatures and heating rates during pyrolysis, which, above a certain value, lead to the destruction of the porous structure formed and the clogging of pores (Masoumi et al., 2021).

Furthermore, on a morphological level, biochar possesses graphite-like layers and has particles with heterogeneous sizes, unlike hydrochar, which has a surface composed of spherical particles and has homogeneous size ranges (Masoumi et al., 2021).

Table 2 summarises the main differences between hydrochar and biochar according to (Masoumi et al., 2021):

Properties	Hydrochar	Biochar
Specific surface area and porosity	Non-porous, low specific surface area	Porous and depends on the reaction temperature could exhibit higher specific surface area (>400 m^2/g)
Morphology	Spherical shape	Graphite-like layers
Total carbon content	58–64 wt.%	60–80 wt.%
H/C molar ratio	>2.3	>1.5
O/C molar ratio	>1.7	>0.7
pH	Mostly acidic	Mostly alkaline
Aromaticity	Contains alkyl moieties	Contains aromatic groups

Table 2: Comparison between biochar and hydrochar (Masoumi et al., 2021)

5. Materials and Methods

In this chapter, materials and methods used during the study of the adsorption process of Methylene Blue by four different adsorbent materials are presented. The aim is to assess the potential of biochar, hydrochar and activated carbon as adsorbents for the removal of this organic pollutant. Each material possesses distinct properties that need to be characterized, as they influence the adsorption behaviour of the material itself.

Furthermore, it is essential not only to understand the characteristics of the adsorbent materials, but also those of Methylene Blue, in order to better comprehend their interaction and, consequently, the adsorption process that occurs.

Particular attention is given to investigating the effects of certain experimental parameters, such as the pH, adsorbent material concentration and contact time, with the objective of identifying the optimal conditions for the adsorption process.

The experimental setup and data collection procedure are also described, as they represent fundamental steps to obtain replicable and reliable results, from which meaningful conclusions can be drawn.

Finally, an overview is provided regarding the methods used for data analysis, particularly discussing kinetic and thermodynamic models, with a note on the potential scale-up of the process.

5.1 Materials

5.1.1 Adsorbents

As adsorbents, four different kinds of materials were used: activated carbon, hydrochar and two types of biochar.

Biochar

According to the International Biochar Initiative (IBI), biochar can be defined in a standardized way as "*a solid material obtained from the thermochemical conversion of biomass in an oxygen-limited environment"* (M. Ahmad et al., 2014).
In this study, the biochar was produced using rice husks as starting biomass and the thermochemical conversion was made through pyrolysis. Rice husk (or rice hull) is the hard outer covering of the rice grain and represents a byproduct of cereal processing, particularly from the dehulling phase.

Rice husks were purchased from S.P. S.p.a. After that, they were subsequently weighted and placed in a stainless-steel pyrolysis reactor, which is part of the pyrolysis plant together with a furnace and a condenser (to condensate heavy volatile compounds produced during the reaction).

The reactor is a fixed-bed reactor (*Figure 5*) and it's constituted by a cylindrical capsule in AISI310. This capsule consists of three different sections: a central body measuring 139 mm in length and 26,64 mm in diameter, and two threaded caps to allow the sealing. A tube allows the gas to exit the reactor and directs it to the condenser. Before proceeding with the thermochemical process, an inert gas is introduced through another tube to make sure that the atmosphere is inert. A thermocouple is attached to this tube and is in contact with the biomass to monitor the temperature during the process. A third tube contains another thermocouple to monitor the temperature at a different point, allowing better monitoring and ensuring an even distribution of heating within the reactor.
Two different types of biochar were prepared, with the only difference being the inert gas used to create the oxygen-limited conditions. In the first case, nitrogen (N_2) was used, while in the second case, carbon dioxide (CO_2) was employed.

After the inertization step, the biomass was pyrolyzed at a temperature of **600 °C** for a residence time of 1 hour under a flow of inert gas, with the temperature ramping at a rate of 15 °C/min following a material heating program regulated by a PID temperature controller.
After the pyrolysis process, the obtained biochar remained in the reactor as solid residue of the biomass. It was washed with distilled water to remove impurities and then dried at 105 °C until reaching a constant weight. Finally, the yield from rice husks to biochar was calculated through the weight loss and the result obtained was 32,1% yield by weight for biochar CO_2 and 31,1% yield by weight for biochar N_2, which are similar values to that obtained by (Singh Karam et al., 2022).

Typically, rice husk biochar (RHB) constitutes 20% of the rice weight and comprises 50% cellulose, 25–30% lignin, 15–20% silica, and 10–15% moisture (Singh Karam et al., 2022).

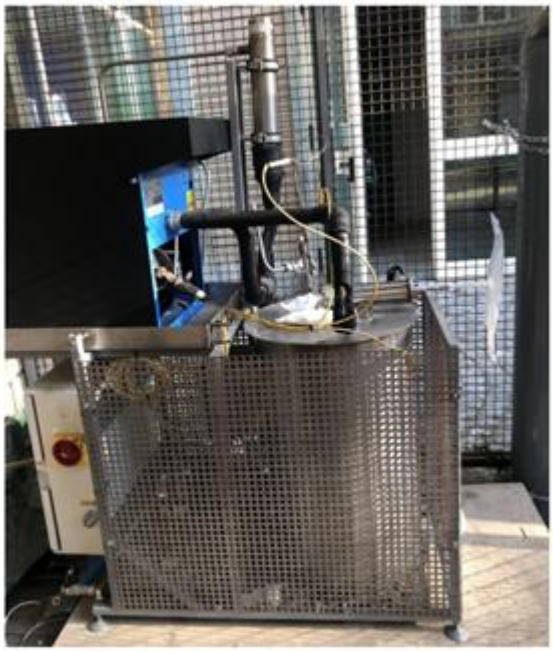

Figure 5: Pyrolysis plant

Hydrochar

Hydrochar, instead, is the product of a hydrothermal conversion process and not of a thermochemical one like biochar, as it involves the use of hot water during the reaction and occurs at lower temperatures (180-260°C). In this study, hydrochar was produced in laboratory through Hydrothermal Carbonization (HTC) starting from the same rice husks used for the production of biochar (Kambo & Dutta, 2015).

Due to the presence of water during the process, the moisture in the feedstock is no longer a problem: this is an advantage because it eliminates the pre-drying requirement of wet biomass, which, in contrast, is an essential and energy-intensive step in pyrolysis (Kambo & Dutta, 2015).

So, the biomass was directly submerged in water at a percentage of 20 wt.% of dry rice husk in water (considering the initial moisture content, distilled water was added to reach this percentage), resulting in a total of 200 g of obtained slurry made of rice husk and water (*Figure 6),* and placed in an HTC reactor.

Figure 6: Slurry (20 wt % rice husk in water*)*

Reactions were conducted in batch mode using a Parr 4575A HP/HT stirred reactor (*Figure 7*) with a nominal volume of 500 mL. The reactor vessel was constructed with Hastelloy C-276 alloy. Taking into account the headspace and various fittings, the total effective volume of the reaction environment was measured to be approximately 567 mL.

The reactor was heated up to an operating temperature of **240 °C** for a duration of 60 minutes of reaction time after reaching the set-point temperature. The initial reactor pressure was 2 barg (3 bara) of Helium at 19,3 °C and it reached a final pressure of 6,5 barg (7,5 bara) at 26,6 °C.

Figure 7: HTC reactor

At the end of the HTC process, hydrochar is in a wet state, with a slurry-like consistency. So, after cooling down the reactor, the reactor content must undergo a series of steps in order to separate all the formed phases (e.g. solid, oil, gas and aqueous phase). The separation of the aqueous phase from the solid one was performed by a filtration step, followed by a mechanically recovery of part of the solid that remained attached to the reactor's wall, that is the solid residue on the vessel. Lastly, several washes of the solid with ethyl acetate were conducted to remove the oily phase impregnated in the solid, continuing until the ethyl acetate used for washing no longer changed colour upon contact with the solid. Afterward, the solid was left at 105 °C overnight to remove traces of solvent ant then weighted to determine the final solid yield equal to 47,8 %, defined as grams of dry feed divided by grams of solid obtained. Regarding the other phases, it was found that feed to oil, to gas and to aqueous phase yields are equal to 5,3%, 17,3%, 29,7% respectively.
Hydrochar, biochar N_2 and biochar CO_2 are shown in *Figure 8*:

Figure 8: Samples of hydrochar, biochar N_2 and biochar CO_2

Activated Carbon

Activated carbon was purchased from an external supplier (NORIT) and it derives from poplar. The activation process was not specified, and it appears in a pelletized form with dimensions between 0,5 – 1,00 mm. Its yield corresponds to 32,7% by weight.

5.1.2 Adsorbate

In all the experiments of this study, the pollutant to be removed is a dye called Methylene Blue.

Many industries, such as textile, leather, paper, plastic, etc., utilize dyes to colour their products, consequently generating substantial volumes of polluted wastewater. The presence of dyes in wastewater is a significant problem to address, as it affects various forms of life. Indeed, the release of dyes into the environment creates issues from a toxicological, environmental, and aesthetic point of view. Colour influences the public perception of water quality and it's the first contaminant to be recognized in wastewater, as a simple visual analysis is enough to notice it. Furthermore, even minute quantities of dyes in water, for example less than 1 ppm for some dyes, are highly visible and undesirable (Rafatullah et al., 2010).

Methylene Blue (*Figure 9*) is one of the most used dyes for dyeing cotton, wood, and silk. Its contact with eyes can cause burns and lead to permanent injury for both humans and animals. Inhalation of MB can result in short periods of rapid or difficult breathing, while ingestion may cause burning sensations, nausea, vomiting, profuse sweating, mental confusion, and methemoglobinemia. Consequently, treating effluents containing this dye is essential to mitigate its harmful impact on receiving waters (Rafatullah et al., 2010).

It is a heterocyclic cationic dye with an aromatic nature. Its molecular formula is $C_{16}H_{18}N_3ClS$ with a molecular weight of 319,85 g/mol and its maximum adsorption wavelength (λ_{max}) is at 664 nm. MB has high water solubility (43,6 g/L at 25 °C), easily forming a stable solution with water at room temperature. According to the International Union of Pure and Applied Chemistry (IUPAC), its chemical name is *3,7-bis(dimethylamino) phenothiazine chloride tetra methylthionine chloride*, and it is classified under colour index (CI) of 52015 (Khan et al., 2022).

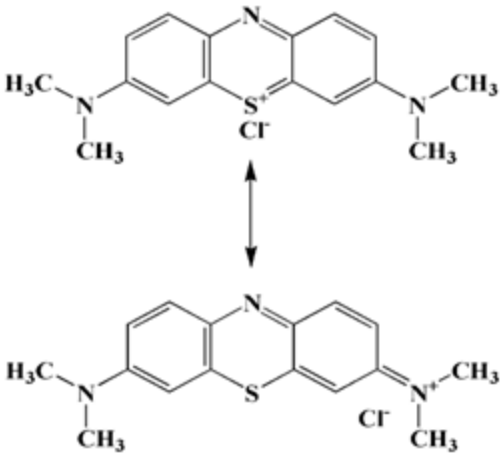

Figure 9: Different resonance structure of MB (Khan et al., 2022)

Methylene Blue is an odourless dark-green powder at room temperature that leads to a deep blue solution when dissolved in water. Its molecular diffusivity is equal to 4,7 × 106 (cm^2/s) at 25 °C, while, based on the different resonance structures, the length of the molecule can be 13,82 Å or 14,47 Å, with a width of approximately 9,5 Å (Khan et al., 2022).
The colour of MB is influenced by its chromophoric group, the N-S conjugated system on the central aromatic heterocycle, and its auxochrome group, the N-containing group with lone pair electrons on the benzene ring: MB has a characteristic deep blue colour if it's in the oxidized state, while it's colourless in the reduced form, known as leucoMB (Khan et al., 2022).

In adsorption studies, UV-analysis of this molecule is essential, because most calculations are based on its UV-Visible spectra. Regarding the adsorption spectra of MB, the most intense peak is around 664 nm, which corresponds to a MB monomer, with a lower peak at about 612 nm corresponding to a MB dimer. Additionally, two bands appear in the ultraviolet region with peaks around 292 and 245 nm, associated with substituted benzene rings. Furthermore, to identify the chemical bonds and functional groups the Fourier transform infrared-spectroscopy (FTIR) can be exploited, in order to perform a quantitative and qualitative analysis. Results of FTIR analysis from literature are shown in *Table 3* (Khan et al., 2022).

Table 3: FTIR spectra of MB (Khan et al., 2022)

FTIR Transmission Wavenumbers (cm^{-1})	Assignments
3410	-NH/-OH overlapped stretching vibration
2928	symmetrical stretching C-H of -CH_2 band
1600	C=N central ring stretching
1482	C=C side ring stretching
1384	multiple ring stretching
1590	skeleton stretching vibration of the benzene ring
1486.4 and 1389	stretching vibration of C–N in aromatic amines
1320	C_{Ar}–N stretching
1572	stretching band of C=O, C-N of amide II
1240 and 1182	N–CH_3 stretching
1143	stretching vibration of C–N in the aliphatic chain
1442	symmetrical stretching band of –COOH
1140 and 854	bending band of N-H and C-N from the amide III
880	absorption of C–H in-plane bending vibration
665	skeleton vibration mode of C–S–C

As far as this study is concerned, the Methylene Blue was purchased from Alquera (*Figure 10*).

Figure 10: Methylene Blue from Alquera

5.2 Characterization techniques

This chapter focuses on the characterization techniques used to analyse biochar, hydrochar, and activated carbon, the adsorbents employed in this study for methylene blue removal, in order to understand their physicochemical properties. Techniques and instruments, such as **FESEM, BET, CHNSO, UV-vis spectrophotometry** and **pHmeter** will be presented, as they provide information about morphology, surface area, porosity, etc., that can be useful in interpreting adsorption data, or as they are tools to perform adsorptions experiments.

5.2.1 Field Emission Scanning Electron Microscopy (FESEM)

FESEM, which stands for Field Emission Scanning Electron Microscopy (*Figure 11*), is one of the most commonly used characterization techniques for examining these properties (Pellenz et al., 2023):

- morphology: it indicates shape and size of a sample.
- topography: it describes surface features of a sample, its texture, smoothness or roughness.
- chemical composition: elements and compounds that constitute the material.
- crystallography: it concerns about the material's arrangement of atoms.

Particularly, it can be employed to visualize the shape and porous structure of adsorbent materials, as in this case. It is important to highlight that this technique does not give any internal information, it only helps to visualize surface images of a sample.

The electron microscope follows the same working principle as the optical microscope, but the difference lies in the fact that the optical microscope uses visible light as a source, while the electron microscope employs a focused accelerated electron beam. The spatial resolution of the electron microscope is not limited by diffraction as is the case with the optical microscope, because electrons have a shorter wavelength than visible light and so this results in diffraction effects occurring at much smaller physical dimensions. As a result, atomic features ranging from nanometer to micrometer particle size can be resolved (Akhtar et al., 2018).

There are two types of electron microscopes: the scanning electron microscope (SEM) and the transmission electron microscope (TEM). In essence, the first detects scattered electrons emitted from the sample's surface, while the second detects the transmitted ones (Akhtar et al., 2018).

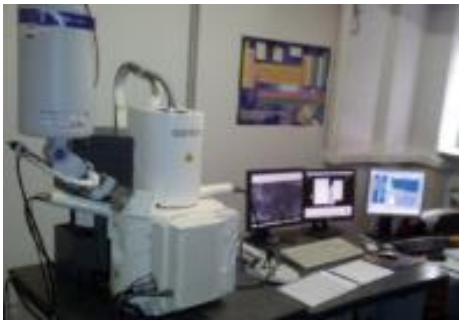

Figure 11: ZEISS Supra 40 Field Emission Scanning Electron Microscopy

In particular, the working principle of the scanning electron microscope involves exciting the sample with an electron beam. This beam is generated by an electron gun, then passes through a series of magnetic lenses inside a vacuum chamber, and reaches the sample coated with a thin layer of conductive metal to amplify the signal. Here it scans the surface, causing the emission of secondary electrons due to reflection and interaction of the electron beam with the surface itself. These electrons are referred to as *backscattered electrons* and are detected by a detector, which converts this information into a scanning image of the surface (*Figure 12*) (Pellenz et al., 2023).

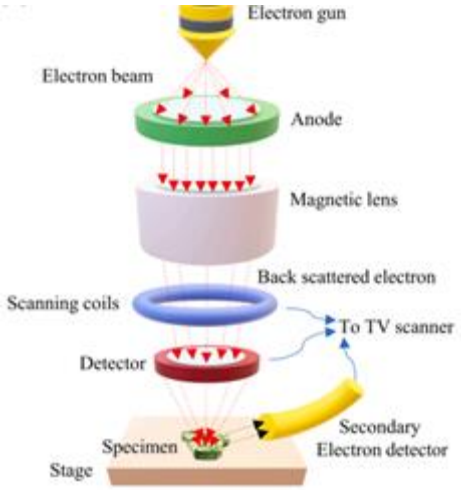

Figure 12: Scheme of a SEM (Pellenz et al., 2023)

FESEM represents an advanced version of SEM, which stands for Scanning Electron Microscopy. It differs from SEM in terms of the electron generation systems: FESEM employs a *field emission gun*, where a potential gradient is applied to emit a narrower electron beam; SEM, instead, uses a thermionic electrons emission system (Pellenz et al., 2023).

The employment of a field emission gun allows to generate cleaner images with better spatial resolution, even up to a nanometric scale (e.g. 1,5 nm, three or six times better than SEM) and with less electrostatic distortions (Akhtar et al., 2018).

5.2.2 Brunauer-Emmett-Teller analysis (BET)

In order to characterize the materials in terms of their suitability as adsorbents, it is essential to determine their specific surface area (m^2/g) and pore size distribution.

This type of analysis is of great importance, due to close correlation between specific surface area/porosity and adsorption capacity of the material. It consists of physical adsorption of inert gases (e.g. N_2, CO_2, Ar) and it's based on an extension of monolayer molecular adsorption Langmuir Theory, with three additional assumptions (Raja & Barron, 2023):

- Gas molecules will undergo physical adsorption on a solid surface in infinite layers.
- The distinct layers of adsorption do not interact with each other.
- This theoretical concept can be applied individually to each layer.

In this case, Brunauer-Emmett-Teller (BET) *Micrometrics Tristar II* system was used (*Figure 13*).

Figure 13: Micrometrics Tristar II

During this analysis, the sample must be put in a glass vial and weighted, and then it is degassed in a vacuum by a device called *Micrometrics FlowPrep 060* where it is kept at 400°C for six hours. This allows water and other gases to desorb from the surface of the sample and avoid it from happening during the BET analysis.

Then, given that the interaction between gaseous and solid phases is generally weak, the surface is cooled using liquid nitrogen as shown in *Figure 14*, so that the interaction between gas molecules and surface is strong enough to allow for measurable adsorption (Raja & Barron, 2023).

Afterwards, nitrogen gas is then incrementally introduced into the sample cell with a calibrated piston, generating relative pressures lower than atmospheric pressure through partial vacuum conditions. Pressure varies from 0 to 1 and, after reaching the saturation pressure, no more adsorption occurs even if pressure continues increasing. Highly precise and accurate pressure transducers monitor the pressure changes during the process (Raja & Barron, 2023).

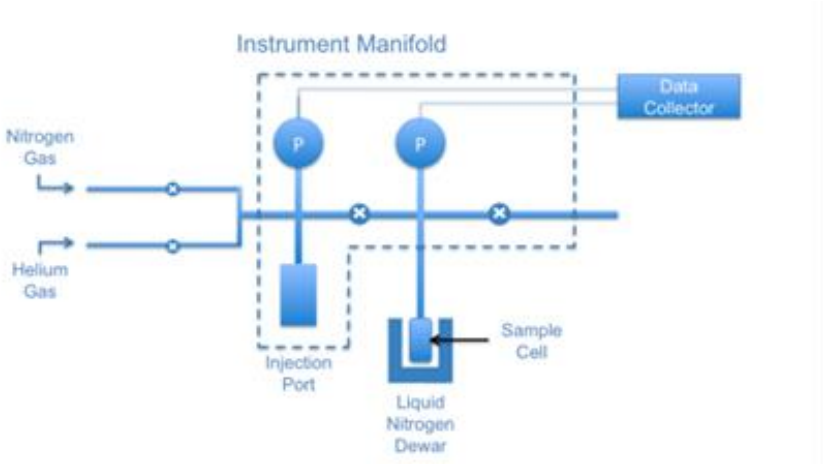

Figure 14: Scheme of BET instrument *(Raja & Barron, 2023)*

During the adsorption step, the gas molecules are adsorbed by the material and follow a certain order, as they firstly cover the micropores (< 2 nm), then mesopores (2-50 nm) and macropores (> 50 nm), until forming a monolayer of molecules over the entire area of the sample(Pellenz et al., 2023).

After the adsorption layers are formed, the sample is taken out of the nitrogen environment and heated to release the adsorbed nitrogen, which is then quantified. The collected data is presented through a BET isotherm, graphing the amount of gas adsorbed against relative pressure, as shown in *Figure 15* (Raja & Barron, 2023):

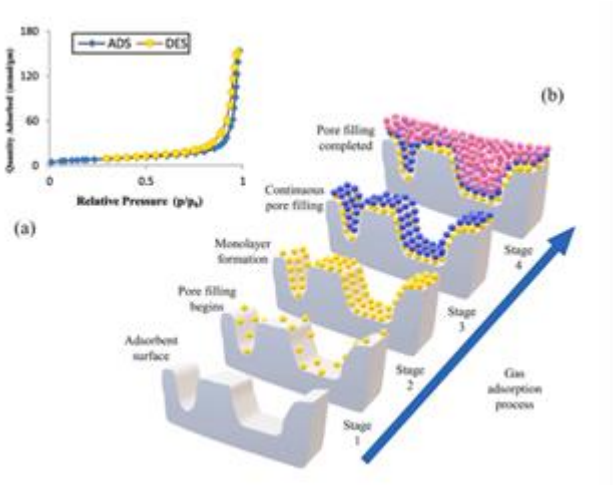

Figure 15: BET technique working principle (Pellenz et al., 2023)

From the measure of the monolayer quantity of adsorbed gas obtained from the isotherm, the surface area can be determined. From desorption data and specifically from the adsorption/desorption hysteresis, information about pore size distribution can be extracted: pore size is calculated from the quantity of gas that condenses inside the pores.

5.2.3 Elemental analysis CHNSO

Another technique for the characterization of the adsorbent material is CHNSO elemental analysis. This allows for the determination of the quantities of carbon (C), hydrogen (H), nitrogen (N), sulphur (S), and oxygen (O) present within the sample. Knowing the quantity of the organic substances present serves as a clue for determining the structure of the substance under analysis.

The CHNSO elemental analysis technique is based on the combustion of a sample inside an elemental analyser: during the combustion (furnace at around 1000°C), the carbon in the sample turns into carbon dioxide, hydrogen into water, nitrogen into nitrogen gas or nitrogen oxides, and sulphur into sulphur dioxide. The sample creates gas compounds made of C, H, N, S: these formed compounds are carried out of the combustion chamber by an inert carrier gas, usually Helium, and passed over heated high-purity copper (reduction stage) to remove any remaining oxygen not used in the reaction and to convert nitrogen oxides into nitrogen gas (Thompson Michael, 2008).

Finally, the compounds are identified using gas chromatography (GC column), and from the determined substances, the ratio of these elements (C, H, N, S) in the original sample can be deduced (oxygen is calculated by difference). During combustion, catalysts are typically added to achieve complete combustion, and absorbents are used to remove potential contaminants that may have formed (Thompson Michael, 2008).

As shown in *Figure 16,* in addition to the Helium line, an oxygen supply line is also required. This oxygen needs to be of high purity (minimum 99,9995%) to minimize the nitrogen 'blank' contribution during the analysis to a negligible level (Thompson Michael, 2008).

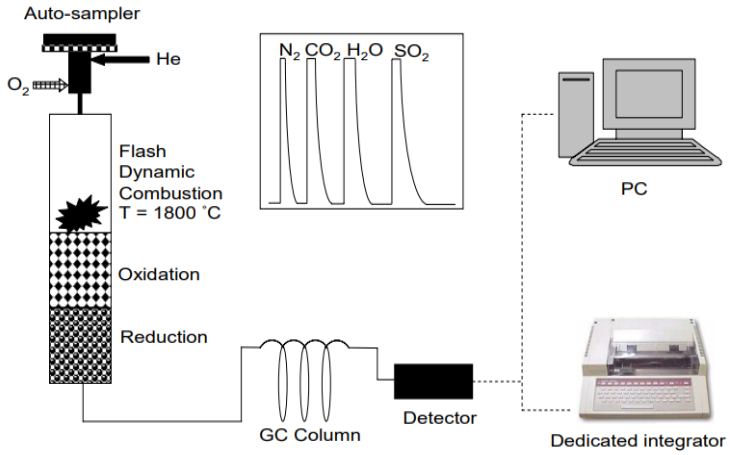

Figure 16: CHNSO scheme (Thompson Michael, 2008)

The results of the elemental analysis are expressed as a percentage by weight of the original sample, which is usually very small in size. Therefore, it was necessary to weight the starting sample very accurately using a precision balance (23 ± 3 mg) with the use of spatulas and tweezers. It's important to avoid the presence of any traces of contaminants inside the tare containers, which are small aluminium crucibles.

In this study, the elemental analyser is a *CHNS MacroCube from Vario NC Technologies*, as shown in *Figure 17*. It consists of the analyser, furnace, a TCD detector, a 60-position autosampler, and instrumentation for control and data analysis (*CHNS MacroCube*, 2023).

Figure 17: CHNS MacroCube from Vario NC Technologies (CHNS MacroCube, 2023)

5.2.4 UV-Visible Spectroscopy

The Ultraviolet-visible (UV-vis) spectroscopy technology holds particular significance in the study of materials for dye adsorption from wastewater. In fact, to assess the amount of residual methylene blue dissolved in water after an adsorption process, one can proceed by measuring the solution's absorbance: electromagnetic radiation passes through the solution and is absorbed according to the pollutant concentration (Pellenz et al., 2023).

Specifically, the **Lambert-Beer law** (*eq. 1*) underlies absorbance spectroscopy:

$$A = \varepsilon(\lambda) b C \qquad (eq.\ 1)$$

Where:

- **A** (-) = absorbance of light energy or electromagnetic radiation, that excites electrons of the compound under analysis from ground state to first excited state.
- **ε** ($M^{-1}cm^{-1}$) = molar absorptivity of the compound in solution, also called extinction coefficient; it's function of λ.
- **λ** (nm) = wavelength of incoming radiation; the UV-visible energy range in the electromagnetic spectrum spans from 1,5 to 6,2 eV, corresponding to a wavelength range of 800 to 200 nm.
- **b** (cm) = path length of the cuvette, equal to 1 cm.
- **C** (M) = concentration of the solution (Pellenz et al., 2023)

For a quantitative analysis, in the case of Methylene Blue the molar absorptivity is measured at λ = 664 nm, that represents the value of λ at which ε exhibits a maximum absorption. Therefore, the analysis of an unknown solution must be conducted at the same wavelength.

The absorbance (*eq. 2*) is the intensity of electromagnetic radiation that is absorbed by a substance and can also be defined as:

$$A = -\log\left(\frac{I}{I_0}\right) \qquad (eq.\ 2)$$

It is function of I_0 and I, that are the intensities of the incident light and the light emerging from the sample at a given wavelength (*Assorbanza*, 2023). The ratio between the two is defined as transmittance (T).

For sufficiently low concentrations, absorbance is linearly related to the concentration of a sample according to Lambert-Beer's law: this law has validity only for diluted solutions, otherwise deviations from linearity may occur.

To minimize the measurement error (photometric error), the absorbance should always have values in the range of 0,2 - 0,8, starting from the construction of the calibration curve (*Spettrofotometria*, 2023).

A spectrophotometer has different components as shown in *Figure 18*:

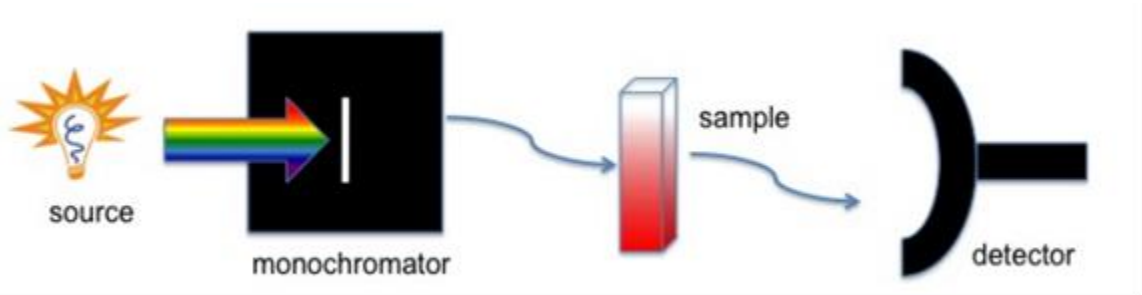

Figure 18: Working principle of a spectrophotometer (Pellenz et al., 2023)

A light source, usually a deuterium or tungsten lamp, emits a radiation that reaches a monochromator. The monochromator, acting as a prism, disperses the incoming polychromatic radiation into different wavelengths (monochromatic bands) through refraction and it's used to analyse one wavelength at a time. Subsequently, the radiation reaches the sample contained in a cuvette of 1 cm of length - namely a transparent container at the wavelength of interest - and goes through it until it finally reaches the detector. The detector then converts the intensity of the transmitted radiation into a proportional electrical signal, which is subsequently amplified and analysed by a computer. The final result consists of a diagram that shows the absorption intensity (y-axis) as a function of wavelength (x-axis) or of the absorbance at a specific wavelength(Pellenz et al., 2023).

To employ this technology, it's required to use a reference cell to zero the spectrophotometer with respect to the solvent (in this case, distilled water). Furthermore, it is necessary to create a calibration curve using solutions with known concentration of the compound to be analysed with the same solvent as the unknown samples (Pellenz et al., 2023).

During the experiments conducted in this thesis, two different spectrophotometers were used, each with their respective calibration curve, as the first had to undergo maintenance work:

- *DR 5000 Hach Lange* UV-vis Spectrophotometer (*Figure 19a*).
- *Biomate 6* UV-vis Spectrophotometer *Thermo scientific* (*Figure 19b*).

Figure 19: Spectrophotometers a) DR 5000, b) Biomate 6

The cuvettes had a volume of 4,5 mL and was made of plastic, with an optical path length of 1 cm. For measuring the concentration of MB in a solution, a volume of approximately 0,18 mL was pipetted and diluted with distilled water as a solvent until reaching a total volume of about 4 mL, ensuring it fell within the recommended absorbance range of 0,2 – 0,8 as previously said. The instrument was zeroed using a cuvette filled with distilled water. To minimize errors, the cuvette was handled only by its ridged sides, and to ensure proper measurement, the smooth sides were positioned to allow the optical path to pass through them.

The resulting calibration curves are shown in *Figure 20*:

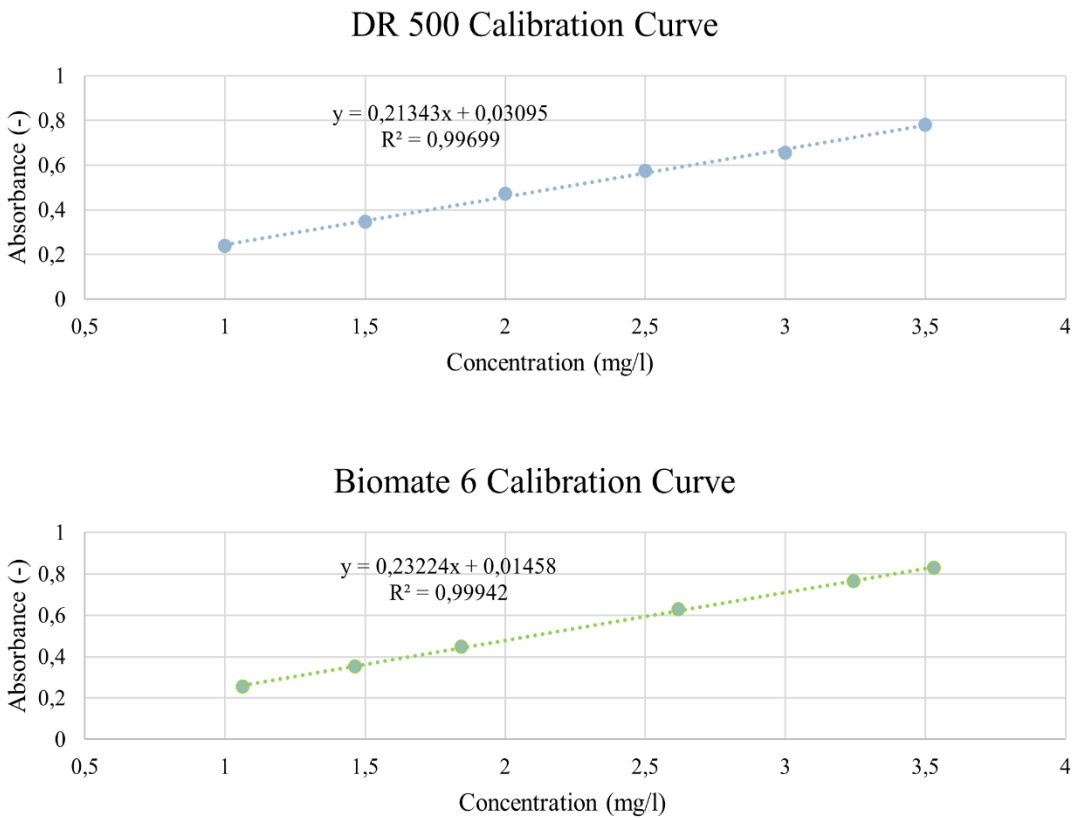

Figure 20: Calibration curves for a) DR 500 b) Biomate 6

The curves were determined starting from a stock solution of 100 mg/L and making dilutions from it, resulting in the concentrations shown on the horizontal axis of the graphs. The chosen concentrations fall within the validity range of Lambert-Beer's law (*eq. 1*).
From the data, the calibration curve was obtained using Excel's linear regression. The parameter R^2 indicates the goodness of linear fitting of the data and, since it's very close to 1, demonstrates good linearity in both cases.

5.2.5 pHmeter

A parameter that influences the adsorption of methylene blue is pH, so tests were conducted at varying pH levels. To measure pH, a pH meter (*Figure 21*) is required, where a probe is immersed in the sample solution and measures the difference in concentration of H+ ions between the inside and outside of the membrane. The probe is a glass electrode, which operates similarly to a battery: the difference in H+ ion concentration on either side of an ultra-thin glass membrane generates an electric potential proportional to the solution's pH. The electrode must be left in the solution long enough for H+ ions in the test solution to equilibrate with the ions on the surface of the glass electrode's bulb. This equilibrium provides a stable pH measurement.

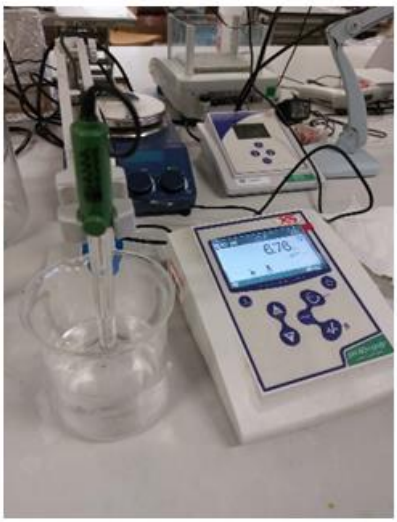

Figure 21: pH meter

The probe is then connected to an electronic device (voltmeter) that collects, amplifies, and converts the signal into a pH scale, calculating the corresponding pH value and displaying it on a screen.

The pH measurements were carried out using a *XS pH 80+ DHS digital benchtop pH meter* with an Ag/AgCl glass electrode. The pH meter was calibrated using solutions of known pH, typically before each use, to ensure measurement accuracy.
Between measurements, the electrode's body was rinsed with a continuous stream of distilled water until the pH displayed on the screen stabilized around neutral pH values of pH = 7.

5.3 Experimental setup

In this chapter, a comprehensive overview of the experimental setup will be provided, as it represents an important point for adsorption processes.

The most studied parameters for this process are:

- Initial dye concentration
- Adsorbent concentration
- Temperature
- Contact time
- Agitation speed
- pH

The selection of operational conditions was the result of a literature review, in order to align with the scientific community on the subject and to make comprehensive and systematic performance comparisons.

5.3.1 Effect of initial dye concentration

By comparing with the literature regarding adsorption experiments on activated carbon, biochar and hydrochar, like (El-Halwany, 2010), (Sharma et al., 2010), (Kannan & Sundaram, 2001), (Lin et al., 2013), (Karaca et al., 2008), (Adam, 2016), (Kuang et al., 2020), (Ghaedi et al., 2014), (Nworie et al., 2019), (Chen et al., 2019), it has been observed that an increase in the initial concentration of Methylene Blue leads to an increase of the actual amount of adsorbed MB (and so there is an enhancement in the adsorption capacity too, since it's defined as the amount (mg) of dye adsorbed per unit mass (g) of adsorbent), due to the increased driving force. This is so because the initial dye concentration provides the driving force to overcome the resistance to the mass transfer of dye between the aqueous and solid phase. The increase in initial concentration also enhances the interaction between adsorbent and dye (Sharma et al., 2010).

Additionally, it has been noted that the removal percentage of MB decreased, possibly due to the lack of available active sites on the adsorbent or the escalating repulsion force between adsorbed dye molecules and bulk ones. This effect is attributed to the fact that, at lower concentrations, there are enough active sites that the adsorbate can easily occupy. However, at higher concentrations, there is an insufficiency of available active sorption sites for the dye to occupy (Ghaedi et al., 2014).

5.3.2 Effect of adsorbent concentration

Adsorbent dose, among the other parameters, is an important factor that affects absorption performance and needs to be optimized for an efficient design of a wastewater treatment plant.

The effect of amount of adsorbent on the MB removal percentage is generally studied at different adsorbent doses, keeping constant the other variables. Analysing different papers as (El-Halwany, 2010), (Sharma et al., 2010), (Kannan & Sundaram, 2001), (Adam, 2016), (Kuang et al., 2020), (Ghaedi et al., 2014), (Chen et al., 2019), it can be noticed that at low adsorbent dose values, there's

a high ratio of dye molecule to vacant site, expressed as an insufficiency of reactive sites and so the removal percentage is low (Kuang et al., 2020).

Instead, with an increase in the mass of adsorbent, the removal rate of MB gradually increased, thanks to greater surface area and the availability of more adsorption sites (Kuang et al., 2020).

On further increase of the adsorbent dose, adsorption percentage did not increase anymore: the adsorption process approached an equilibrium point as the adsorbent mass reached a specific value. This is because at higher dosages of adsorbent, the quantity of available MB molecules in the solution is insufficient to fully combine with all the effective adsorption sites on the adsorbent, leading to the establishment of a surface equilibrium state and a subsequent reduction in adsorption capacity per unit mass of adsorbent (Kuang et al., 2020).

In fact, unlike the percentage of colour removal, which increases with an increase in adsorbent dosage, the amount of dye adsorbed decreased with higher adsorbent dosage. When the ratio of rice husk to solute concentration is higher, there is a rapid surface sorption onto the adsorbent, resulting in a lower solute concentration in the solution compared to situations where the biomass to solute concentration ratio is lower. The reduction in the quantity of dye adsorbed, represented as $\mathbf{q_e}$ (mg/g), as the mass of adsorbent increases, is a result of the concentration gradient between the solute concentration in the solution and the one on the surface of the adsorbent (Chen et al., 2019).

As the adsorbent mass increases, the amount of dye adsorbed per unit weight of adsorbent decreases, leading to a decrease in the q_e value with higher adsorbent mass concentration.

5.3.3 Effect of temperature

Compared to other parameters, temperature is a slightly less explored factor in the literature. The reviewed articles like (El-Halwany, 2010), (Lin et al., 2013), (Karaca et al., 2008), (Adam, 2016), (Kuang et al., 2020), (Ghaedi et al., 2014), highlight that an increase in temperature results in a significant increase in MB uptake (adsorption capacity), implying that altering the temperature will cause changes in the equilibrium capacity of the adsorbent for a specific adsorbate.

In reality, temperature has two primary effects on the adsorption process: aside from the aforementioned effect, elevating the temperature is known to accelerate the diffusion rate of adsorbate molecules across both the external boundary layer and the internal pores of the adsorbent particle. This phenomenon is due to the decrease in the solution's viscosity (El-Halwany, 2010).

The reasons that led to the increase in the adsorption capacity of MB as the temperature rises are: the enhanced adsorption rate of MB on the adsorbent surface may be attributed to a higher conversion of dimer species into monomers, resulting in a decrease in particle size for the adsorbate (MB) and subsequently an increase in the number of adsorbable species (El-Halwany, 2010); additionally, the thermal expansion leads to an increase in the pore structure and the number of active adsorption sites of the adsorbent (Kuang et al., 2020).

Finally, the notable increase in MB uptake with rising temperature demonstrates the endothermic nature of the adsorption process (Ghaedi et al., 2014).

5.3.4 Effect of contact time

The time during which the substances are in contact was the key factor affecting how well the MB dye was removed. Ensuring the adsorption process is faster is crucial for cost-effective methods. In wastewater treatment, it's important to reduce the time required to remove substances.

According to (Sharma et al., 2010), (Kannan & Sundaram, 2001), (Lin et al., 2013), (A. Ahmad et al., 2020), (Adam, 2016), (Kuang et al., 2020), (Ghaedi et al., 2014), (Nworie et al., 2019), (Chen et al., 2019), (Vadivelan & Vasanth Kumar, 2005), as the contact time increases, the rate of adsorption initially increases and then remains almost constant. It's observable that both the removal efficiency and the adsorption capacity of MB increase as the contact time increases, until they reach a maximum value.

The process can be divided into two phases (Kuang et al., 2020):

- **Fast adsorption**: the rate of adsorption of MB is very fast during the initial stage of the adsorption processes (5 – 30 min).
- **Slow adsorption**: after a fast initial rate of adsorption, the MB uptake capacity slowly increases with time and reaches equilibrium. The adsorption rate decreases and gradually stabilizes.

The concentration gradient is responsible for these changes in the adsorption rate. In the beginning, due to high concentration gradient, the driving force helps in the rapid adsorption. 4 There' s high available surface area and active sites, as the majority of dye molecules are still in the bulk phase, causing the driving force to be high (Ghaedi et al., 2014). During this step of fast adsorption, the rate of the dye transported from the solution to the surface of the adsorbent particles (diffusion through the film layer) is the controlling step of the MB adsorption rate (Kuang et al., 2020).

However, as the concentration gradient decreases with time, the rate is reduced until reaching equilibrium and this may be the reason why, after a particular time interval, removal efficiency remains almost constant (Sharma et al., 2010). During slow adsorption, the driving force is small, because the active sites and functional groups on the adsorbent are gradually saturated. The absorption rate of the dye is controlled by the dye molecules going from the exterior to the interior pore sites of the adsorbent particles (Kuang et al., 2020).

So, it can overall be said that in batch-type adsorption systems, a monolayer of adsorbate is typically formed on the adsorbent's surface. The speed at which this substance is removed from the liquid solution mainly depends on how quickly it moves from the outer sites of the adsorbent particles to the interior ones, corresponding to the slow adsorption phase mentioned before (Kannan & Sundaram, 2001).

At the equilibrium, the MB molecules desorbing from the adsorbent are in a state of dynamic balance with the amount of MB that re-adsorbs onto the substance. The time required to reach this condition is called equilibrium time and is usually used to estimate the adsorbate - adsorbent affinity (Lin et al., 2013).

In some cases, the removal efficiency can decrease with the contact time after a certain time, which may be due to a desorption process (Kannan & Sundaram, 2001).

5.3.5 *Effect of agitation speed*

Regarding the stirring rate, it was observed that beyond a certain threshold (120 - 150 rpm, as indicated in (Mahapatra et al., 2022) and (Karaca et al., 2008), changes in the agitation speed do not impact the concentration profiles.

This suggests that the adsorption rate is not influenced by the mixing rate, indicating that diffusion through the film layer is not the rate-controlling step for the overall adsorption process.

5.3.6 *Effect of pH and Point of Zero Charge*

This parameter is the most studied one among the others already analysed and its effects have been reported by (El-Halwany, 2010), (Sharma et al., 2010), (Kannan & Sundaram, 2001), (Lin et al., 2013), (Hamad & Idrus, 2022), (Karaca et al., 2008), (Kuang et al., 2020), (Ghaedi et al., 2014), (Nworie et al., 2019), (Chen et al., 2019), (Vadivelan & Vasanth Kumar, 2005).

The pH of the solution significantly impacts the adsorption capacity of the adsorbent (Le et al., 2021).

In general, the solution's pH can either enhance or inhibit the uptake of dye molecules by modifying both the surface properties of the adsorbent and the chemistry of the dye (Lin et al., 2013). This is attributed to the change of the charge of the adsorbent surface with the change in pH value.

In order to optimize the adsorption capacity, the so-called **point of zero charge** (PZC) should be analysed and used. To understand the meaning of PZC, the dissociation of surface groups should be considered (Prof. M. Vanni, 2023):

- Acidic dissociation can occur if there are acidic groups on the adsorbent's surface; it is proportional with the solution basicity, as by increasing pH, more dissociation occurs and H^+ go into the solution, making the surface negative. This process can be controlled by modifying the pH.
- During basic dissociation, instead, basic groups at the adsorbent's surface will lead to a positive surface, as OH^- will go into the solution leaving a positive charge on the material. Dissociation of basic groups is stronger with low values of pH.

If the surface has both acidic and basic groups, the surface can be positive or negative based on the pH value of the solution. For this reason, H^+ and OH^- are called *charge determining ions,* as they allow to manipulate surface charge.

When the surface charge is exactly equal to zero, it means that the extent of acid and basic dissociation is the same: the concentration of charge determining ions corresponding to surface charge equal to zero is the point of zero charge (Prof. M. Vanni, 2023).

When pH values are below the PZC of an adsorbent, anions are attracted to its surface; cations experience the same effect when pH values exceed the PZC.

For materials such as biochars, hydrochars, and activated carbons, an alkaline environment proves advantageous for the adsorption of MB dye. This is due to the fact that MB is a cationic dye and exhibits a preference for surfaces with a negative charge. At elevated pH levels, the adsorbent's surface becomes negatively charged, due to the presence of hydroxyl groups (-OH) and carbonyl groups (C=O). This shift in charge enhances the adsorption of the positively charged MB dye through electrostatic attraction. Consequently, both the rate of MB adsorption removal and the adsorption capacities increase as the pH rises (Kuang et al., 2020).

At lower pH, the dissociation of hydrogen ions (H^+) by oxygen-containing functional groups on the adsorbent is inhibited, resulting in a weaker electronegativity of the adsorbent; this weaker electronegativity leads to an electrostatic attraction force between the dye cation and the adsorbent that becomes repulsive in nature, causing a reduction in the removal percentage (Kuang et al., 2020).

Above specific pH thresholds, a slight decrease in adsorption might occur due to repulsion forces between the negatively charged adsorbent surface and the partial negative charge on MB caused by chloride ions (Sharma et al., 2010).

During the experiments at high pH, the final pH of the solution was found to decrease slightly (by 0,3 - 0,5 pH units) due to the release of H+ ion from the adsorbent surface's active sites (Kannan & Sundaram, 2001).

In conclusion, it is important to establish a procedure for determining the Point of Zero Charge (PZC), which enables understanding the pH value beyond which the adsorption is optimized for a cationic dye like MB. The procedure is outlined in section *5.3.7*.

5.3.7 Operational conditions

Among the effects listed in the preceding paragraphs, only a few have been selected for the current study due to time or logistical constraints. Specifically, the decision was made to analyse the effects of adsorbent concentration, contact time, and pH.

For the selection of the ranges in which to vary these parameters and for the setup of the experiments, a comparison with the literature was conducted, as shown in *Table 4*:

Table 4: Literature review of MB adsorption operational conditions

Adsorbent	MB concentration (mg/L)	Adsorbent dose (g/L)	Solution volume (mL)	Agitation speed (rpm)	Time (h)	Reference
AC	3,8 – 14,7	0,025	200	-	6,6	(S. Wang et al., 2005)
AC	250	1 - 10	100	-	1	(Okeola & Odebunmi, 2010)
AC	7 - 20	1,8	-	-	0,75	(Ghaedi et al., 2014)
AC	20 - 200	1	100	150	24	(Paluri et al., 2020)
RHAC	50 - 500	0,5	200	120	2	(Lin et al., 2013)
RHAC	25 - 125	0,5–1,5 10^{-3}	50	-	2,6	(El-Halwany, 2010)
RHAC	10	0,005	70	250	4	(Phuong et al., 2015)
RHAC	32	0,1 – 0,35	100	-	8	(Ahiduzzaman & Sadrul I., 2016)
RHAC, CAC	100 - 900	1 – 11,6	50	200	2	(Kannan & Sundaram, 2001)
RHBC	100	5	100	-	84 - 96	(A. Ahmad et al., 2020)
RHBC	100	0,6 - 4	50 - 1000	800	48	(Vadivelan & Vasanth Kumar, 2005)
RHBC	100	2 - 4	50	-	24	(Y. Wang & Liu, 2017)
RHBC	10 - 500	16	30	100	24	(Quansah et al., 2020)
RHBC, RHHC	20	4	25	100	0,5	(Jian et al., 2018)
RHBC, RHHC	5 - 250	2	200	-	4	(Lang et al., 2021a)
CAC	50 - 500	1 - 10	50	150	2 - 30	(Mahapatra et al., 2022)
CAC	100 - 180	1	100	90	0,5	(Karaca et al., 2008)
CAC	60 - 120	2	100	200	4	(Adam, 2016)
CAC	100 - 275	0,44	1500	800	2,3	(Kumar, 2006)
BC	10 - 500	3 - 15	30	150	2	(Lonappan et al., 2016)
RHBC, RHHC, CAC	50	0,25 – 0,5 – 1	200	280	6	This study

As reported in the last row of the table, during the adsorption experiments, a Methylene Blue solution in distilled water with a concentration of 50 mg/L was used. This solution was prepared in a 400 or 600 mL becker by mixing 200 mL of distilled water with 0,01 g of powdered MB. The solution was placed on a plate and stirred using a magnetic stir bar for one hour to ensure its homogeneity.

Figure 22 shows different stirred beckers containing the initial solution of MB at 50 mg/L.

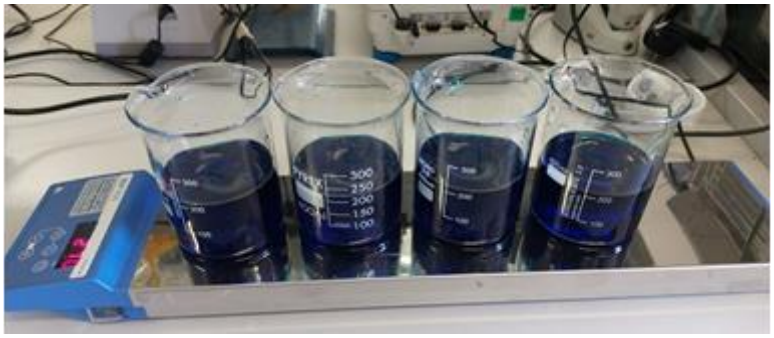

Figure 22: Initial solutions of MB at 50 mg/L

For the adsorbent dosage, three different values were explored (0,25 - 0,5 - 1 g/L), in accordance with the literature. Correspondingly, 0,05, 0,1, and 0,2 g of each adsorbent material were weighed and placed into the beckers containing the solution. Almost all tests were conducted in triplicate, with a few in duplicate, for a total time of 6 hours per experiment to observe the impact of contact time.

Figure 23: Setup for pH measurements

For the experiments regarding pH, tests were conducted at pH = 10 and pH = 11,5 using 400 mL beckers with 200 mL of a 50 mg/L MB solution. A single adsorbent dosage value of 0,5 g/L was explored to observe the pH effect. The desired pH was achieved by adding NaOH using a pipette and was monitored using a pH meter (*Figure 23*) and/or pH indicator paper. The total duration for each test was 6 hours.

Throughout all the experiments, room temperature and a constant agitation speed of approximately 270 rpm were maintained, as the latter had no influence on the adsorption process.

For the determination of the **Point of Zero Charge** (PZC), a salt solution of 0,01 M NaCl was prepared as the stock solution, in a volume of 600 mL. Then, 25 mL of this solution was poured into each 100 mL becker. To achieve the desired pH values ranging from 2 to 12, a 0,1 M NaOH solution (in pellet form) and a 98% HCl solution were utilized, added dropwise using a pipette. The pH was monitored using a pH meter and/or pH indicator paper.
In each becker, 0,125 g of adsorbent was added, and Parafilm was used to cover the beckers to prevent solution evaporation. In total, there were 6 beckers for each adsorbent material, representing pH = 2, 4, 6, 8, 10, 12.
The PZC experiments were conducted in duplicate at room temperature and under agitation using a magnetic stir plate for a total duration of 24 hours at a speed of 60 rpm.

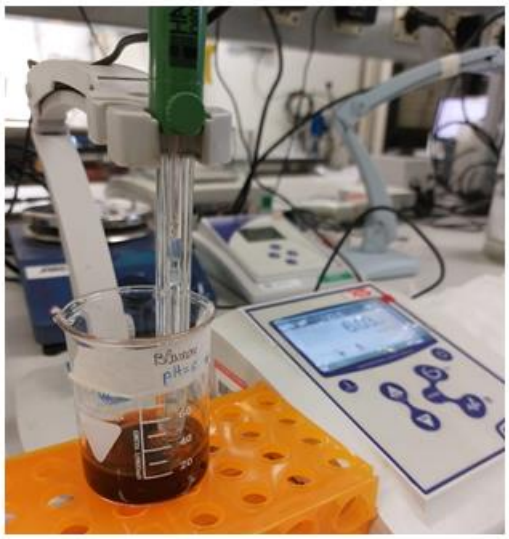

Figure 24: Determination of PZC

After this time period, the pH inside each becker was measured again *(Figure 24*) and compared with the initial starting value. Using these values, a graph was created with the initial pH on the x-axis and the difference between final and initial pH on the y-axis. The point at which the vertical axis parameter reached zero corresponds to the Point of Zero Charge pH, read on the horizontal axis.

5.4 Procedure

In this section, the procedure for the data collection during the adsorption experiments will be presented. To ensure accuracy and reproducibility, almost all experiments have been conducted twice or even more, so this will be specified.

For the adsorption experiments, the first step involved sampling the MB solution before adding the adsorbent material. This initial step is crucial to precisely determine the actual initial concentration of MB, as 50 mg/L is just a nominal value and experimental errors could lead to deviations. Samples were collected by pipetting 1,5 mL from a 3 mL Pasteur pipette into a 15 mL Falcon conical tube. The collected sample was analysed using a UV-vis spectrophotometer, as explained later, following the same procedure.

After collecting the initial solution sample, the adsorbent material was added to the becker. Any adsorbent residue was carefully recovered by rinsing the pipette with the solution itself. The stopwatch was then started, with this point considered as time zero.

Sampling was conducted every 5 minutes during the first hour, every 15 minutes during the following hour, and every 30 minutes for the remaining 4 hours, totalling six hours. One minute before each sampling, agitation was paused to allow adsorbent particles to settle at the bottom of the container. Using a pipette, only the supernatant (approximately 1,5 mL) was collected. The collected amount was placed in a 15 mL conical bottom Falcon tube, allowing any remaining adsorbent residues to settle for a few minutes.
Subsequently, the supernatant was extracted from the Falcon tubes using a pipette, and 0,75 mL was transferred to 1,5 mL Eppendorf tubes. To ensure the removal of any residual adsorbent particles that could affect proper spectrophotometer readings, the Eppendorf tubes were centrifuged using a centrifuge named *CAPP CR1512* at 10000 rpm for two minutes (*Figure 25*).

Figure 25: Centrifuge CAPP CR1512

The content of the Eppendorf tubes was then carefully retrieved from the surface and diluted into cuvettes made of quartz with a volume of 4,5 mL, using distilled water to bring it within the absorption range defined by the calibration curve of the UV-vis spectrophotometer (*Figure 26*).

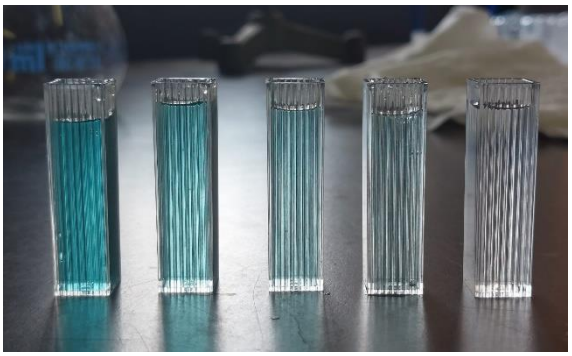

Figure 26: Example of cuvettes filled with MB solution at different times

At this point, the cuvettes were analysed using the spectrophotometer at a wavelength of 664 nm. Prior to the analysis, the cuvettes were agitated to ensure proper mixing of the solution with the dilution water, and a blank reading was taken using a cuvette containing only distilled water.
The values obtained from the instrument were recorded and analysed as explained in the following paragraph.

After the 6-hour period, the agitation was kept constant for another 18 hours, and the final sample was taken at the end of this period. This step was taken to assess the potential attainment of equilibrium conditions in the adsorption process or any long-term effects. The analysis of this final sample followed the same steps used for the other samples.

In the experiments at pH = 10 and pH = 11,5, the procedure followed was exactly the same, with the addition that the pH was not continuously monitored but checked using a pH meter every hour and, if necessary, adjusted with NaOH. After each check, the pH meter was thoroughly rinsed with distilled water until a consistent pH value appeared on the display when immersed in a becker of pure distilled water.

For determining the Point of Zero Charge, after 24 hours in the shaker, the Parafilm was removed and the final pH of each becker was measured using a pH meter. After each measurement, the pH meter was thoroughly cleaned as previously mentioned.

As highlighted in the previous paragraph, the experiments were conducted in duplicate and, at times, even in triplicate, in order to ensure better accuracy and reproducibility.

5.5 Data analysis

In this section, the methods employed for the analysis of experimental data will be described, in reference to the current literature. Specifically, during an adsorption process, it is essential to examine both kinetic and thermodynamic models to gain a comprehensive understanding of the phenomenon. Moreover, statistical methods were employed for data analysis, implemented using Excel.

5.5.1 Kinetic models

The study of adsorption dynamics describes the adsorbate uptake happening at the interface between the solid and the solution and its residence time. The prediction of batch adsorption kinetics is relevant for the design of adsorption columns for industrial use.
Various mathematical models have been developed to describe the kinetics of adsorption, including classical models like the **pseudo-first order** and **pseudo-second order** models, as well as more complex ones like the Elovich, Avrami, Crank, Vermeulen, Weber-Morris, Bangham, linear film, mixed surface reaction and diffusion, and multi-exponential models.
Among these, the adsorption kinetics are frequently represented using the pseudo-first and pseudo-second order rate equations. In fact, an analysis of previously published works over the past two decades, as highlighted in the referenced article (Revellame et al., 2020), has shown that the pseudo-second order model is often preferred due to its ability to effectively describe a wide range of adsorption systems.

A careful evaluation of modelling methods and conventions implies that the apparent superiority of the pseudo-second order model might derive from modelling trends that tend to prioritize this model. This preference has arisen due to several modelling pitfalls that are frequently ignored. Moreover, frequently employed techniques for model validation are often applied in a disorganized and repetitive manner; consequently, these techniques are insufficient to offer assurance on the accuracy of a model. To address this modelling bias, a novel validation approach that combines numerical and visual tools has been introduced by (Revellame et al., 2020).

The first and second order models are derived from Langmuir adsorption kinetics (Revellame et al., 2020), which is defined as follows (*eq. 3-5*):

$$\frac{dq(t)}{dt} = k_1[q_e - q(t)] + k_2[q_e - q(t)]^2 \qquad (eq.\ 3)$$

With:

$$k_1 = \left[k_a^2(C_0 - q_{max}X)^2 + 2k_a k_d(C_0 + q_{max}X) + k_d^2\right]^{\frac{1}{2}} \qquad (eq.\ 4)$$

$$k_2 = k_a q_{max} X \qquad (eq.\ 5)$$

Where:

- q(t) = amount of adsorbate adsorbed at time t
- q_e = amount of adsorbate adsorbed at equilibrium
- q_{max} = maximum adsorption capacity of the adsorbent
- k_a = adsorption rate constant
- k_d = desorption rate constant
- C_0 = initial adsorbate concentration
- X = adsorbent dosage

In cases where the value of q_e is much smaller than the ratio of k_1/k_2, the equation reduces to a first order rate expression, corresponding to the Lagergren's pseudo-first order rate expression (*eq. 6*):

$$\frac{dq(t)}{dt} = k_1[q_e - q(t)] \quad (eq.\ 6)$$

The boundary conditions are that at time t = 0, q(0) = 0, and at time t, q(t) = q(t). Below is the integrated form, and from it, its linearization is provided (*eq. 7- 8*):

$$q(t) = q_e\left(1 - e^{-k_1 t}\right) \quad (eq.\ 7)$$

$$\ln[q_e - q(t)] = -k_1 t + \ln q_e \quad (eq.\ 8)$$

In the case of the opposite scenario, the equation simplifies to a second-order expression, resulting in the pseudo-second order rate expression, which, after integration, becomes (*eq. 9*):

$$q(t) = \frac{q_e^2 k_2 t}{1 + q_e k_2 t} \quad (eq.\ 9)$$

Its linearized form is (*eq. 10*):

$$\frac{t}{q(t)} = \frac{1}{q_e} t + \frac{1}{k_2 q_e^2} \quad (eq.\ 10)$$

The use of **linear regression** proves is very useful as it allows plotting the results in a straight line and directly determining the unknown parameters of the equation from the intercept and slope of the line. For this reason, the most common approach to determining adsorption kinetic parameters or modelling the adsorption process is to use the linearized form of the models.

For the linear modelling of first-order kinetics, experimental data collected are plotted as ln[q(e) – q(t)] vs. t. From the slope (m), the value of parameter k_1 can be obtained, as k_1 = - m, while from the intercept (b), the value of q_e is derived, as q_e = exp(b).

For second-order kinetics, on the other hand, the plot represents t/q(t) vs. t, and by using the slope and intercept, k_2 can be obtained as $k_2 = m^2/b$ and q_e can be derived as q_e = 1/m.

Indeed, linearization also comes with disadvantages that cannot be ignored. As highlighted by (Revellame et al., 2020), the conversion of kinetic data to fit the linear forms of the model introduces uncertainty and bias that are frequently disregarded. The linear transformation of the pseudo-first order model into logarithmic scale leads to a discontinuity at equilibrium, favouring the linear pseudo-second order model even for datasets that naturally follow the pseudo-first order. This discontinuity also causes a disparity in the number of data points usable for fitting the two models, with pseudo-second order modelling often having access to more data points. Under the established modelling approaches, a notable bias towards the pseudo-second order occurs when all data points are at equilibrium. In such cases, pseudo-first order is automatically excluded while pseudo-second order exhibits a linear fit which is almost perfect.
Furthermore, the linearized first-order model also requires prior knowledge of the q_e value, which is not always available.

An alternative is provided by **nonlinear modelling** (Revellame et al., 2020).
It involves the use of a predefined objective function (OF), such as the sum of the squares of the distances between experimental and predicted values of the response variable. In this case, the objective is to minimize this function (*eq. 11*):

$$OF = \sum_{i=1}^{n}(y_i - \hat{y}_i)^2 \qquad (eq.\ 11)$$

Where:

- y_i = experimental response for i^{th} observation
- $\hat{y}_i$ = calculated or predicted value of y_i
- n = total number of observations or data points

Nonlinear modelling has been proposed as a better method when compared to linear regression, as it yields more realistic kinetic parameters. This approach also removes the necessity of knowing any parameters a priori and eliminates any model discontinuities. Consequently, this modelling approach treats both models in the same way, offering a more precise comparative evaluation to determine the model that best fits a given kinetic dataset.

Furthermore, employing nonlinear modelling addresses a common pitfall inherent in linear modelling: the uneven distribution of data points. The transformation of data for linear modelling results in the exclusion of data beyond equilibrium for pseudo-first order and pseudo-second order modelling, respectively. This leads to an unequal distribution of data points available for analysis. The number of data points directly impacts the degrees of freedom (which is a function of the number of data points and model parameters), consequently affecting validation methods such as R^2 used to assess model quality.
Nonlinear modelling, however, enables the utilization of all data points, allowing for a direct comparison between the first and second-order kinetics with an equal number of data points.

For this reason, in this study, the choice was made to employ nonlinear modelling and the followed procedure is hereafter illustrated.

The experimental data, including equilibrium concentration C_e, time and concentration at that time were inputted into an Excel Spreadsheet and the amount of dye adsorbed at equilibrium and at time t were calculated according to (*eq. 12*):

$$q_t = \frac{(C_0 - C_t)V}{m} \qquad (eq.\ 12)$$

Furthermore, concentrations were normalized to 1 to eliminate the influence of small variations of initial concentration of MB during the preparation of the initial solution. The normalized concentration data were averaged across the available replicates, and from the result, q_t was calculated using the previously described formula. The removal efficiency was also calculated, and graphs were made.

Since the nonlinear regression analysis is an iterative process, it is necessary an initial estimation of the unknown parameters of the model. In this case, the results obtained from linear regression were exploited: starting from experimental data, the linear regression approach was followed for the pseudo first-order and pseudo second-order models and model parameters were extracted from the slope and intercept of the graphs (respectively, $\log(q_e\text{-}q_t)$ vs t for pseudo-first order and t/q_t vs t for pseudo-second order). These parameters were used as initial values for the iterative process of nonlinear regression.

Non-linearized form of the pseudo-second and pseudo-first order rate expression were used to calculate q(t) and a comparison with the experimental q(t) was performed, in order to obtain the error between the experimental data and the model output. These differences were summed to visualize the SSE, the sum of squared estimate of errors of the model, also known as sum of squared residuals (SSR); this is the objective function to be minimized (*eq. 13*):

$$SSE = \sum_{i=1}^{n} \left(q_{t,exp} - q_{t,calc}\right)^2 \qquad (eq.\ 13)$$

Successive iterations are carried out by making slight adjustments to the initially estimated parameters and then recalculating the sum of squared errors SSE multiple times until the parameter values yield in the smallest value of SSE achievable. In particular, this step was performed by exploiting the *Solver* add-in functionality of the Microsoft Excel spreadsheet. The function to be minimized was the SSE, by changing q_e and k_1 for the pseudo-first order kinetic and q_e and k_2 for the pseudo-second order kinetic. The method used was GRG Nonlinear, which converges very quickly, but provides a local minimum value.

As a further step, starting from the values obtained from the method GRG Nonlinear, the method Evolutionary was employed to confirm that it was an absolute minimum value, since this method is slower, but allows finding the point of absolute minimum.

Finally, R^2 and adjusted R^2 were calculated.

5.5.2 Validation techniques

Validation is an essential aspect of any modelling process, even if it tends to be neglected or assigned a lower level of importance. This step is used to assess the quality of fit achieved by the model.

Each validation method serves as a metric to measure how low the model error is (also called "residual"), that can be defined as (*eq. 14*):

$$e_i = y_i - \hat{y}_i \qquad (eq.\ 14)$$

In case of adsorption processes, it represents the difference between experimental data and calculated values predicted by the model (*eq. 15*):

$$e_i = q_{t,exp} - q_{t,calc} \qquad (eq.\ 15)$$

The most used validation criterion in modelling adsorption kinetic data is the coefficient of determination R^2 (*eq. 16*), (Revellame et al., 2020):

$$R^2 = 1 - \frac{\sum_{i=1}^{n}(y_i - \hat{y}_i)^2}{\sum_{i=1}^{n}(y_i - \bar{y})^2} \qquad (eq.\ 16)$$

Where $\bar{y}$ is the mean of the observed data.

A modified version of R^2 is called Adjusted R squared (*eq. 17*) and it takes into account for degrees of freedom for model validation through the variable p, which is the total number of model parameters:

$$R^2_{adj} = 1 - \frac{(1-R^2)(n-1)}{n-1-p} \qquad (eq.\ 17)$$

A model that accurately fits a dataset will have R^2 or Adjusted R^2 values closer to unity. They are numerical validation tools like many others, but only one of these methods is truly necessary, as using more would be redundant, not providing any additional useful information.

Model validity can also be assessed through qualitative or graphical examination of residuals. Unlike numerical validation methods, graphical residual analysis focuses on analysing the behaviour of residuals for each data point, to verify that specific modelling assumptions concerning model error are valid.
These assumptions involve the independence (**randomness**) and **normal distribution** of errors. In the process of comparing different models, the model to be preferably chosen is the one exhibiting residuals that closely follow normal behaviour.

To ensure the robustness of the fit, graphical validation techniques should be incorporated as supplementary tools to numerical ones, as graphical methods rely on the examination of model residuals. Graphical methods offer an advantage: they can effectively visualize the complex relationships between the model and the data. Instead, numerical techniques tend to have a narrower focus on a specific aspect of the model-data relationship, summarizing that information into a single

descriptive value. These graphical validation methods are not suitable when the number of estimated parameters is relatively close to the dataset's size.

The following section outlines the suggested validation criteria for the modelling of adsorption kinetics using non-linear techniques according to (Revellame et al., 2020).

This study followed the specified criteria:

- **R^2**, already specified. It is often coupled with the model parameter q_e to support the suitability of a model fit. For comparative model evaluation, R^2, instead of R^2 adjusted, can be utilized as long as the same number of data points is employed and both models have an identical number of parameters.
  An R^2 value exceeding 0,8 indicates a satisfactory fit between the data and the model. However, R^2 alone is insufficient for model validation. The model with the higher R^2 (closer to 1) is not necessarily always the accurate one, hence additional validation methods are necessary.

- As previously mentioned, the model residuals need to be normally distributed and random in order to the model to be valid. In this study, the verification of the normality assumption was conducted using a **normal probability plot** of the residuals.
  The procedure followed for constructing the plot involved the following steps (Revellame et al., 2020):

  1. Calculating the residual, also referred to as error, for each data point. This involves finding the difference between the experimental value and the predicted value based on the kinetic model.
  2. Arranging the residuals in ascending order.
  3. Assigning a position, denoted as $'i'$, to each residual, ranging from 1 to m, where m represents the total number of residuals.
  4. Calculating the probability for each data point using the formula $100(i\text{-}0{,}5)/m$.
  5. Creating a plot of residuals against their corresponding probabilities.
  6. Analysing the normal probability plot. Ideally, the residuals should approximately follow a straight line in this plot. It's important to pay more attention to the central values of the plot rather than the outliers when assessing the straightness of the line.

- Regarding the assumption of **randomness**, non-randomness in residuals was evaluated through tests for potential time effects, non-constant variance, and curvature. These tests were conducted graphically by creating plots where the residuals are plotted against the time and against the corresponding calculated values ($\hat{y}_i$).
  The time order plot is helpful for identifying whether the timing of data collection has contributed to a correlation among residuals. This could be linked to factors like experimenter skills (which might vary over time) or ambient conditions (certain reactions are influenced by environmental factors). These situations can lead to alterations in residual variability over time. When the model is accurate, residuals should lack any recognizable pattern and should not be connected to any other variable. Therefore, a plot showing residuals against predicted values is essential to uncover any evident patterns that might be linked to errors.

Acceptable residual plots exhibit a relatively consistent horizontal band of data points. However, confirming the non-random nature of residuals alone is not comprehensive enough as a validation measure. It's crucial to incorporate normality testing as well to accurately evaluate the appropriateness of models.

The normality test can help identify potential outliers, while the stochastic test can reveal possible effects of conditions during data collection. These insights can guide in determining whether it's necessary to explore alternative kinetic models to better fit the dataset. It's important to note that minor deviations from ideal or standard graphical tests shouldn't automatically disqualify a model.

5.5.3 Thermodynamic models

Adsorption equilibrium is fundamental for the comprehension, analysis and design of adsorption processes and it offers physicochemical information to assess the suitability of adsorption as a unit operation (Vadivelan & Vasanth Kumar, 2005).
Equilibrium studies provide the value of adsorbent capacity and are described by adsorption isotherms, that typically represent the ratio between the amount of substance adsorbed and the amount remaining in the solution at equilibrium at fixed temperature (El-Halwany, 2010).
The Freundlich and Langmuir isotherm equations are the most frequently employed equilibrium relations (Vadivelan & Vasanth Kumar, 2005).

The **Langmuir** equation is employed to predict the maximum adsorption capacity, which corresponds to the complete formation of a monolayer on the adsorbent surface. In fact, the theoretical Langmuir sorption isotherm is based on several assumptions and the first one is that it assumes that the maximum adsorption occurs when a saturated monolayer of solute molecules is present on the adsorbent surface. It also assumes that the energy of adsorption is constant and that there is no migration of adsorbate molecules in the surface plane (Senthil Kumar et al., 2011).
It is mathematically expressed as (*eq. 18*):

$$q_e = \frac{(q_{max} K_L C_e)}{(1 + K_L C_e)} \qquad (eq.\ 18)$$

Where C_e indicates the equilibrium concentration in solution (mg/L), q_{max} the maximum adsorption capacity and K_L is the Langmuir energy constant related to the heat of adsorption.

The rearranged linearized form (*eq. 19*) of the equation is expressed as:

$$\frac{C_e}{q_e} = \frac{1}{q_{max} K_L} + \frac{C_e}{q_{max}} \qquad (eq.\ 19)$$

The experimental data is fitted into the linearized equation by plotting C_e/q_e against C_e, from which K_L and q_{max} can be derived.

The **Freundlich** equation is an empirical equation for the estimation of the adsorption intensity of the adsorbent towards the adsorbate. This model is applicable to adsorption on heterogeneous surfaces, where it describes the interaction between adsorbed molecules and the sorbent. Freundlich equation says that adsorption energy decreases exponentially as all the adsorption sites of an adsorbent become saturated (Senthil Kumar et al., 2011).
It is expressed as follows (*eq. 20*):

$$q_e = K_F C_e^{\frac{1}{n}} \qquad (eq.\ 20)$$

The 'n' value indicates the adsorbate-adsorbent affinity, while K_F is a Freundlich constant with units of $(mg/g)(L/mg)^{1/n}$ that gives information about bonding energy. The parameter 1/n represents the heterogeneity factor, and n quantifies the deviation from linearity (Senthil Kumar et al., 2011):

- If n = 1, adsorption is linear.
- If n < 1, adsorption is considered a chemical process.
- If n > 1, adsorption is a physical process.

The equation is commonly employed in a linearized form (*eq. 21*) as follows:

$$\ln q_e = \ln K_F + \frac{1}{n} \ln C_e \qquad (eq.\ 21)$$

A linear plot of $\ln C_e$ against $\ln q_e$, resulting in a straight line, implies that the data are following the Freundlich adsorption isotherm. The values for the constants 1/n and $\ln(K_F)$ can be extracted from the slope and intercept of the line, respectively.

In this study, these isotherms were initially employed in their linear form to determine initial values of model constants by extracting the slope and intercept from the plots.
Subsequently, starting from these values, nonlinear isotherms were used, following the same approach as the one illustrated in section *5.5.1*. The nonlinearized isotherms were applied to the experimental data using the values found by applying linearized isotherms. Then, the error between the values predicted by the model and the experimental data was calculated. The sum of these squared errors (SSE) was found and subsequently minimized by slightly varying the constants' values according to the Excel-based method GRG non-linear employed in the Solver Add-in. Finally, the value of R^2 was calculated to assess the quality of the fit.

5.6 Batch Adsorber design

The results obtained during the experimental tests were then applied for the practical design of a single-stage batch adsorber, in order to gain a general overview for a potential process scale-up. Thermodynamic results are especially necessary for the design.

An adsorber aims to reduce the initial concentration of Methylene Blue, C_0 (mg/L), to a final value, C_1 (mg/L), as required by the regulations.
What occurs during the adsorption process inside a single-stage batch adsorber can be schematically represented as follows (*Figure 27*), where V (L) indicates the volume of the aqueous solution, M (g) indicates the quantity of adsorbent, and q (mg/g) indicates the mass of solute divided by the mass of adsorbent:

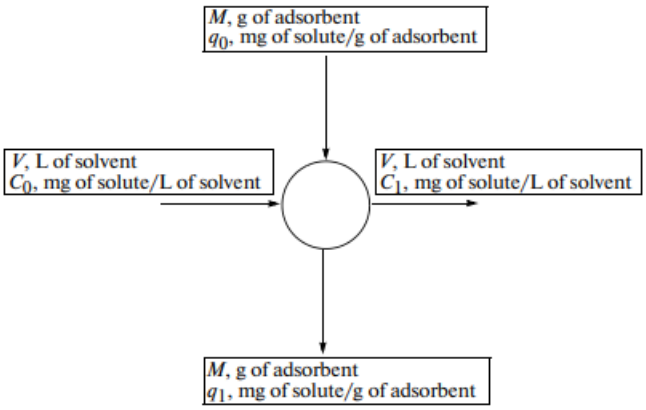

Figure 27: Scheme of a single-stage batch adsorber (Senthil Kumar et al., 2011)

The diagram is based on a mass balance between the MB removed from the aqueous solution (left-hand side of the *eq. 22*) and the amount of MB adsorbed by the adsorbent material (right-hand side of the *eq. 22*):

$$V(C_0 - C_1) = M(q_1 - q_0) = Mq_1 \qquad (eq.\ 22)$$

The value of q_0 is equal to zero because there's no adsorption at initial time. At equilibrium conditions, the final concentration C_1 tends towards the equilibrium concentration (C_e), as well as q_1 tends to q_e:

$$C_1 \rightarrow C_e \text{ and } q_1 \rightarrow q_e$$

At this point, it is possible to replace q_e with the expressions from the thermodynamic models (e.g., Langmuir, Freundlich, etc.). For example, using the Freundlich isotherm and reformulating the equation, the resulting relationship is (*eq. 23*):

$$\frac{M}{V} = \frac{(C_0 - C_1)}{q_1} = \frac{(C_0 - C_e)}{q_e} = \frac{(C_0 - C_e)}{K_F C_e^{1/n}} \qquad (eq.\ 23)$$

In this study, an incoming stream with an initial MB concentration of 50 mg/L was assumed, and to obtain the final equilibrium concentrations, different scenarios were hypothesized, with removal percentages of 70, 75, 80, 85, and 90%. The values found during the data analysis in the previous chapter were used as the parameters of the isotherms, thus making it possible to derive the value of q_e to be inserted into the previous equation.

Finally, starting from this, a graph was constructed to determine the quantity of adsorbent material (y-axis) required for the removal of MB at different removal percentages, as a function of the solution volume (x-axis), which was varied between 2000 and 20000 L, considering various scale-up scenarios.

6. Results and Discussion

This chapter presents the outcomes of the characterization conducted on four different materials as described in chapter *5*, related to Materials and Methods. Furthermore, data collected regarding the experiments on Methylene Blue adsorption are presented, highlighting the influence of the following parameters:

- Initial adsorbent concentration
- Solution pH
- Contact time

An analysis of the adsorption mechanisms and their relationship to the properties of the adsorbents will be provided, followed by a discussion on adsorption kinetics and isotherms.

Comparisons with existing literature will be made, and additionally, results regarding scaling up for practical applications will be discussed.

6.1 Materials characteristics

Concerning the surface morphology analysis, the field-emission scanning electron microscope was firstly employed for the study of raw rice husk. It showed a surface topology with an absence of any kind of pore, as shown in *Figure 28*.

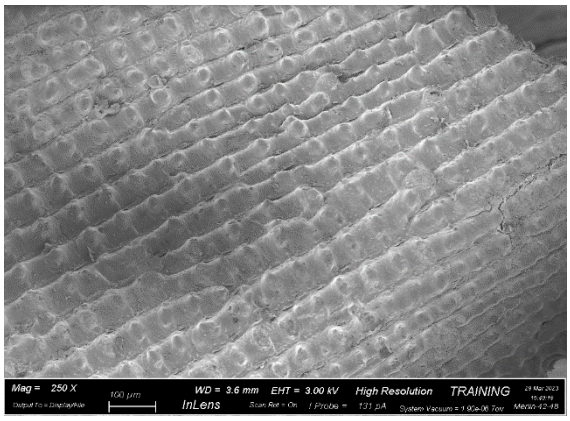

Figure 28: FESEM image of raw rice husk

The FESEM images of rice husk biochar showed that it preserved the original fiber-shaped structure of the raw rice husk, with the presence of quite uniform pores created during the pyrolysis (Phuong et al., 2015). In fact, after pyrolysis, the original smooth structure of raw rice husk was broken down by the release of volatile compounds of the biomass matrix, induced by the reactions (Jian et al., 2018).

From cross-section images, the pore size in the range of 3 - 8 µm of diameter indicates that these visible pores can be categorized as macropores (> 50 nm). These considerations apply to both CO_2 biochar and N_2 biochar, as shows in *Figure 29*.

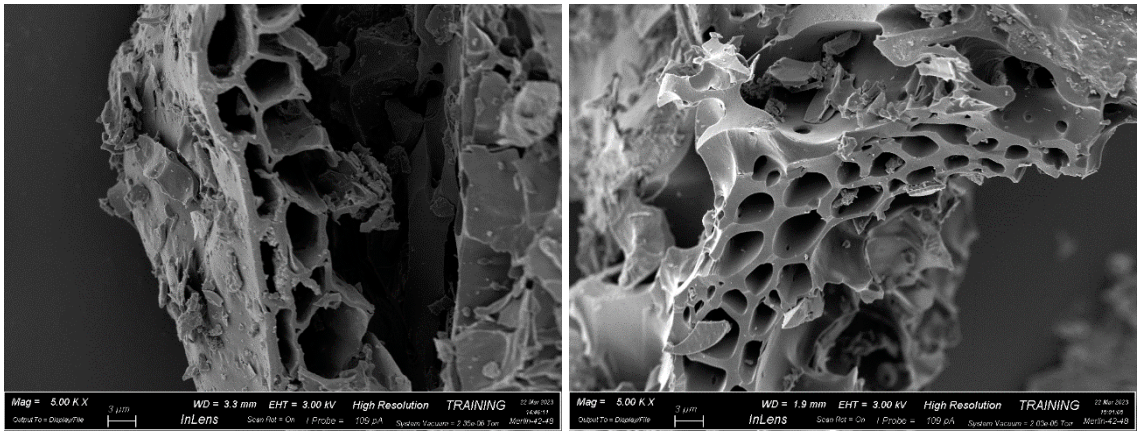

Figure 29: FESEM images of rice husk biochar CO_2 and rice husk biochar N_2

As far as hydrochar is concerned, it has fewer irregular surfaces than the biochars and the raw rice husk and it features a smaller pore size (*Figure 30*).

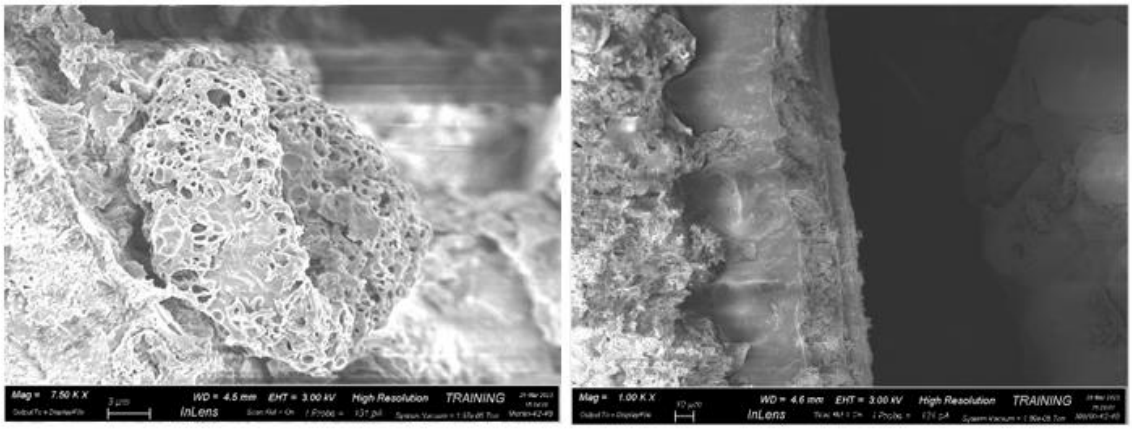

Figure 30: FESEM images of rice husk hydrochar

Finally, activated carbon is shown in *Figure 31*: it presents fine granular blocks with hardly visible pores.

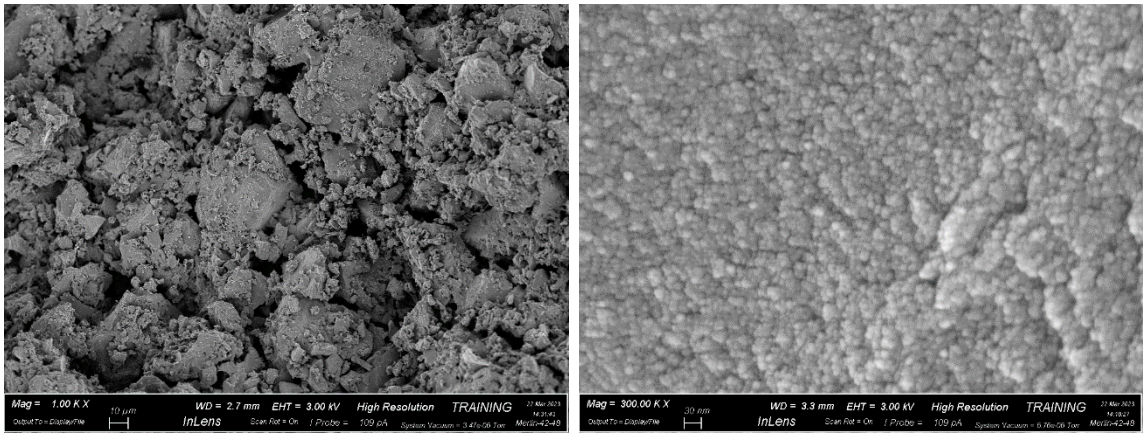

Figure 31: FESEM images of activated carbon

The BET method used for the specific surface area and pore volume determination gave information on the porosity of the adsorbents. The adsorption capacity of biochar depends significantly on its internal structure. A larger specific surface area (BET) and pore volume generally indicate stronger physical adsorption capacities. However, the pore diameter of the adsorbent also plays an important role. According to adsorption theory, when the pore diameter of the adsorbent is 1,7 - 3 times larger than the size of the adsorbate molecules, it exhibits optimal adsorption properties. Furthermore, when the pore diameter is 3 - 6 times larger or even more than the size of the adsorbate molecules, the adsorbent can be regenerated (Chen et al., 2019).

Here it is reported the obtained results for each adsorbent material that underwent the BET method for the specific surface area (SSA) determination, along with the volumes (*Table 5*):

	Rice husk biochar (CO_2)	**Rice husk biochar (N_2)**	**Rice husk hydrochar**	**Activated carbon**
BET specific surface area (m^2/g)	179,8	84,2	22,5	1459,9
Micropore Volume (cm^3/g)	0,543	0,318	0,107	0,987

Table 5: BET specific surface area

These values concerning pores and their properties are also widely studied in the literature. For this reason, it is suitable to make a comparison, which is shown in *Table 6*:

Reference	**Material**	**BET specific surface area (m^2/g)**	**Micropore Volume (cm^3/g)**
(S. Wang et al., 2005)	Activated carbon	1118 – 957 - 972	0,415 – 0,381 – 0,495
(Zhou et al., 2021)	Activated carbon	1310	0,516
(Karaca et al., 2008)	Activated carbon	900	0,294
(Phuong et al., 2015)	Rice husk biochar	364,2	0,150
(Lang et al., 2021)	Rice husk biochar	256	0,069
(Nworie et al., 2019)	Rice husk biochar	27,3	-
(Y. Wang & Liu, 2017)	Rice husk biochar	119,2	-
(Phuong et al., 2015)	Rice husk biochar	216,2	0,110
(Ighalo et al., 2022)	Rice husk hydrochar	25,5	0,11
(Hagos et al., 2022)	Rice husk hydrochar	11,6	0,03
(Lang et al., 2021)	Rice husk hydrochar	17	0,07

Table 6: Literature review of BET specific surface area and micropore volume

From the literature, the results for activated carbon are approximately in agreement with those found in this study regarding the specific surface area; for the micropore volume, however, a higher value than the reference values was obtained. The range of specific surface area values for rice husk biochar is wide and includes the values found in this thesis work, while, as for activated carbon, the micropore volume values from the literature are lower. Finally, hydrochar agrees very well with the literature for both values.

Results from elemental analysis (CHNSO) showed that the percentage by weight of the original sample of the different elements are the ones listed in *Table 7*:

	C (%)	**H (%)**	**N (%)**	**S (%)**	**O (%)**
Rice husk	42,99	1,79	3,09	0,35	51,79
Rice husk biochar (CO_2)	74,09	2,09	1,68	0,12	22,02
Rice husk biochar (N_2)	72,00	2,30	1,68	0,12	23,90
Activated carbon	80,45	2,48	1,74	0,03	15,30

Table 7: Results from CHNSO analysis

The CHNSO analysis performed on biochar CO_2 and biochar N_2 shows almost exactly the same values. With respect to the raw rice husk, all the materials present a higher percentage of carbon due to the volatilization of the compounds during the thermochemical processes, that leads to a solid carbonaceous product. For this reason, the oxygen percentage is reduced and the carbon percentage increases. Activated carbon shows a very high percentage of carbon, lower content of sulphur due to the different origin of the starting material and a low percentage of oxygen.

Regarding the determination of the **Point of Zero Charge** of the different adsorbent materials, a graph of initial pH vs. final pH was constructed based on the results obtained through the procedure described in Section *5.3.7*.

In total, there were 6 pH values available for each material, and using MATLAB, the data were interpolated to obtain the corresponding curves.

The resulting graph is shown in *Figure 32*.

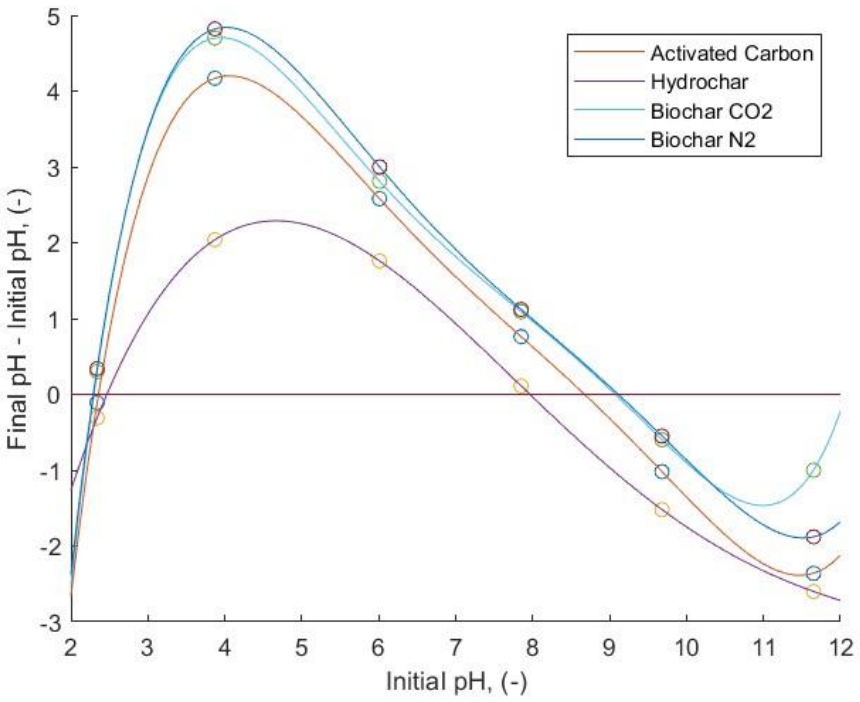

Figure 32: Determination of PZC for all the different materials

As it can be seen, the pH at Point of Zero Charge can be individuated as the points where the final pH equals the initial one and this resulted in:

- Activated carbon: pH_{PZC} = **8,67**
- Hydrochar: pH_{PZC} = **7,96**
- Biochar CO_2: pH_{PZC} = **9,07**
- Biochar N_2: pH_{PZC} = **9,11**

The material with the lowest value is the hydrochar, while biochar CO_2 and biochar N_2 have approximately the same value.

These obtained values can be compared with those found in the literature, as shown in *Table 8.*

Lower values are observed compared to those found in the present study. This could be attributed to the fact that the pH_{PZC} value strongly depends on the elemental composition of the starting rice husk and the temperature and heating program used during pyrolysis or HTC, as well as any activation of the biochar.

Table 8: Literature review of PZC

Reference	***Material***	***pH_{PZC}***
(Le et al., 2021)	Activated rice husk biochar at 600 °C	8
(Guilhen et al., 2022)	Rice husk biochar at 550 °C	7,22
(Guilhen et al., 2022)	Rice husk biochar at 770 °C	7,64
(Guilhen et al., 2022)	Rice husk biochar at 550 °C	7,24
(Guilhen et al., 2022)	Rice husk biochar at 770 °C	8,53
(Huyen T. B. et al., 2022)	Activated rice husk biochar at 600 °C	7,8

6.2 *Adsorption experiments*

The results of the conducted experiments will be presented in this section, categorizing them based on the type of material under analysis and the explored parameter, providing graphical representations of the trends. To perform a comprehensive analysis, a comparison is presented between the four different materials, evaluating their performance in different conditions.

6.2.1 Effect of adsorbent concentration

For the study on adsorbent dosage, the trend of removal efficiency at the end of the experiment with respect to the concentration of adsorbent material used was examined. The results are illustrated in *Figure 33*, where all four materials are plotted together and compared.
The results show a correlation between dye removal and the adsorbent dosage: generally, the removal efficiency is proportional to the g/L of adsorbent material used.

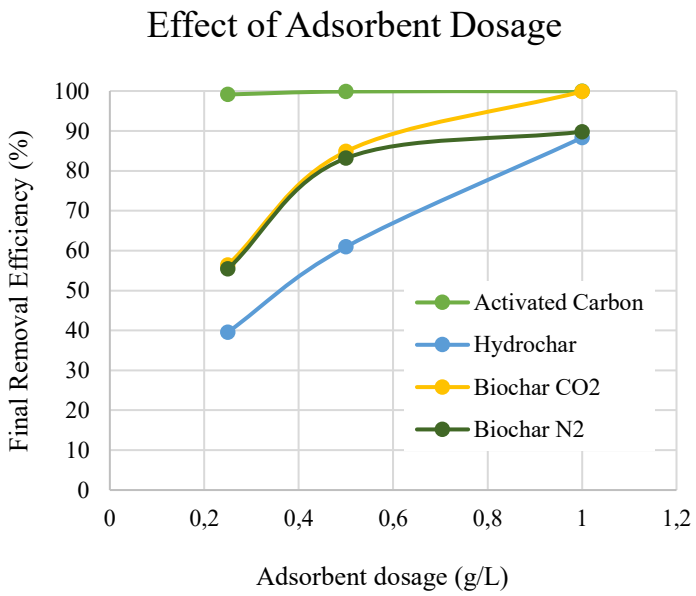

Figure 33: Effect of adsorbent dosage on removal efficiency

The removal efficiency of any adsorbent in wastewater treatment mainly depends on the number of adsorption sites that are available and active. In fact, as the amount of adsorbent material increased, the rate of MB removal showed a gradual increase because of the greater surface area and greater number of adsorption sites available on the adsorbent.

Then, adsorption tended to reach equilibrium when a specific amount of adsorbent mass was reached, as it can be seen for biochar N_2, that reached the saturated value at adsorbent dosage of about 1 g/L.
In the studied range, instead, hydrochar is still far from reaching equilibrium, biochar approaches it at 1 g/L, while activated carbon needed a lower range of values to show its tendency to equilibrium, since even at 0,25 g/L it's already at equilibrium.

This graph could be used to determine the optimal dosage amounts, i.e., the point at which a further increase in the adsorbent dosage no longer result in a significant improvement in removal efficiency, indicating the achievement of equilibrium.
For activated carbon, a detailed study is needed, conducting tests at lower dosages to find the point where the curve's slope changes. However, since it is not the focus of this study, it was decided to not perform new experiments. Regarding the other materials, for biochar N_2 1 g/L can be considered as the optimal dosage since it has already reached the asymptote. For biochar CO_2, it can be observed that at 1 g/L, there is already a value close to 100% removal efficiency, so it can also be considered as the optimal dosage. For the hydrochar, on the other hand, a study at higher concentrations would be required.

Another observation that can be made concerns the trend of the adsorption capacity (*Figure 34)*: as the dosage increased, the ability of the adsorbents to adsorb MB decreased. In fact, at higher dosages of adsorbents, there were insufficient MB dye molecules in the solution to fully interact with all the available adsorption sites on the adsorbent, while the adsorbent mass at the denominator of the definition of q_e increased. This led to a state of surface equilibrium and a decrease in the adsorption capacity per unit mass of adsorbent (Kuang et al., 2020).

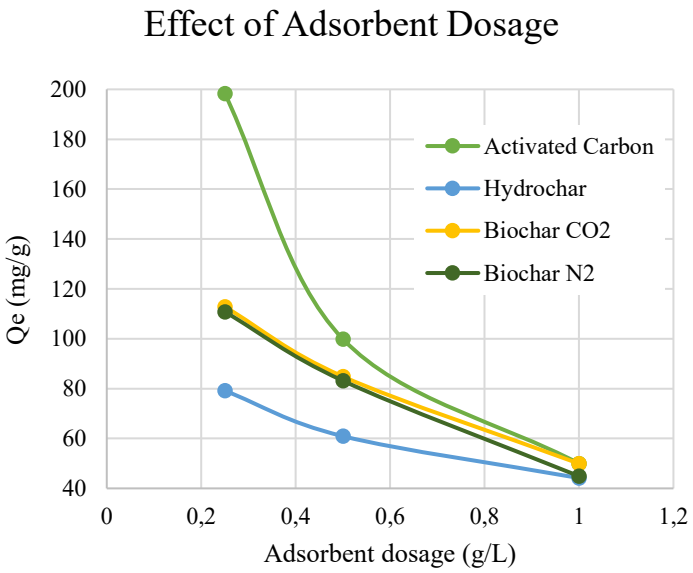

Figure 34: Effect of adsorbent dosage on adsorption capacity

6.2.2 Effect of contact time

The contact time has a great influence on dye adsorption and decreasing the time required to have an effective dye removal is necessary in wastewater treatment.

The first material analysed was **activated carbon**, as it is widely used and commonly employed. It has been extensively studied in the literature and was included in this study to comparing it with the innovative materials proposed, in order to determine if they exhibit performance that can overall be considered competitive.

During the experiments, the initial dye concentration was maintained at 50 mg/L, while the concentration of activated carbon assumed three different values (0,25, 0,5, and 1 g/L), as previously mentioned.

The MB concentration was measured and recorded during the six hours of experiment. Based on these measurements, a concentration vs. time graph was plotted, with the concentration of dye normalized to 1 on the y-axis. This was done to make the comparison between the different cases easier and to make the data dimensionless.

The obtained result is presented in *Figure 35*, where all three curves, including error bars based on three experiment duplicates, can be observed simultaneously:

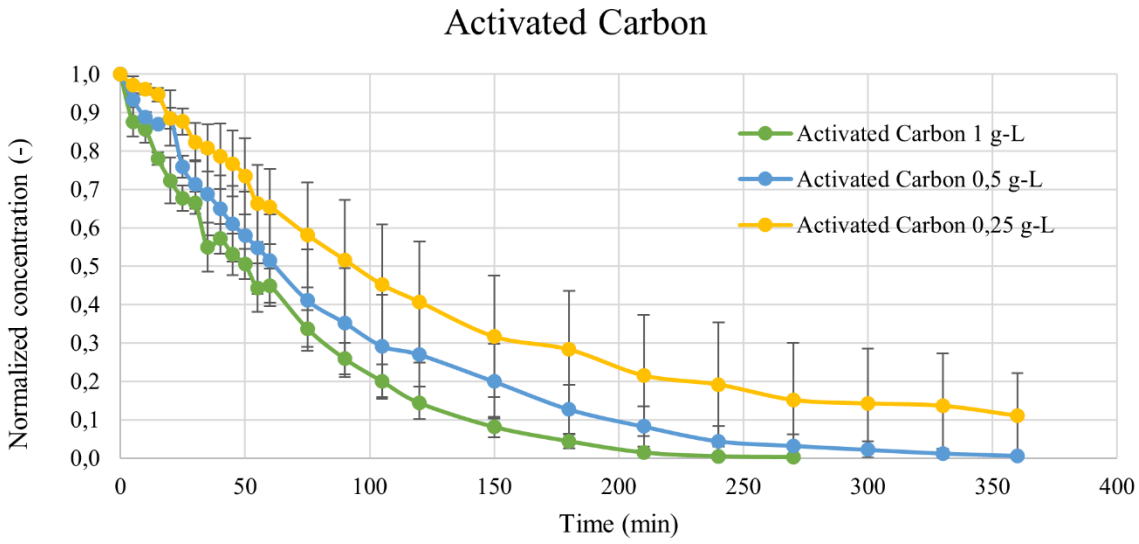

Figure 35: Trend of normalized concentration with respect to time for activated carbon

In all three cases, a very rapid decrease in concentration can be observed, with the achievement of an almost complete removal by the 1 g/L and 0,5 g/L cases. However, the third case does not allow reaching a concentration close to zero, indicating the need to use a higher adsorbent concentration to achieve the objective or to extend the experiment for a longer period.

The same information can be visualized using the calculation of the removal efficiency and adsorption capacity:

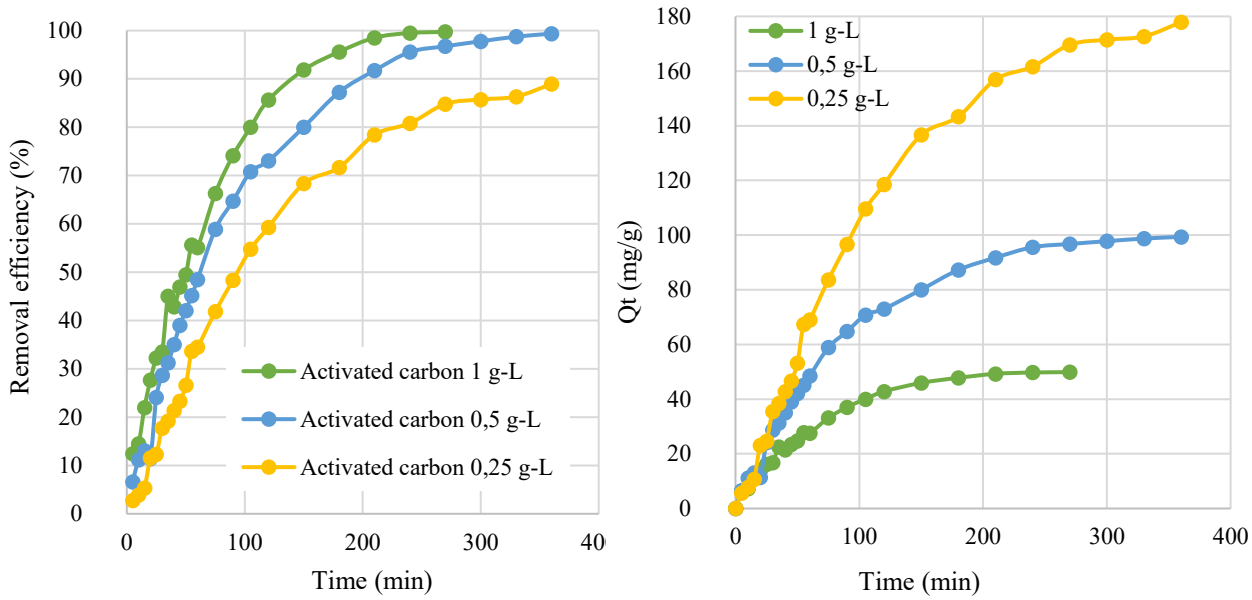

Figure 36: Removal efficiency and adsorption capacity vs time for activated carbon

The changes in MB adsorption over time, as shown in *Figure 36*, reveal that the adsorption rate and dye uptake increase with contact time until reaching equilibrium. There is a rapid rise in the initial stages of MB adsorption, followed by a decrease as it approaches equilibrium. This suggests that during the early phase of adsorption, a sufficient number of active sites are available and gradually become occupied over time, limiting further adsorption (Nworie et al., 2019).

In fact, the changes in the adsorption rate are primarily due to variations in the concentration gradient. Initially, the rapid adsorption is facilitated by the high concentration gradient, which acts as a driving force, and this is due the increased number of active sites available. However, as time proceed, the concentration gradient decreases because the MB molecules accumulate on the adsorption sites, and the rate of adsorption slows down until it reaches equilibrium, where the MB molecules that desorb from the adsorbent are in dynamic balance with the ones that re-adsorb onto it. This explains why, after a certain time period, the adsorption percentage remains nearly constant (Sharma et al., 2010), (Vadivelan & Vasanth Kumar, 2005).

In the adsorption capacity plot, the curve referred to 0,25 g/L dosage is the higher one and this is due the same motivations as the previous paragraph regarding the effect of the adsorbent dosage on q_e.

As shown in *Figure 37*, the other analysed materials (biochar CO_2, biochar N_2, hydrochar) have a similar trend, even if they don't achieve complete removal of Methylene Blue:

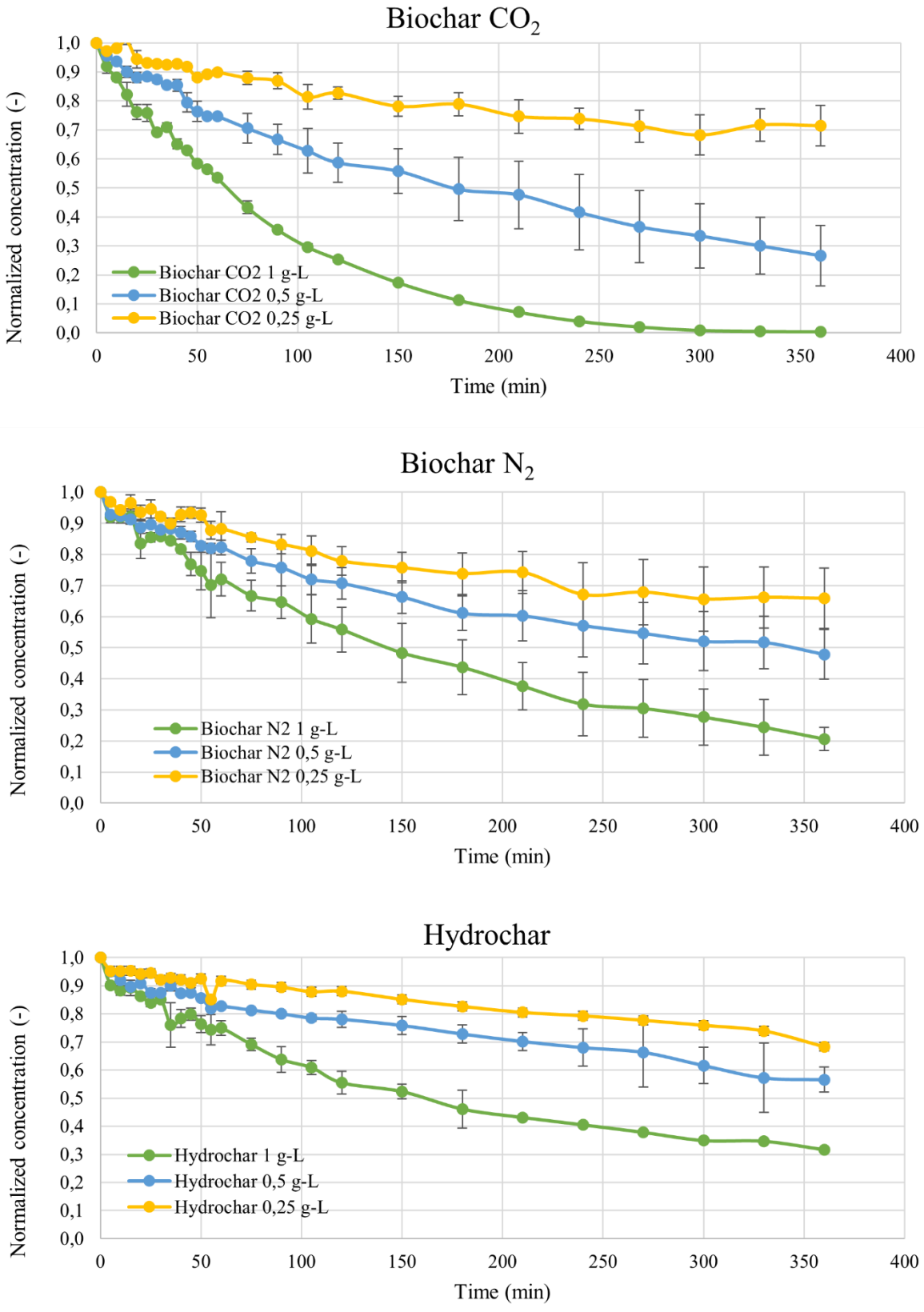

Figure 37: concentration of MB vs time for biochar CO_2, biochar N_2 and hydrochar

The following figures (*Figure 38*) display the removal efficiencies and adsorption capacity for the three innovative materials:

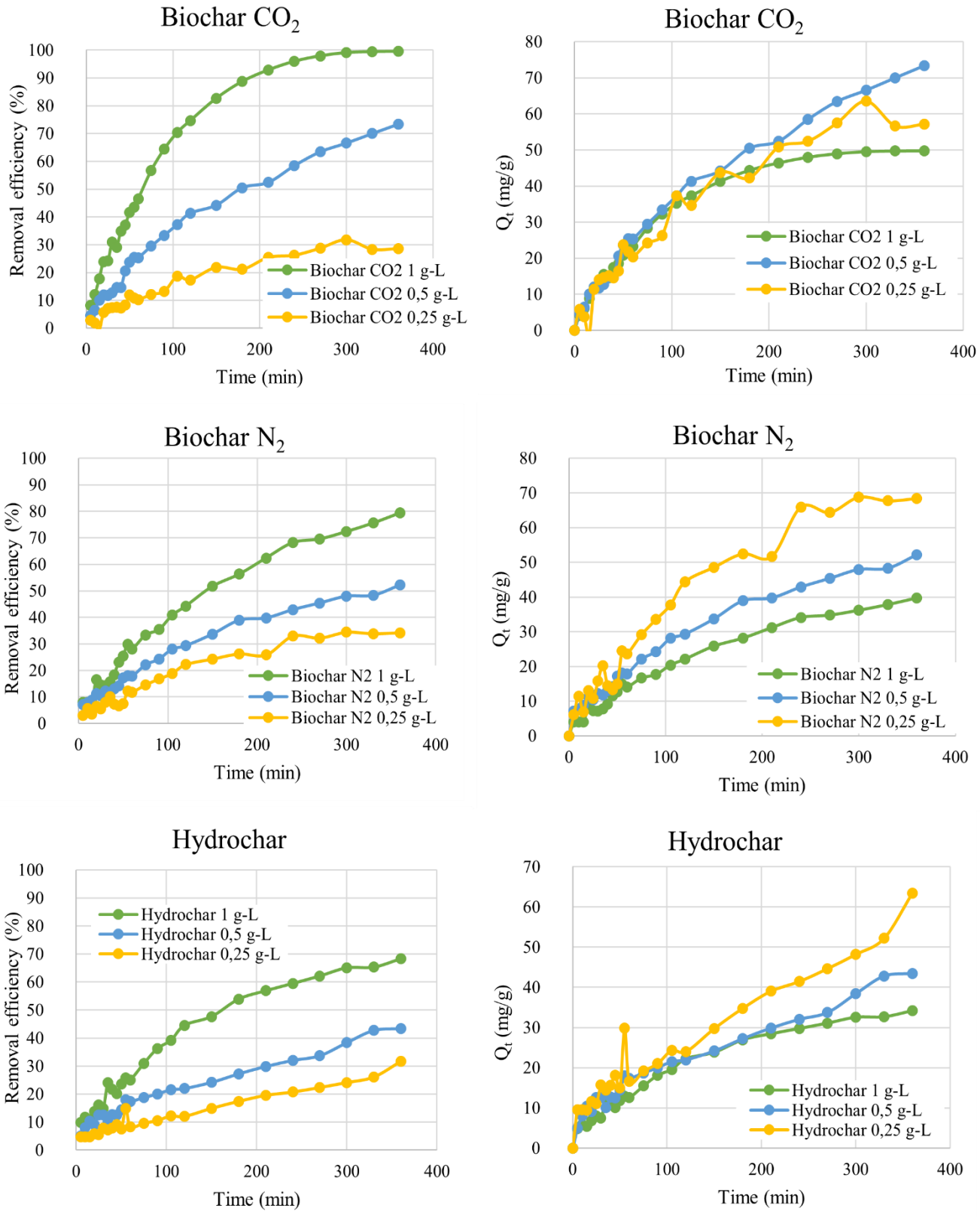

Figure 38: Removal efficiencies and adsorption capacity over time for biochar CO_2, biochar N_2 and hydrochar

The only case in which a removal efficiency of 100% is reached in times comparable to those of activated carbon is the case of biochar CO_2 at 1 g/L. In the other cases, the six hours were not sufficient to reach 100% removal or even a condition of equilibrium. The trend of the graphs reflects what was mentioned for activated carbon: an initial steeper slope that then evolves towards a horizontal asymptote, even though more slowly compared to the reference case of activated carbon.

6.2.3 Effect of pH

Figure 39 illustrates the variation in removal efficiency and adsorption capacity for hydrochar and biochar CO_2 as a function of solution pH. The data points used to create these graphs were selected from experimental values obtained at 6 hours from the start of the experiment. The curve for biochar N_2 is represented with dashed lines because, unlike the other two materials studied, it was constructed based on only two data points, assuming a linear trend that, instead, would be similar to that of biochar CO_2 if more intermediate data were available.

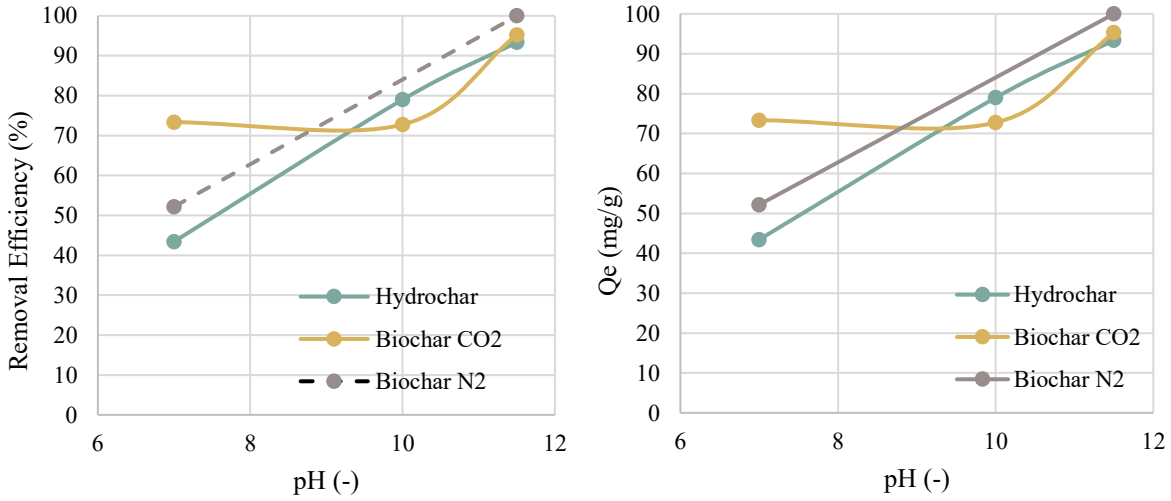

Figure 39: Effect of pH on removal efficiency and adsorption capacity

The use of a higher pH promotes adsorption, as both the adsorption removal rate and adsorption capacity increase with increasing pH value.
In particular, this effect becomes evident when the solution pH exceeds the pH_{PZC} as observed for biochar CO_2: at natural pH and pH = 10, there are no significant variations in removal efficiency, but once the pH exceeds the pH_{PZC} value of 9,07, there is a rapid increase. In reality, this effect should already be visible at pH = 10, considering the pH_{PZC} value of this material. However, this discrepancy could be due to inaccuracies when calculating the pH_{PZC}, which might be higher than 9,07, or inaccuracies in pH measurement during the experiments at altered pH levels, potentially overestimating the solution pH, that instead of 10 was maybe even lower than the pH_{PZC}.

It can be presumed that the same happens for biochar N_2, despite the lack of the intermediate point at pH = 10.

In the case of hydrochar, which has a lower pH_{PZC} of 7,96, it is not possible to visualize the region of constant efficiency as only one measurement was taken at pH < pH_{PZC}. Therefore, there is insufficient information regarding the region to the left of the pH_{PZC}. However, the rapid increase in efficiency in the region at pH > pH_{PZC} is clearly visible, as evidenced by the cases at pH = 10 and pH = 11,5.

Indeed, in solutions with a pH higher than the pH_{PZC}, the adsorbent's surface becomes negatively charged, leading to an increased adsorption of the positively charged MB cationic dye due to the electrostatic force of attraction. At lower pH levels, the surface charge becomes positively charged, allowing H+ ions to effectively compete with dye cations. This competition leads to a reduction in the quantity of dye adsorbed (mg/g) and removal efficiency.

Furthermore, the entire MB removal experiment at adjusted pH levels can be visualized using the concentration normalized vs. time graphs *(Figure 40)*.

In the graph for biochar CO_2 *(Figure 40a)*, there is no noticeable improvement between the natural pH case and the pH = 10 case, as the pH_{PZC} may not have been exceeded, possibly for the reasons previously suggested. However, the case at pH = 11,5 is definitely beyond the pH_{PZC}, as indicated by the significantly lower curve.

For hydrochar (*Figure 40b*), both the pH = 10 and pH = 11,5 cases show better performance compared to pH = 7. Between these two, it's noticeable that they have almost the same trend most of the time, although the pH = 11,5 curve consistently stays slightly lower, with a significant difference during the last hour of the experiment.

Finally, for biochar N_2 (*Figure 40c*), the beneficial effect of raising the pH is clearly visible, as complete removal is reached already at 200 minutes.

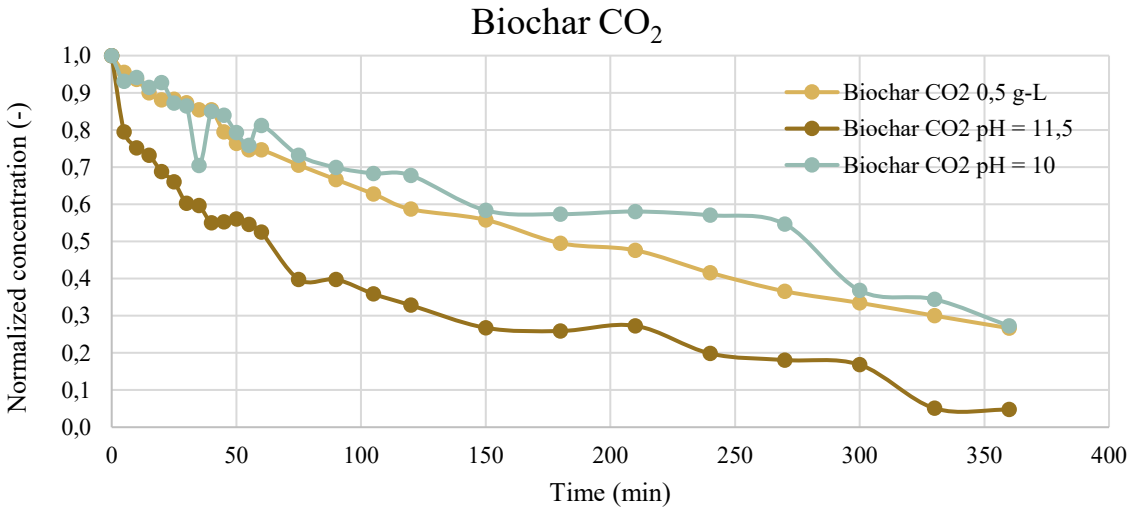

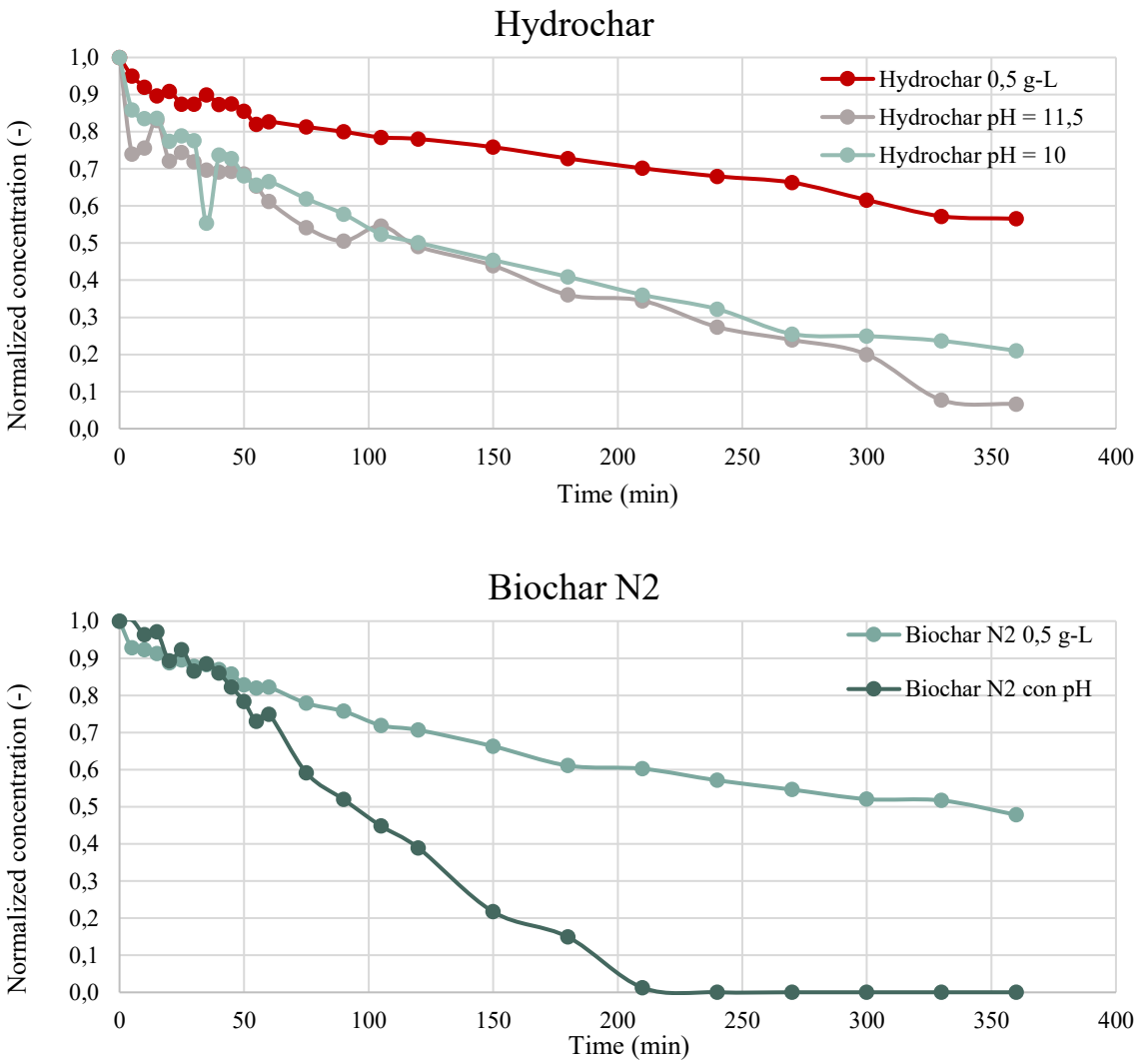

Figure 40: Trend of normalized concentration over time considering the effect of pH

6.3 Modelling

Regarding the modelling based on the experimental data obtained, a kinetic and thermodynamic analysis was conducted, accompanied by a data cleaning step and model validation.

6.3.1 Outliers detection

Before testing the kinetic and thermodynamic models on the results obtained from the conducted experiments, the normal distribution of residuals was verified through the construction of a normal probability plot. Indeed, this serves primarily to identify potential outliers, i.e. cases where residuals are significantly larger than others, strongly deviating from the linear trend.
The presence of one or more outliers can severely distort the analysis of variance and the interpretation of residuals (*Figure 41*). Therefore, in cases like this, an accurate outlier analysis is necessary to understand whether it represents a particularly significant anomalous value, indicating a deviation from the regular data pattern, or, on the contrary, a data point to be discarded due to calculation and/or experimental errors.

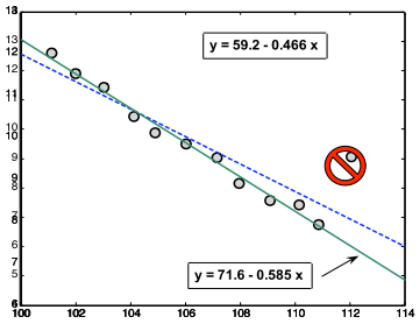

Figure 41: Influence of the presence of an outlier on residuals interpretation (Pier Luca Maffettone, 2009)

The outliers, moreover, also influence the randomness plot: normally, to be considered valid, this type of graph should represent the data in a horizontal band centered on the x-axis with a random distribution, without any identifiable structure as it will be shown in section *6.3.3*, but the problem is that an outlier can alter the perception of the horizontal band in the randomness plot. Its presence may influence the scale on the vertical axis, resulting in a flat graph that seems to have a recognizable tendency (*Figure 42*).

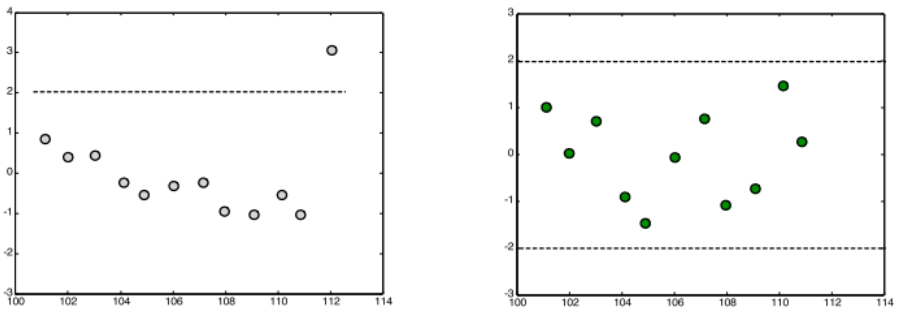

Figure 42: Influence of an outlier on randomness plot (Pier Luca Maffettone, 2009)

Therefore, to classify an experimental point as an outlier, one can conduct either a purely visual analysis by identifying points that deviate the most from the normality plot line, or a numerical analysis based on standardized residuals.

The **standardized residual** has been calculated according to the following formula (*eq. 24*):

$$d_i = \frac{e_i}{\sqrt{MSE}} \qquad (eq.\ 24)$$

Where e_i is the residual and MSE represents the Mean Squared Error (*eq. 25*), linked to SSE through this relationship:

$$MSE = \frac{SSE}{n-p} \qquad (eq.\ 25)$$

The term *n* indicates the total number of data points collected for each experiment, while *p* indicates the number of model parameters, which in this case is always equal to 2. The division by *n-p* takes into account that *p* degrees of freedom are already used to estimate the model parameters, thus reducing the effective number of degrees of freedom available to measure data variability. In the context of nonlinear regression, this makes MSE a statistically more appropriate parameter than the more common MSE defined without considering the subtraction of *p*.

The standardized residuals should approximately follow a normal distribution with a mean of zero and a unit variance. At least 95% of them should fall within an interval of +/- 2 times the standard deviation. In the context of this thesis, a standardized residual not falling approximately within the [-2, 2] range was considered an outlier (Montgomery, 2013).

An example of outlier detection is provided for activated carbon at 0,5 g/L in *Figure 43*:

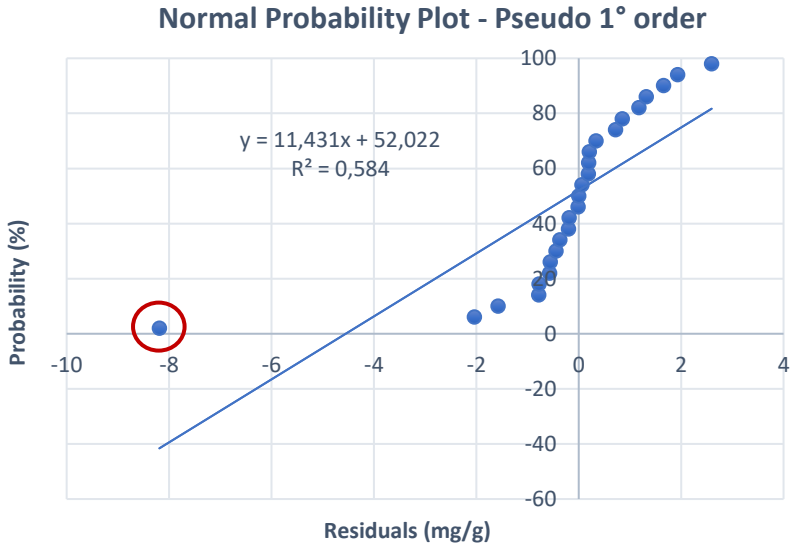

Figure 43: Normal probability plot with the effect of an outlier

In this case, the hypothesized model is the pseudo-first order, and as it can be seen, there is a point that deviates significantly from the linear trend, strongly influencing the slope of the trendline. This point has a standardized residual of approximately -4, well beyond the imposed threshold of [-2,2].

After its removal, the resulting outcome is shown in *Figure 44*:

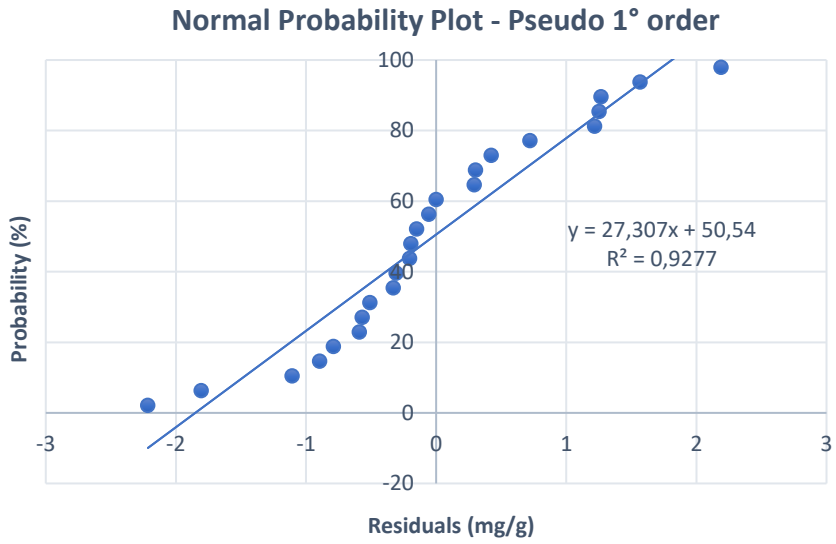

Figure 44: Normal probability plot without the influence of an outlier

Similarly, it is possible to observe the effect of the outlier on the randomness plot. In the next figures, the two plots are compared before and after the removal of the outlier point, and it can be noticed how the points, which in the first plot (*Figure 45*) appeared to have a sinusoidal trend, reveal their random nature in the second plot (*Figure 46*), without a clear pattern.

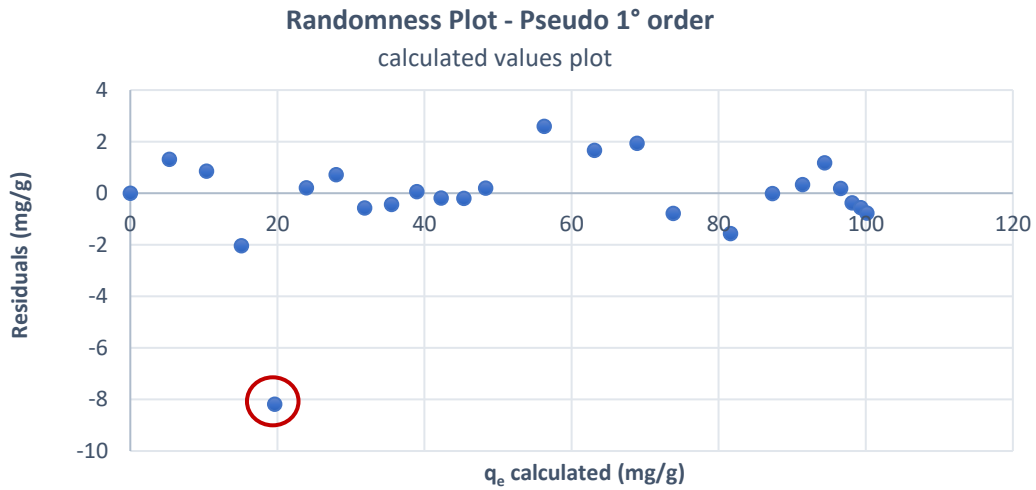

Figure 45: Randomness plot with the effect of an outlier

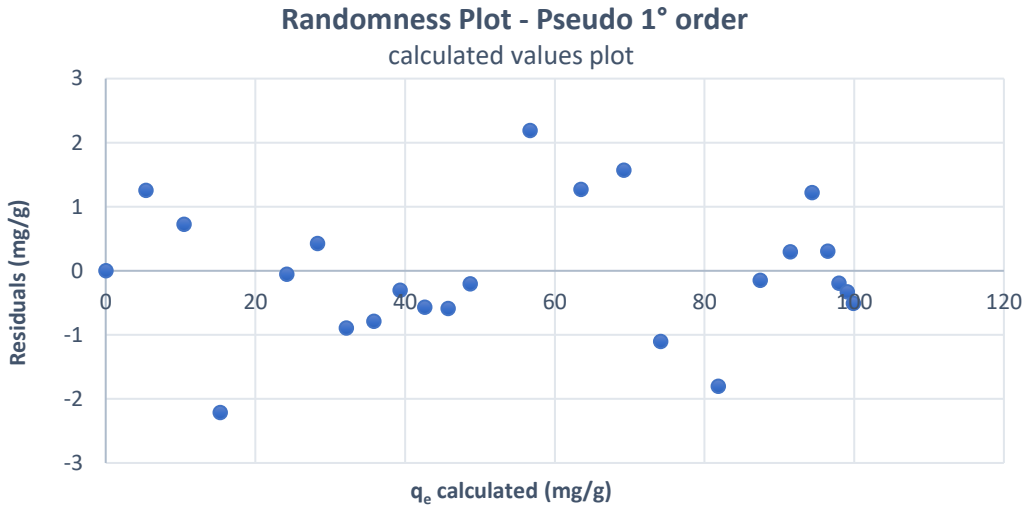

Figure 46: Randomness plot without the influence of an outlier

The same procedure was adopted for each experimental test.

The normal probability plot and randomness plot will be presented completely in section *6.3.3* on model validation, with explanatory comments to assess the normality of the residual distribution, their randomness, and so the validity of the tested models.

6.3.2 Kinetics

With regard to kinetics, the best fitting model was selected based on the value of the coefficient of determination R^2 and especially based on the difference between the q_e value calculated by the model and the experimental one. It must be considered that relying solely on slight variations in R^2 values may not be sufficient to distinguish the fitting performance of the models (Mahapatra et al., 2022).

For the **hydrochar** tests, both models approximate the experimental data well, as can be seen from *Table 9*, presenting high R^2 values. In particular, taking into account the R^2, the pseudo-second-order model appears to be slightly more accurate for all the analysed cases; the choice of the pseudo-second order is confirmed also by comparing the q_e values obtained from the model with the experimental ones, which result to be very similar for all three cases at different concentrations. The kinetic constants k_1 and k_2 derived from the two respective models are also reported.

C_o (g/L)	$Q_{e,exp}$ (mg/g)	Pseudo-First Order Model			Pseudo-Second Order Model		
		k_1 (1/min)	$Q_{e,calc}$ (mg/g)	R^2 (-)	k_2 (g/mg.min)	$Q_{e,calc}$ (mg/g)	R^2 (-)
1	44,2	0,0080	35,3	0,9945	0,00014	**48,6**	**0,9958**
0,5	60,9	0,0080	40,8	0,9199	0,00013	**53,8**	**0,9393**
0,25	79,1	0,0063	54,6	0,9268	0,00007	**75,7**	**0,9371**

Table 9: Models' parameters estimation and performance evaluation for hydrochar

Graphs in *Figure 47* graphically show the experimental points of q vs. t, with the approximation made by the first-order and second-order curves:

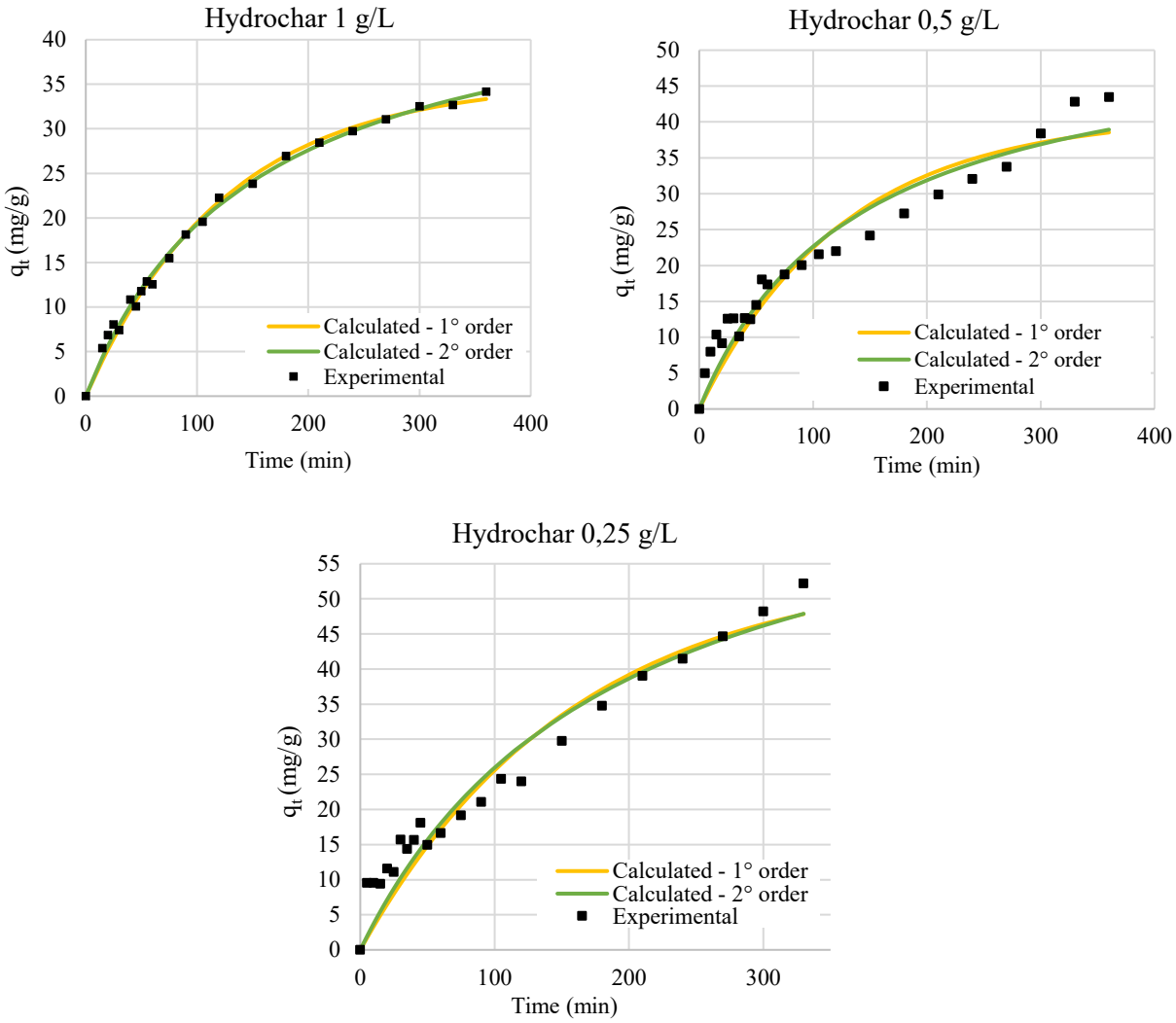

Figure 47: Model fitting of experimental data using pseudo 1° and 2° order models for hydrochar at different dosage

The graph with the higher concentration approximates the trend of the experimental points very accurately, while in the other two cases there are deviations to be further analysed, so that it may **be necessary to use a different model that can approximate the kinetics even more accurately**.

For **biochar CO_2**, *Table 10* shows a better agreement between q_e values when using a pseudo-first-order kinetic model, except for the case with lower adsorbent material concentration. In this case, in fact, a q_e value (92 mg/g) closer to the experimental one (112,8 mg/g) is obtained using a pseudo-second-order model, but it is still not a good approximation, as it shows a difference of over than 20 mg/g. The R^2 values are all very high and reflect what was observed by the above-mentioned q_e analysis except for the case at 0,5 g/L. In fact, despite having a better determination coefficient, the pseudo-second order model fails to correctly predict the q_e value.

C_o (g/L)	$Q_{e,exp}$ (mg/g)	Pseudo-First Order Model			Pseudo-Second Order Model		
		k_1 (1/min)	$Q_{e,calc}$ (mg/g)	R^2 (-)	k_2 (g/mg.min)	$Q_{e,calc}$ (mg/g)	R^2 (-)
1	49,9	0,0105	**51,7**	**0,9976***	0,00014	67,8	0,9933*
0,5	84,8	0,0061	**79,5**	0,9930	0,00004	115,0	**0,9952**
0,25	112,8	0,0070	65,1	0,9782	0,00006	**92,0**	**0,9785**

Table 10: Models' parameters estimation and performance evaluation for biochar CO_2 (*indicates that R^2 adj. was used due to different number of exp. data between 1° and 2° order)

The curves representing the fitting of the experimental data according to the two models used are depicted in *Figure 48*:

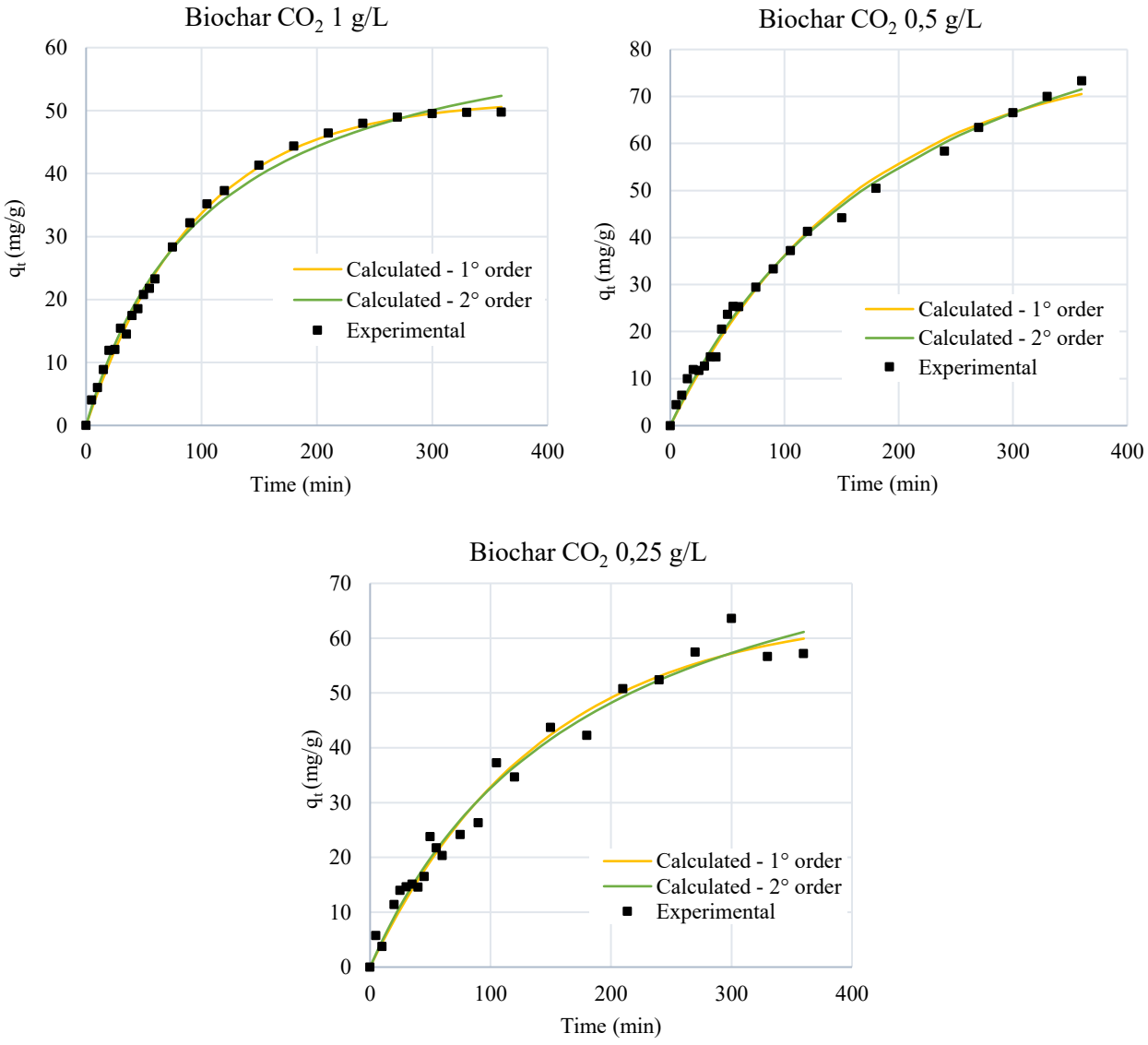

Figure 48: Model fitting of experimental data using pseudo 1° and 2° order models for biochar CO_2 at different dosage

For the values of biochar CO_2 concentration at 1 and 0,5 g/L, the curves have a good trend, whereas the case at 0,25 g/L shows some discrepancies, which could be the cause of the deviation of the calculated q_e values from the actual value found in the experiments.

As far as **biochar N_2** is concerned (*Table 11*), according to the q_e values, the pseudo-first-order model fits the experimental data well for the 1 g/L case, while in the remaining two cases, it's the pseudo-second-order model that clearly prevails. The kinetics, therefore, appear to be second-order at low concentrations and first-order at higher concentrations.

C_0 (g/L)	$Q_{e,exp}$ (mg/g)	Pseudo-First Order Model			Pseudo-Second Order Model		
		k_1 (1/min)	$Q_{e,calc}$ (mg/g)	R^2 (-)	k_2 (g/mg.min)	$Q_{e,calc}$ (mg/g)	R^2 (-)
1	44,9	0,0063	**42,9**	0,9950	0,00008	61,9	**0,9963**
0,5	83,2	0,0069	54,3	0,9925	0,00007	**76,8**	**0,9952**
0,25	110,8	0,0062	78,8	**0,9789**	0,00004	**115,1**	0,9779

Table 11: Models' parameters estimation and performance evaluation for biochar N_2

The same information is visually summarised in the graphs in *Figure 49*:

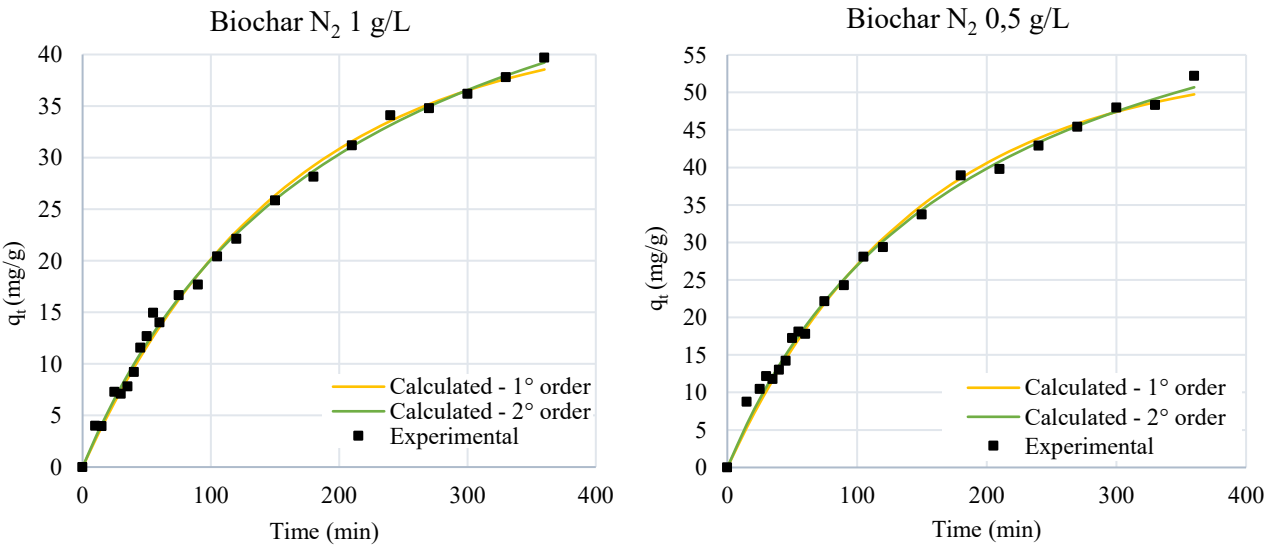

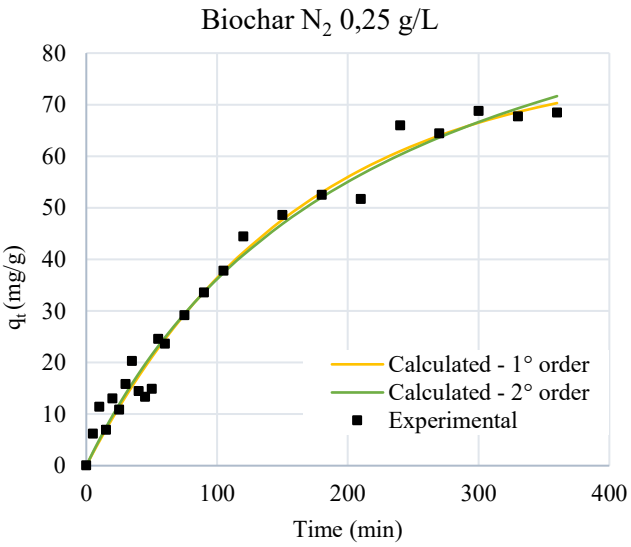

Figure 49: Model fitting of experimental data using pseudo 1° and 2° order models for biochar N_2 at different dosage

Finally, *Table 12* shows the results obtained for **activated carbon**:

C_0 (g/L)	$Q_{e,exp}$ (mg/g)	Pseudo-First Order Model			Pseudo-Second Order Model		
		k_1 (1/min)	$Q_{e,calc}$ (mg/g)	R^2 (-)	k_2 (g/mg.min)	$Q_{e,calc}$ (mg/g)	R^2 (-)
1	50,0	0,0136	**52,3**	**0,9982***	0,00017	69,5	0,9956*
0,5	99,9	0,0108	**101,9**	**0,9990**	0,00007	133,4	0,9955
0,25	198,3	0,0072	**195,9**	**0,9940**	0,00002	281,9	0,9896

Table 12: Models' parameters estimation and performance evaluation for activated carbon (*indicates that R^2 adj. was used due to different number of exp. data between 1° and 2° order*)*

In this case, the experimental data are best approximated by the pseudo-first-order kinetic model for each initial concentration value C_0. From the point of view of the coefficients of determination R^2, the most satisfactory fitting is also to be attributed to the aforementioned model.

The R^2 values for the case at $C_0 = 1$ g/L are represented with an * because they are actually Adjusted R^2 values, due to the different number of points used for pseudo-first-order modelling compared to pseudo-second-order modelling; this was because outlier detection identified some points as outliers for only one of the two models, so they have not been removed for both.

The graphs shown in *Figure 50* denote a very accurate fitting, with no oscillations or points to be further investigated, so it can be deduced that the pseudo-first-order model is the correct model to represent adsorption of MB onto activated carbon.

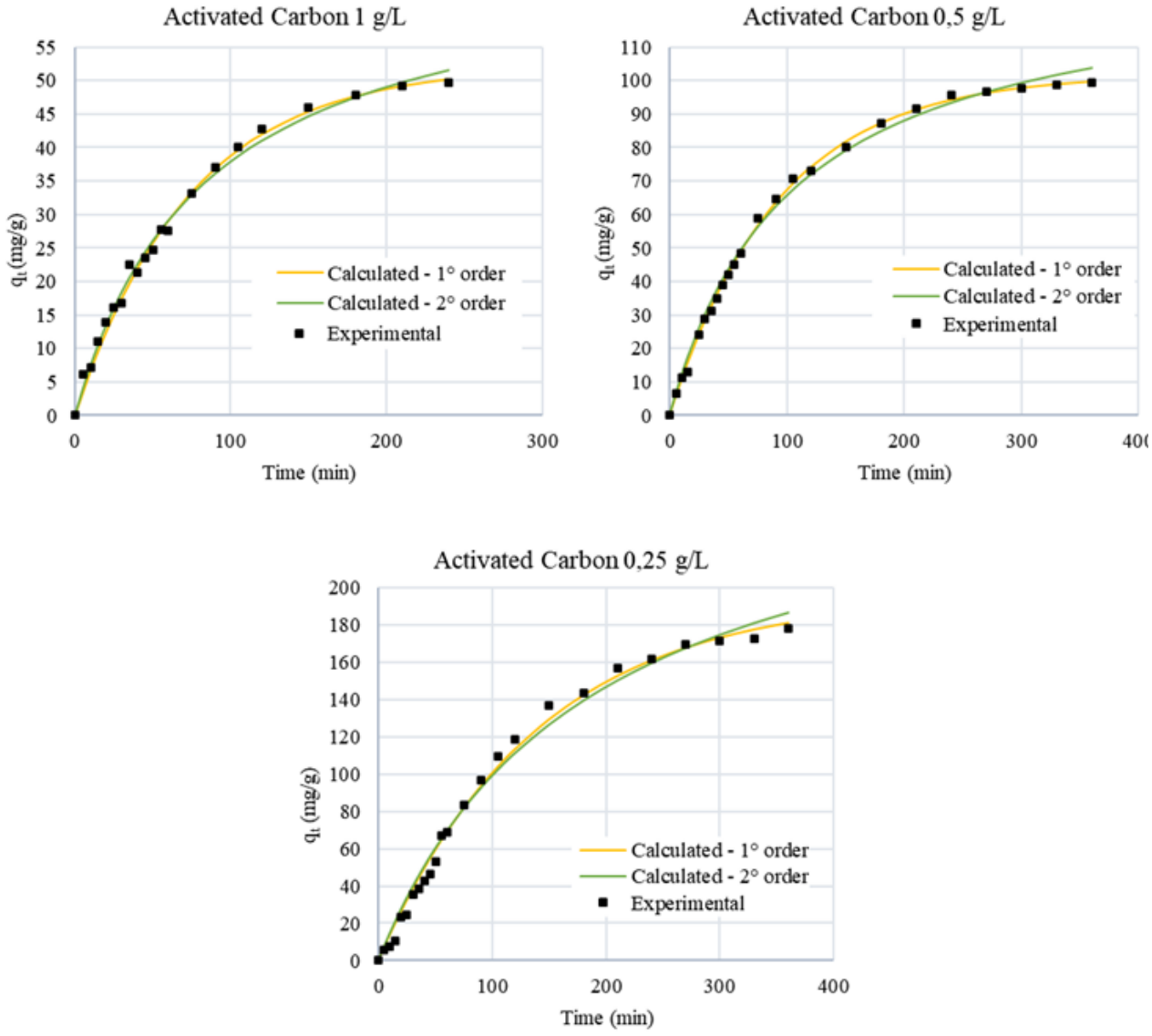

Figure 50: Model fitting of experimental data using pseudo 1° and 2° order models for activated carbon at different dosage

6.3.3 Model validation

After finding the non-linear models that best fit the data obtained from the adsorption experiment, a model validation step was conducted to verify the assumptions on which the modelling is based. In particular, the tests highlighted in section *5.5.2* are the normality test and the randomness test. In addition, the R^2 value was calculated to assess the goodness of fit.

The R^2 values are all to be considered satisfactory, as they have a value well above 0,8. However, R2 only gives information on the quality of the fit of a model, i.e. how well the non-linear regression line approximates the experimental data, but does not provide information on whether the independent variables considered are actually the true cause of the variation in the dependent variable or whether the model is correct (Revellame et al., 2020).

With regard to the initial assumptions of randomness and normality of the residuals on which the modelling is based, the randomness test is used to verify the purely random nature of the observation: if one obtains a residual vs. q_e graph in which it is possible to infer the presence of a structure in the residuals as the prediction of the independent variable q_e varies, it means that a deterministic part falls in the residual that the model has not been able to capture completely and it is therefore necessary to extend and/or modify the model. Besides randomness, it's important to confirm that the residuals of the model also follow a normal distribution. Relying solely on randomness for validation is insufficient, and normality tests are necessary to evaluate the model's appropriateness in a correct way.

However, a minor deviation from the ideal residual behaviour doesn't automatically mean that the model must be discarded. When comparing models, the one that aligns more closely with the expected residual behaviour, should be preferred (Revellame et al., 2020).

For the interpretation of normal probability plots, more attention should be paid to the central points than to the extreme points (Revellame et al., 2020).

Hydrochar 1 g/L

From the modelling of the hydrochar data, the best approximating model was the pseudo-second order (PSO) model for all cases with different concentrations. Looking at the normal probability plots *Figure 51*, the trend is satisfactory and the best linearity is obtained for the PSO.

The randomness of the residuals is guaranteed for both models, as there are no recognisable trends in the plots of *Figure 52.* The PSO model is therefore valid.

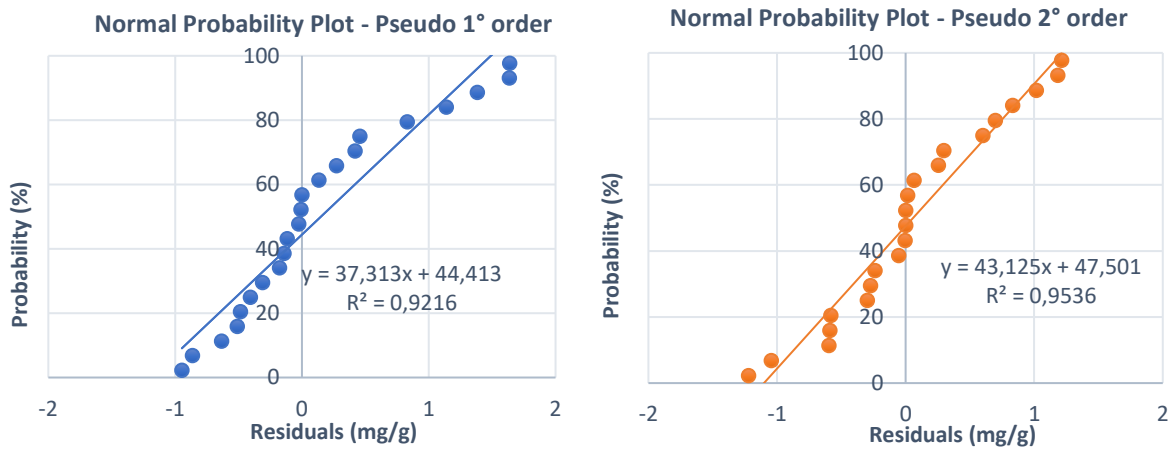

Figure 52: Normal probability plots for pseudo 1° and 2° order model – Hydrochar 1 g/L

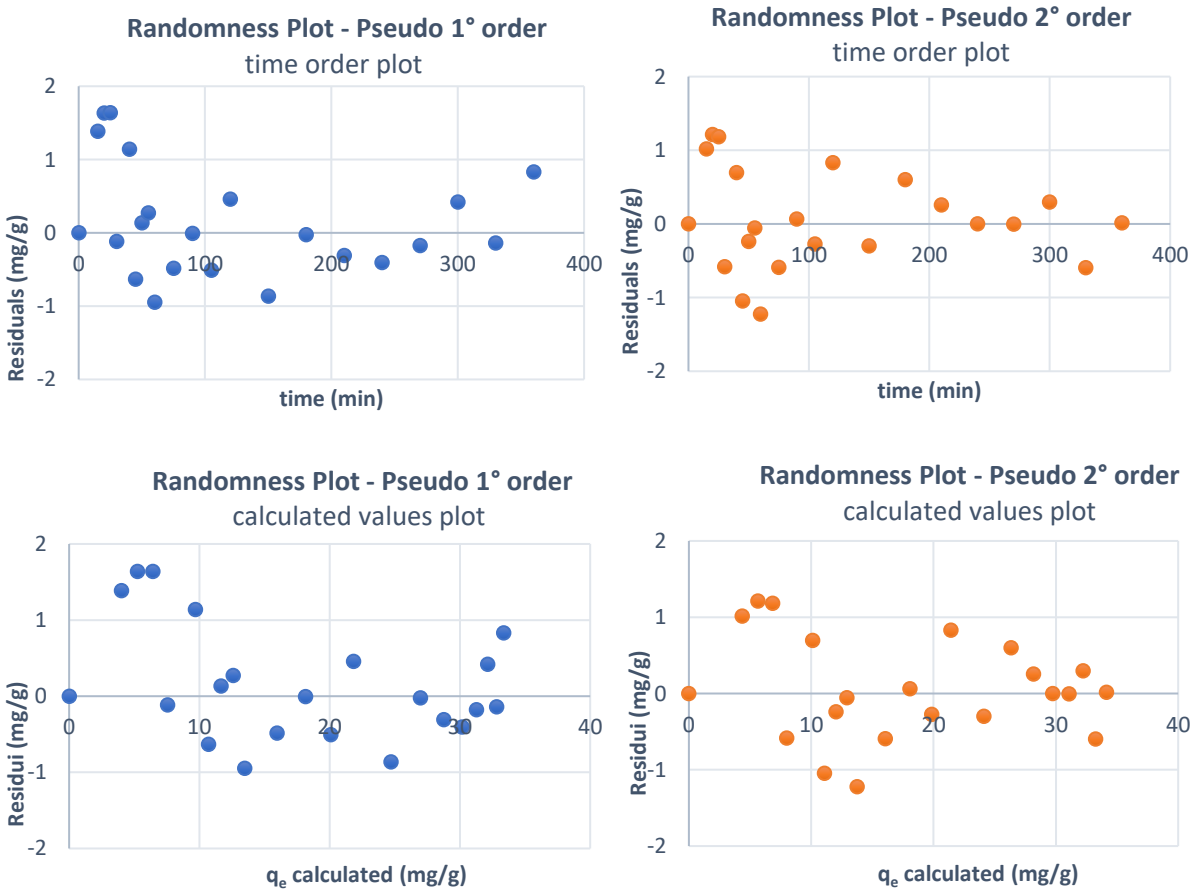

Figure 51: Randomness plots for pseudo 1° and 2° order model – Hydrochar 1 g/L

Hydrochar 0,5 g/L

Linearity is again better respected by the PSO model *Figure 53*. Regarding the randomness plots (*Figure 54*), a slight trend can be seen for only seven central points, so the randomness of the residuals can be assumed.

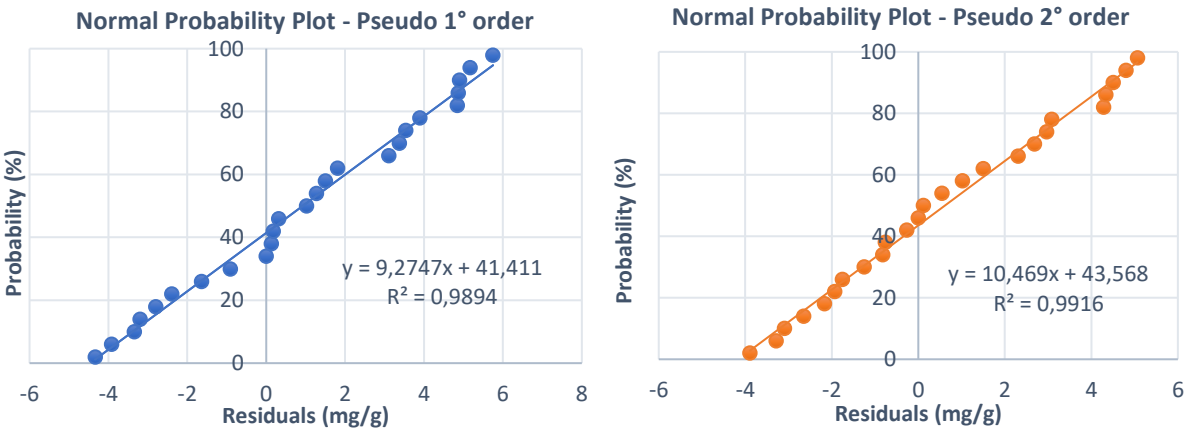

Figure 53: Normal probability plots for pseudo 1° and 2° order models – Hydrochar 0,5 g/L

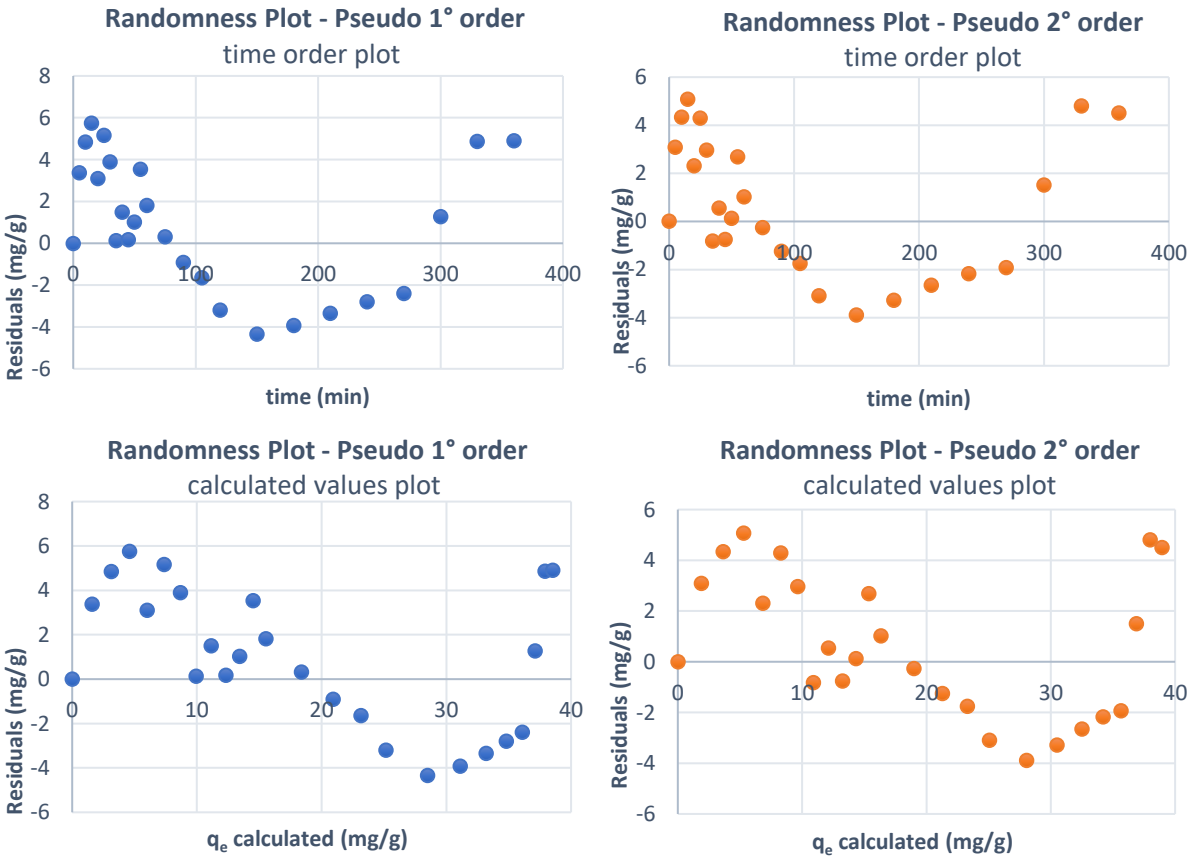

Figure 54: Randomness plots for pseudo 1° and 2° order models – Hydrochar 0,25 g/L

The points depicted in the graph on the right of *Figure 55* fall almost perfectly into a straight line, satisfying the linearity condition better than the data depicted on the graph referring to the pseudo-first order (PFO) model. The randomness hypothesis, on the other hand, is not guaranteed, as the residuals clearly show a trend with curvature (*Figure 56*), which is one of the unsatisfactory plots reported in (Draper & Smith, 1998). It may be necessary to investigate a different model or to modify the pseudo-second-order model.

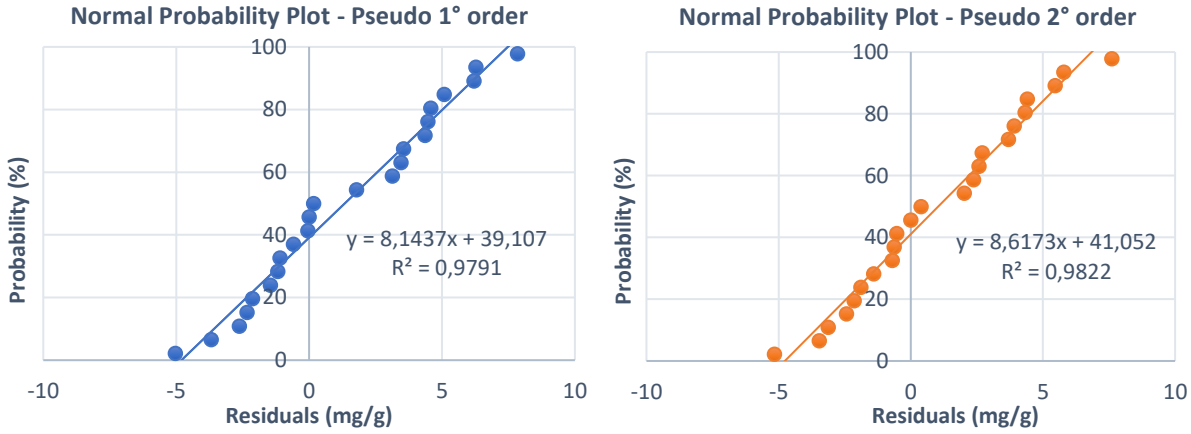

Figure 55: Normal probability plots for pseudo 1° and 2° order models – Hydrochar 0,25 g/L

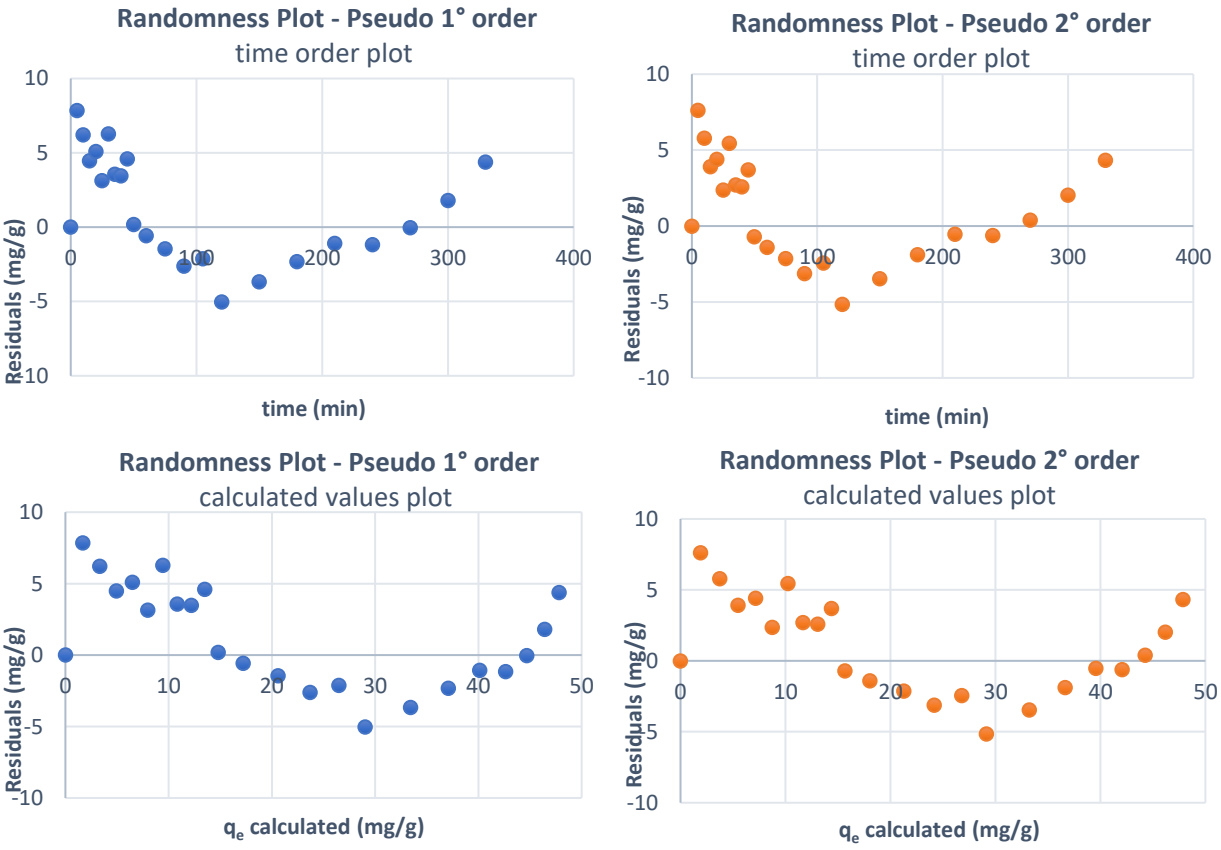

Figure 56: Randomness plots for pseudo 1° and 2° order models – Hydrochar 0,25 g/L

Biochar CO_2 1 g/L

In *Figure 57*, the normal probability plot referring to the PFO shows a better linearity (based on the R^2 value), however, the PSO is also not to be dismissed, confirming what was found through the application of the models, which agree better with the 2° order. The randomness plots *Figure 58* show a clear trend, so a new model may be needed.

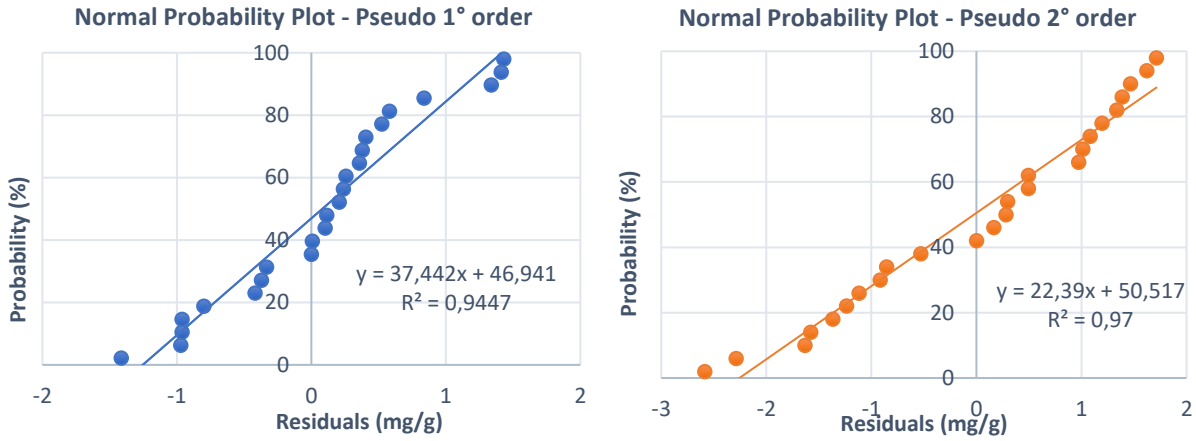

Figure 57: Normal probability plots for pseudo 1° and 2° order models – Biochar CO_2 1 g/L

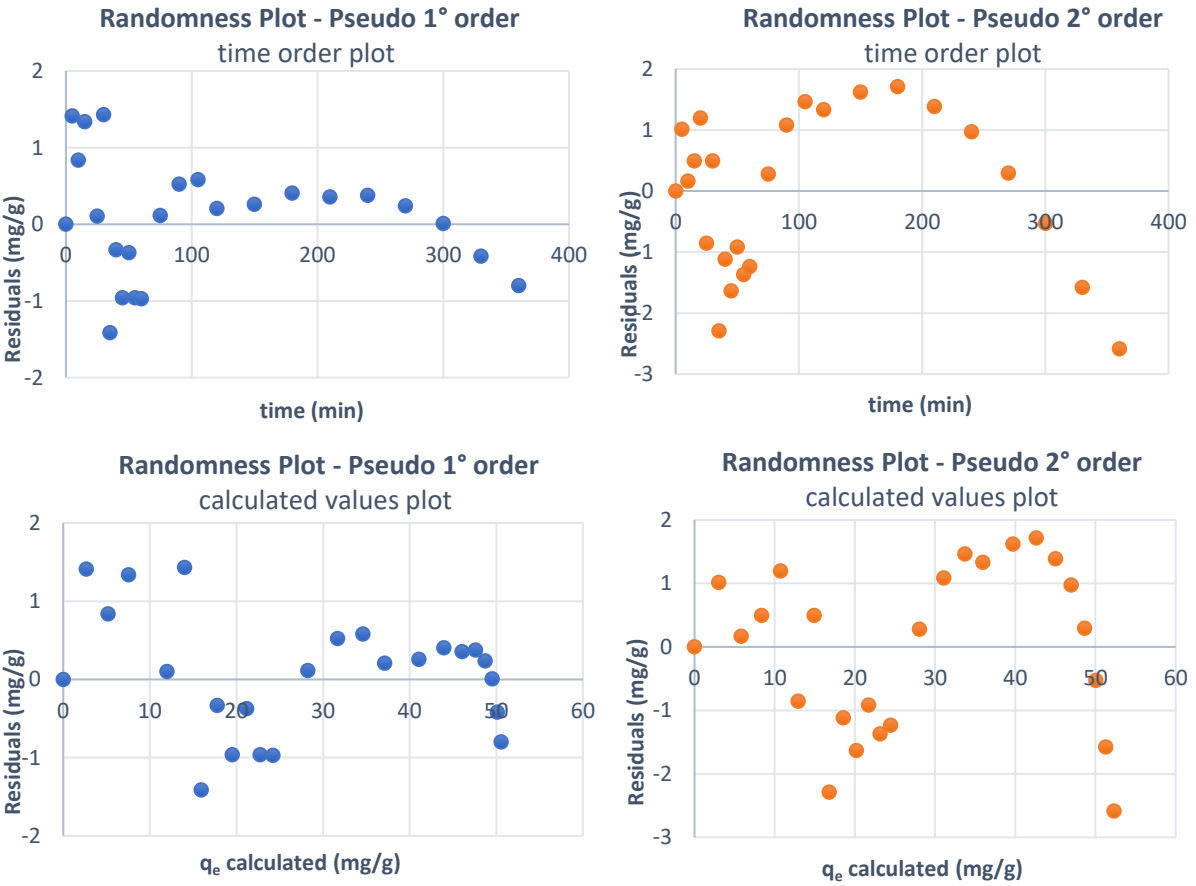

Figure 58: Randomness plots for pseudo 1° and 2° order models – Biochar CO_2 1 g/L

Biochar CO_2 0,5 g/L

PFO has a linear trend in (*Figure 59)*, in accordance with the results obtained from the comparison between the q_e values during the application of the model. Randomness plot (*Figure 60*) are satisfactory, so the PFO can be valid.

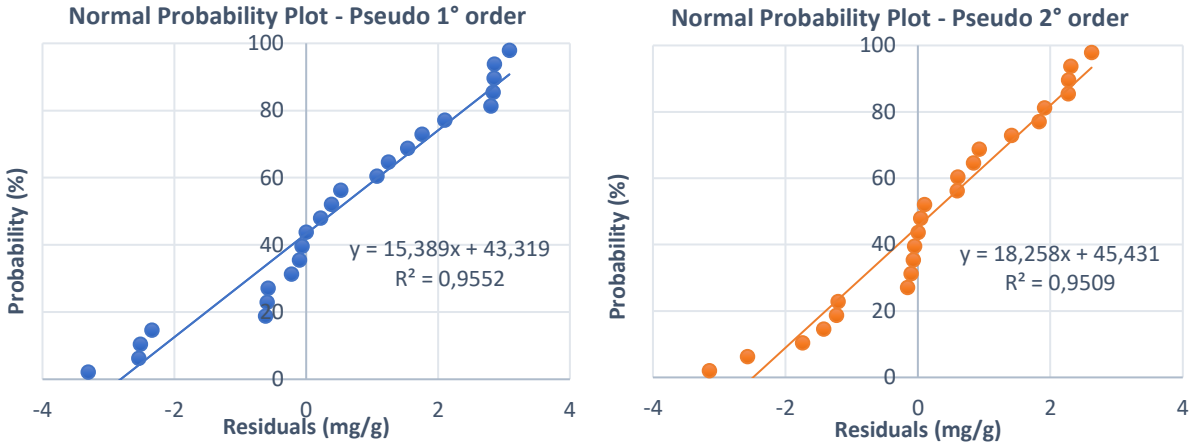

Figure 59: Normal probability plots for pseudo 1° and 2° order models – Biochar CO_2 0,5 g/L

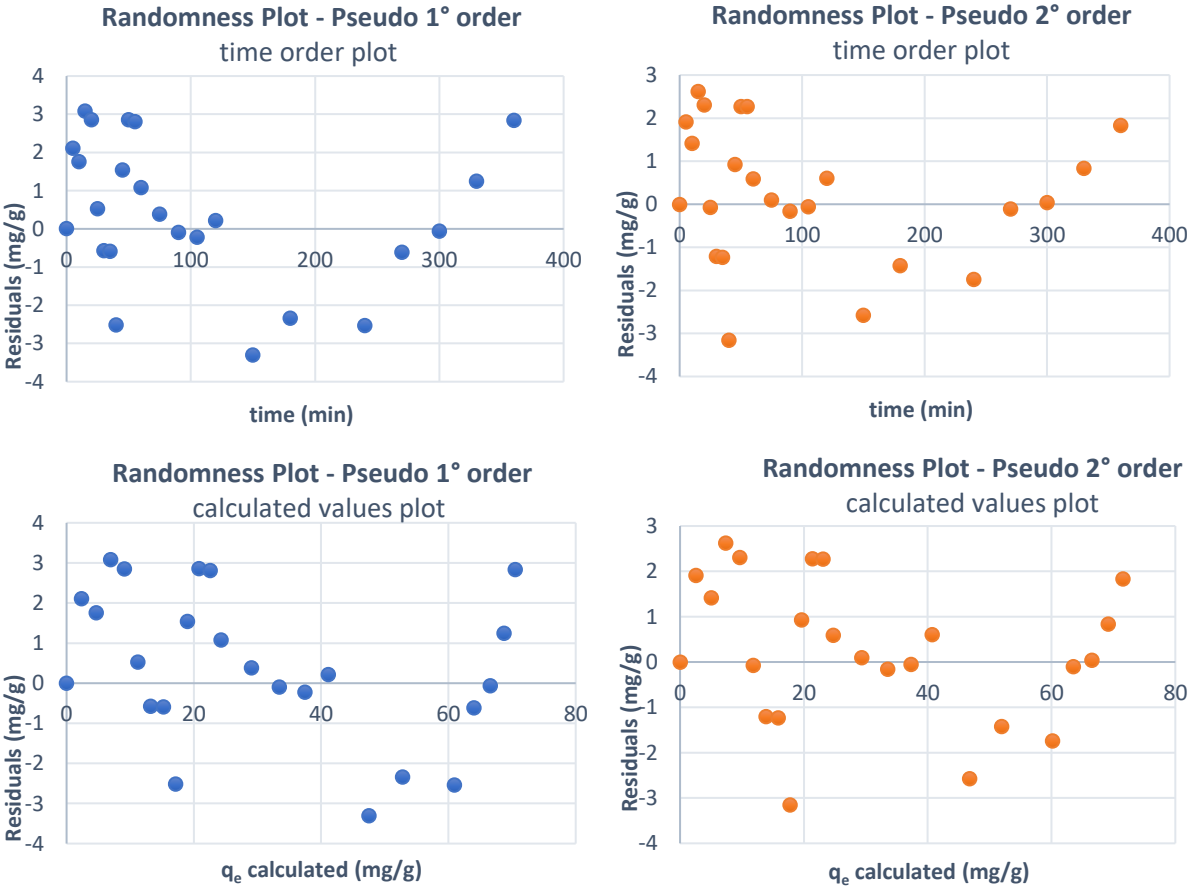

Figure 60: Randomness plots for pseudo 1° and 2° order models – Biochar CO_2 0,5 g/L

Biochar CO_2 0,25 g/L

In this case, both the normal probability plots (*Figure 61)* and the randomness plots *(Figure 62)* are equally satisfactory, so both models could be valid. From previous analysis, the closer one was PSO.

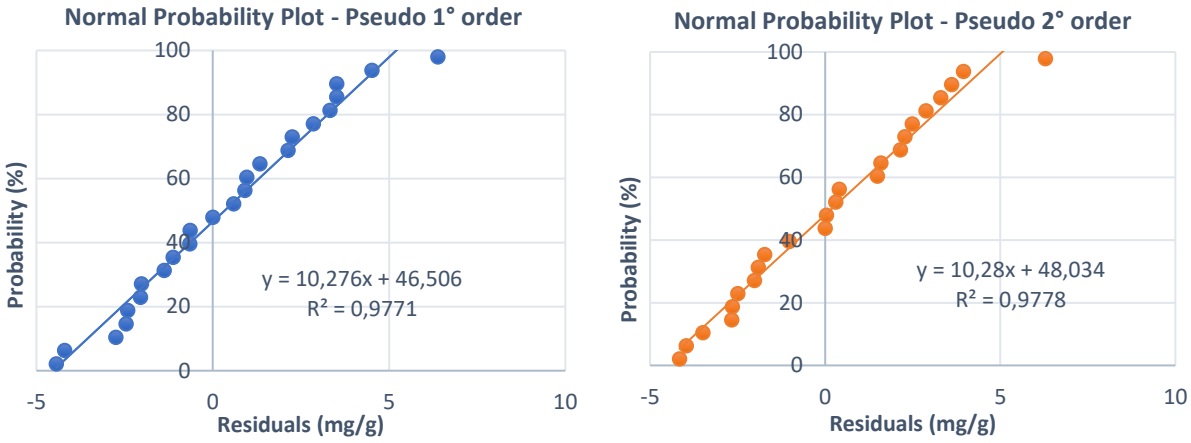

Figure 61: Normal probability plots for pseudo 1° and 2° order models – Biochar CO_2 0,25 g/L

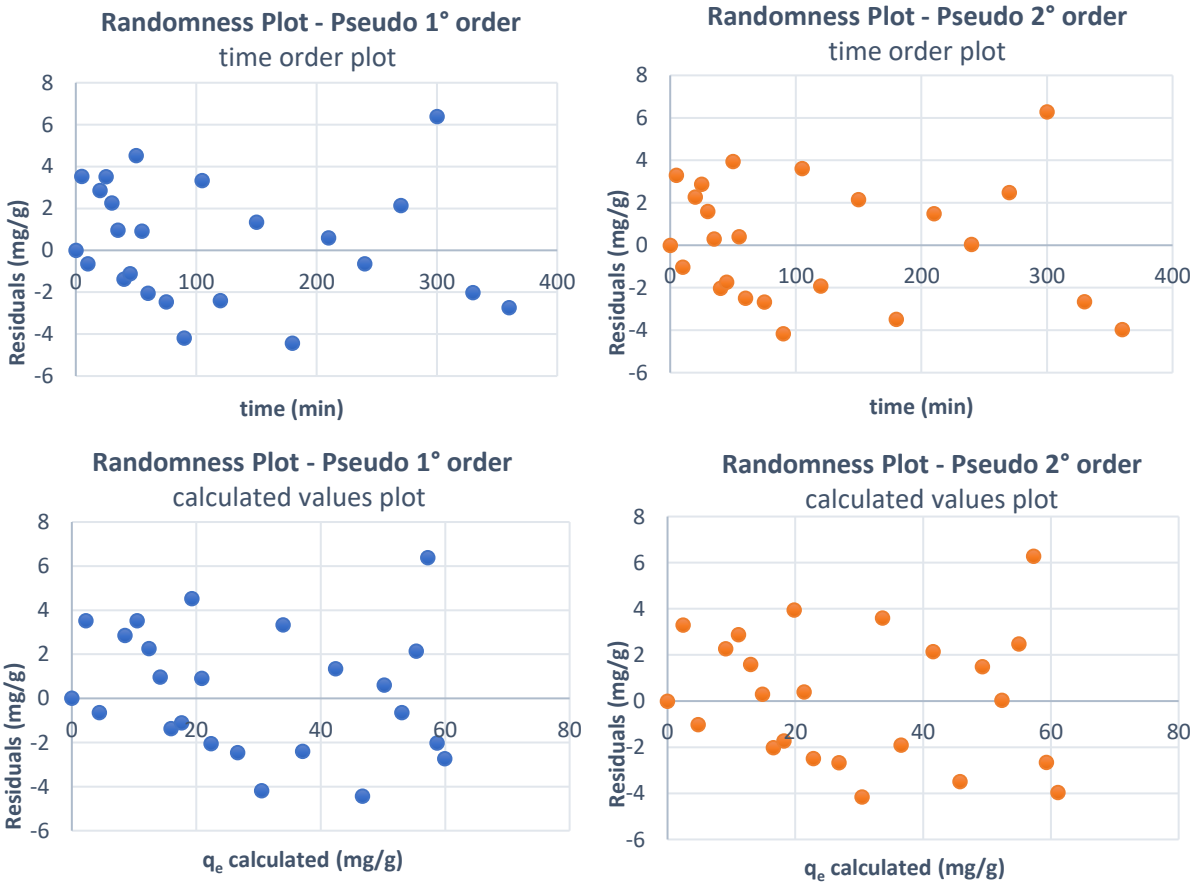

Figure 62: Randomness plots for pseudo 1° and 2° order models – Biochar CO_2 0,25 g/L

Biochar N_2 1 g/L

The values of R^2 for the normal probability plots (*Figure 63*) are very close. Both models are valid since there's no visible trend in randomness plots (*Figure 64*) and, based on q_e values, the best approximating model is the PFO.

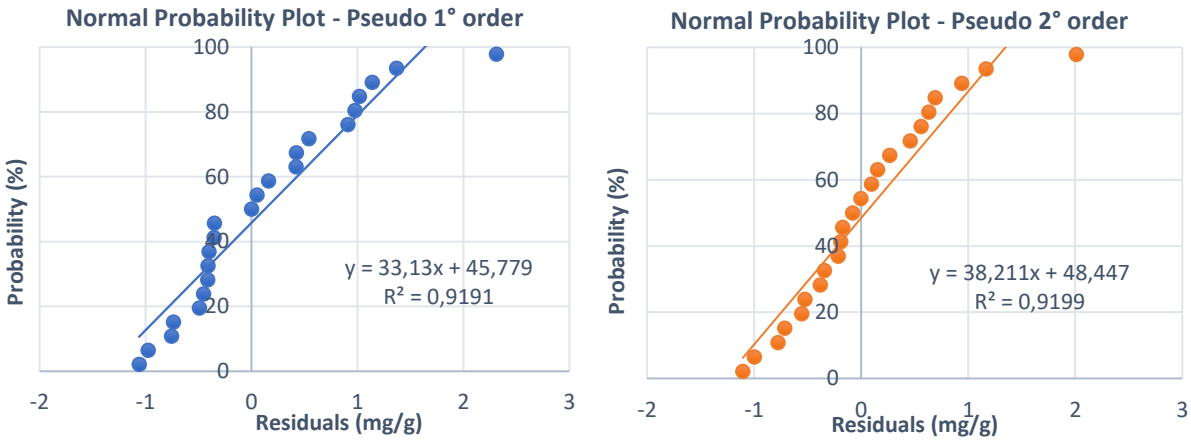

Figure 63: Normal probability plots for pseudo 1° and 2° order models – Biochar N_2 1 g/L

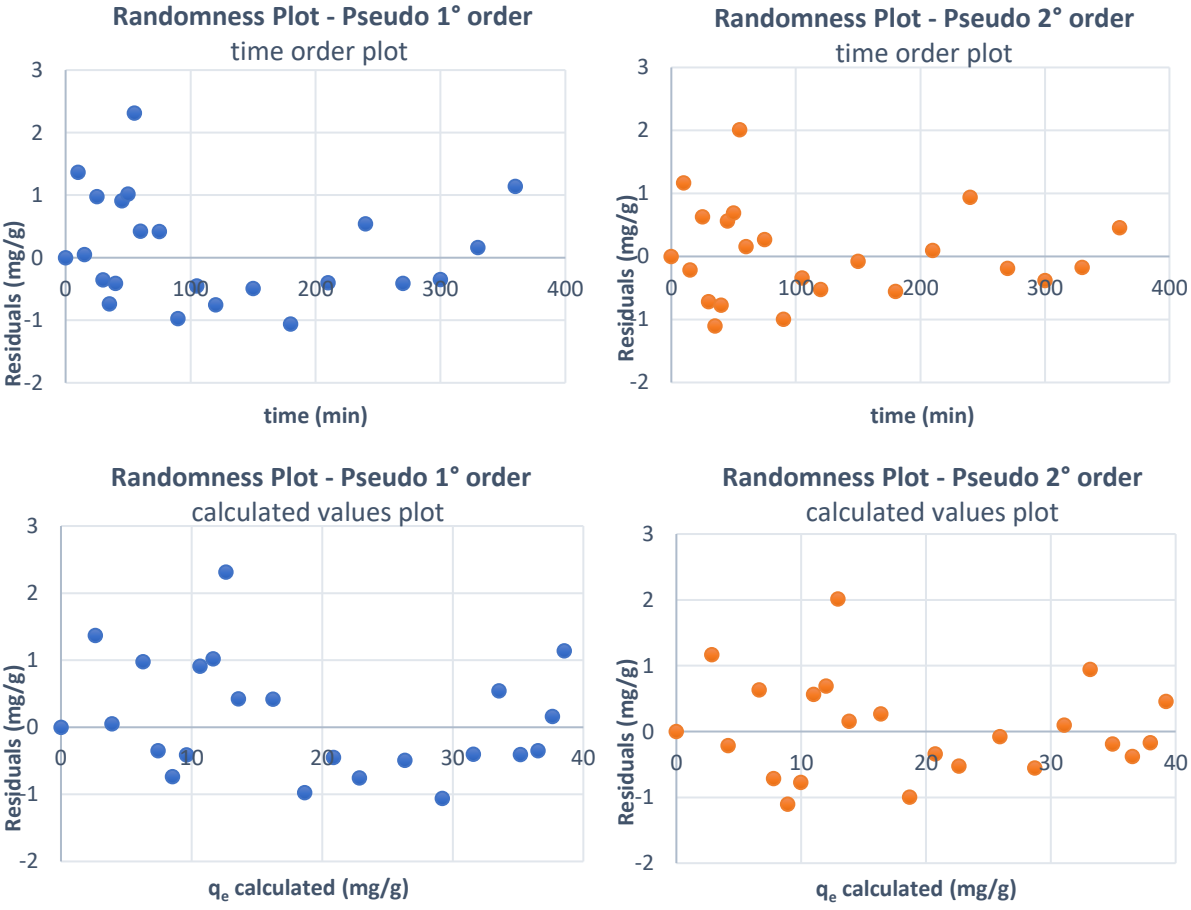

Figure 64: Randomness plots for pseudo 1° and 2° order models – Biochar N_2 1 g/L

Biochar N_2 0,5 g/L

Regarding the normal probability plots (*Figure 65)*, the best linear is the PFO one based on the R^2 value, but this is only because the PSO has a deviating point. Without it, the PSO shows a better trend and this is in accordance with what was found in the previous chapter. Trends from randomness plots *(Figure 66)* are not recognizable, so the models are valid.

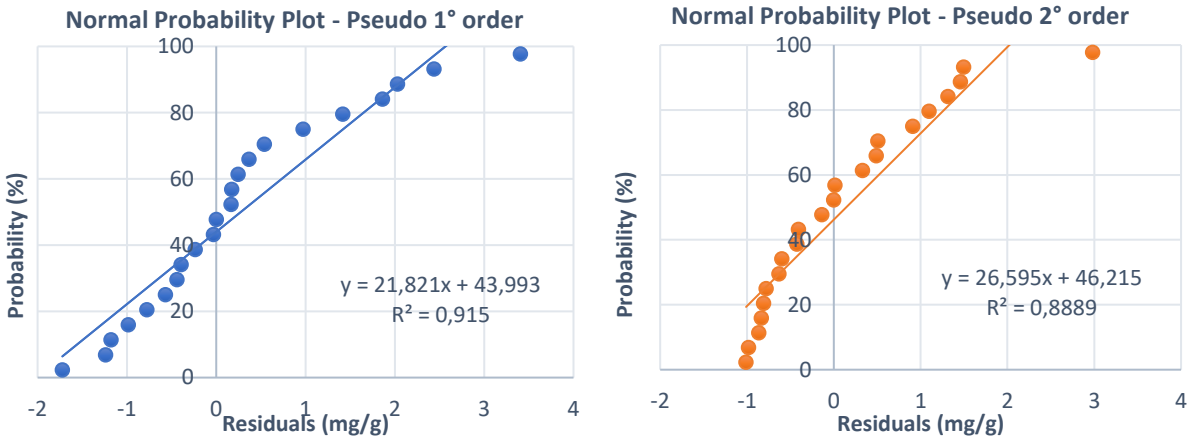

Figure 66: Normal probability plots for pseudo 1° and 2° order models – Biochar N_2 0,5 g/L

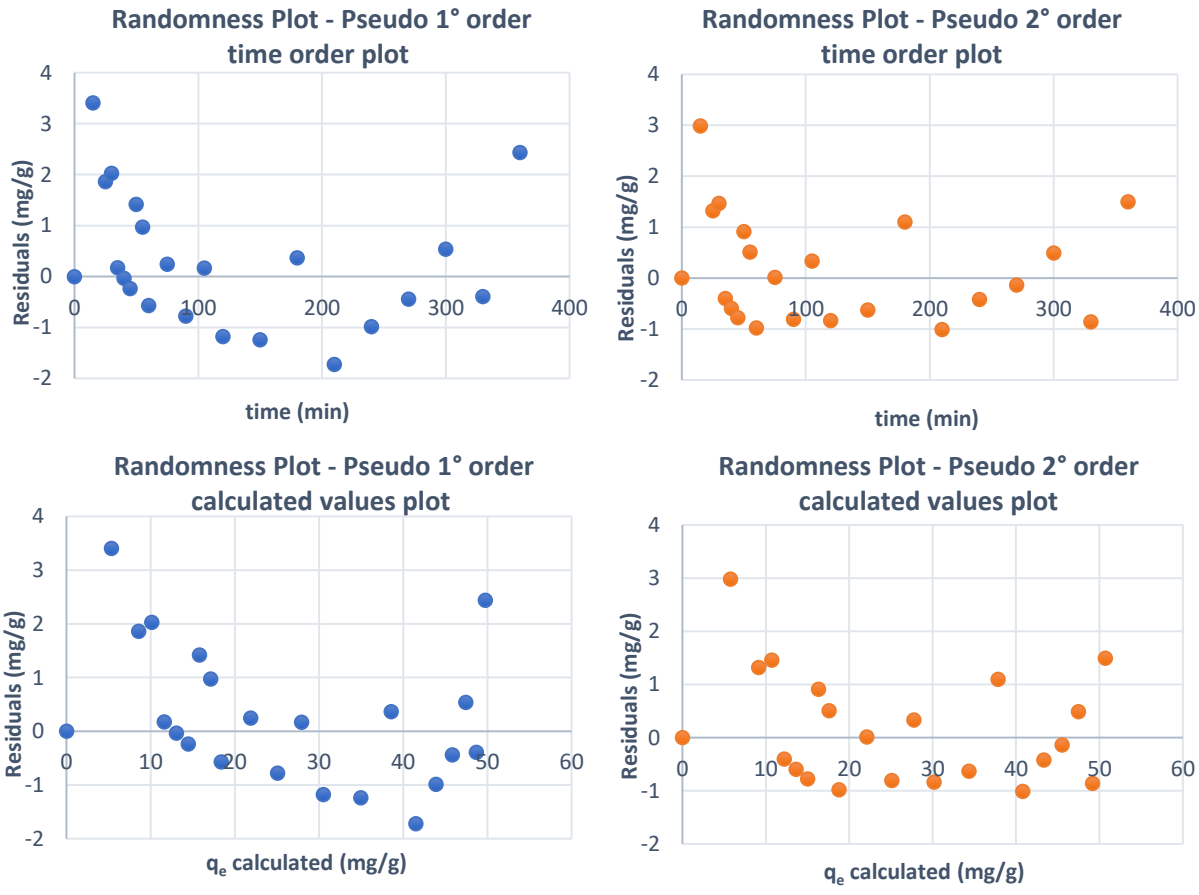

Figure 65: Randomness plots for pseudo 1° and 2° order models – Biochar N_2 0,5 g/L

Biochar N_2 0,25 g/L

In this case the PSO model has a more linear trend for the normal probability plots (*Figure 67)* and shows a random tendency in the randomness plot (*Figure 68*), so it validates what was found during the application of the models: the pseudo second order model approximate better the experimental data.

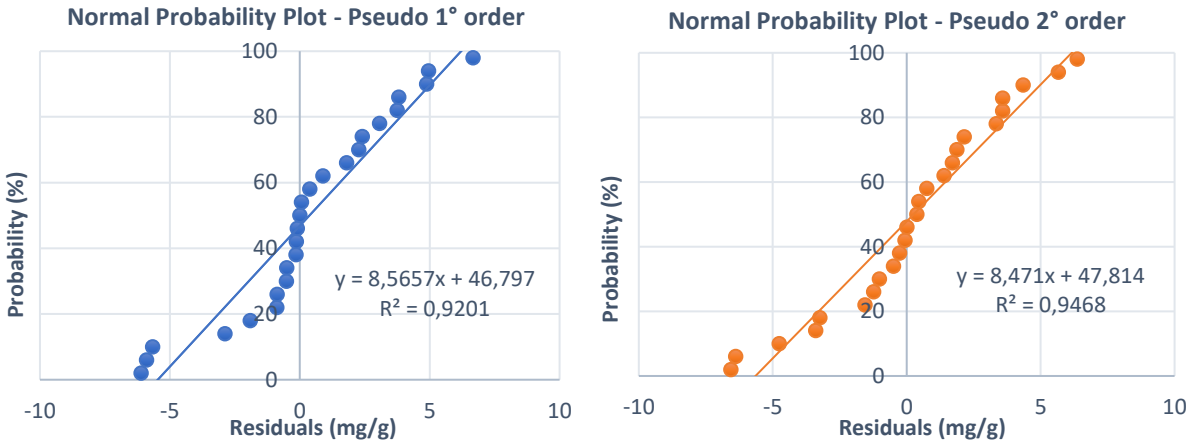

Figure 67: Normal probability plots for pseudo 1° and 2° order models – Biochar N_2 0,25 g/L

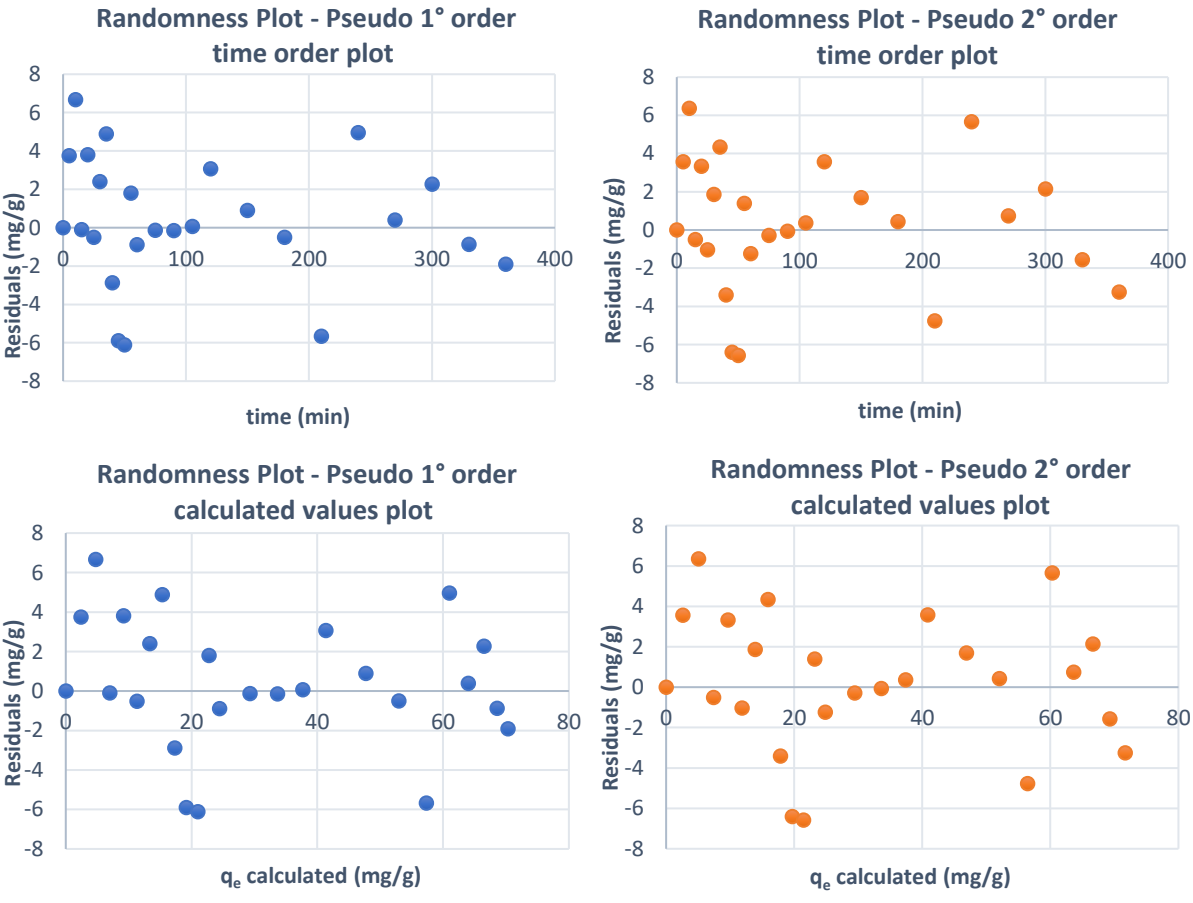

Figure 68: Randomness plots for pseudo 1° and 2° order models – Biochar N_2 0,25 g/L

Activated Carbon 1 g/L

In *Figure 69*, the normal probability plots show a higher R^2 for PSO model, even if the analysis conducted in the previous chapter illustrates that the PFO is a better model for activated carbon. Visually, the PFO has a better trend, so it can be assumed that the PFO is the correct model, also because it presents better randomness plots (*Figure 70)* than the PSO, that instead shows some trends.

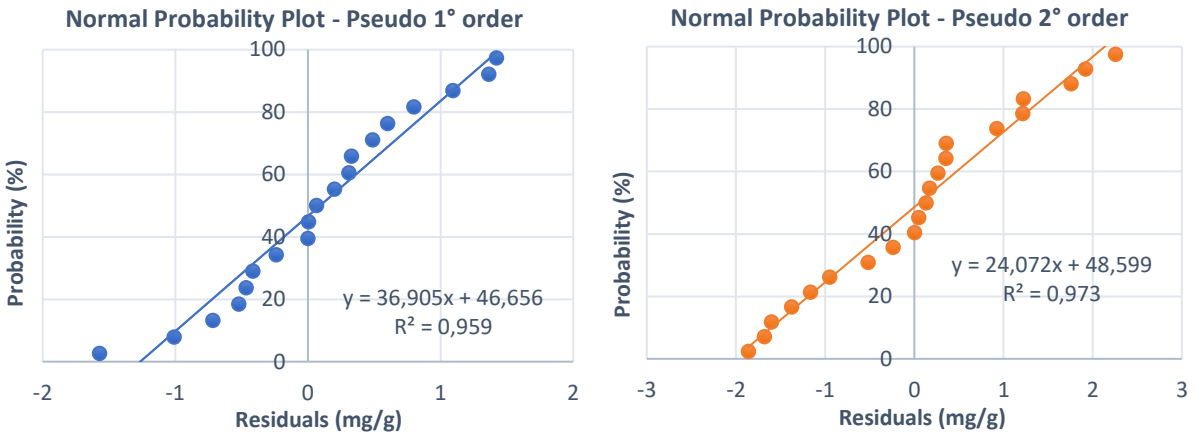

Figure 69: Normal probability plots for pseudo 1° and 2° order models – Activated Carbon 1 g/L

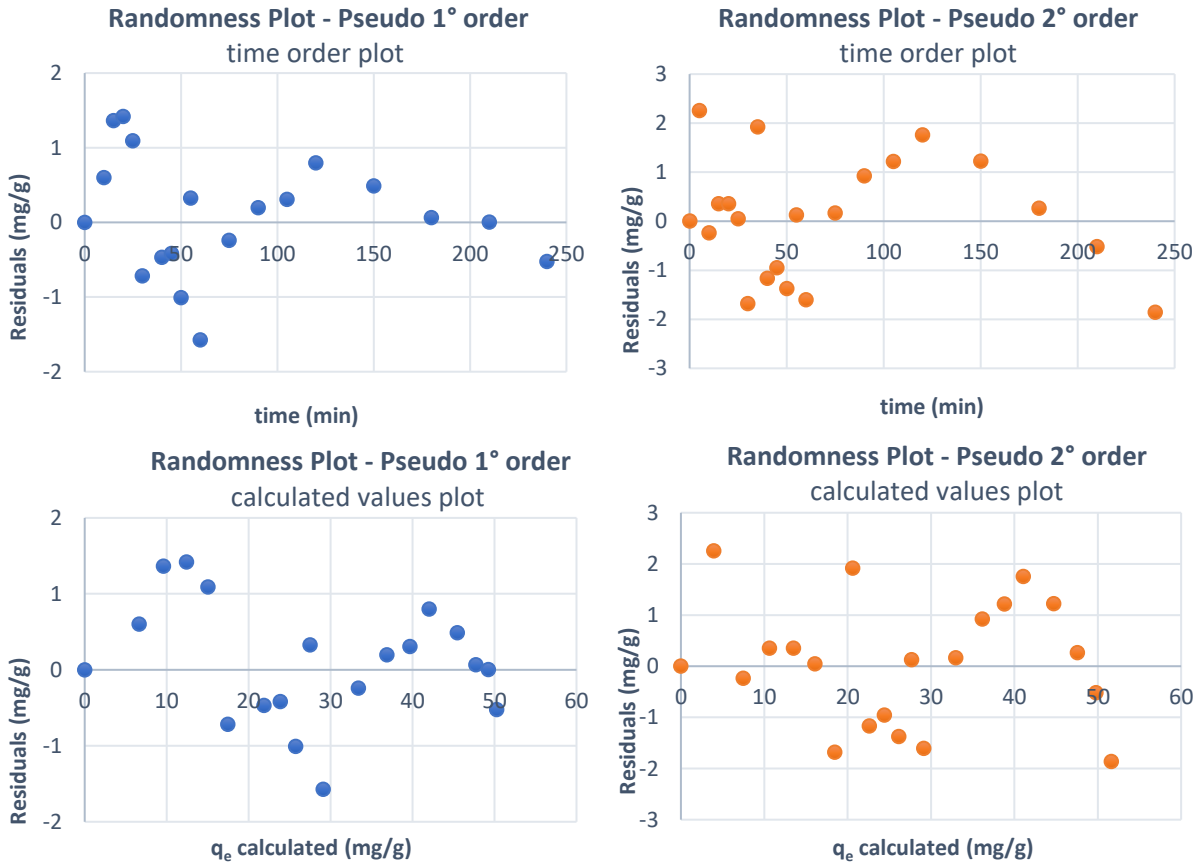

Figure 70: Randomness plots for pseudo 1° and 2° order models – Activated Carbon 1 g/L

Activated Carbon 0,5 g/L

The normal probability plots in *Figure 71* are both sufficiently linear to be considered valid, but looking at the randomness plots (*Figure 72*) the PSO seems to show a trend, so the right model to be chosen is the PFO, according also to the difference in q_e values found previously.

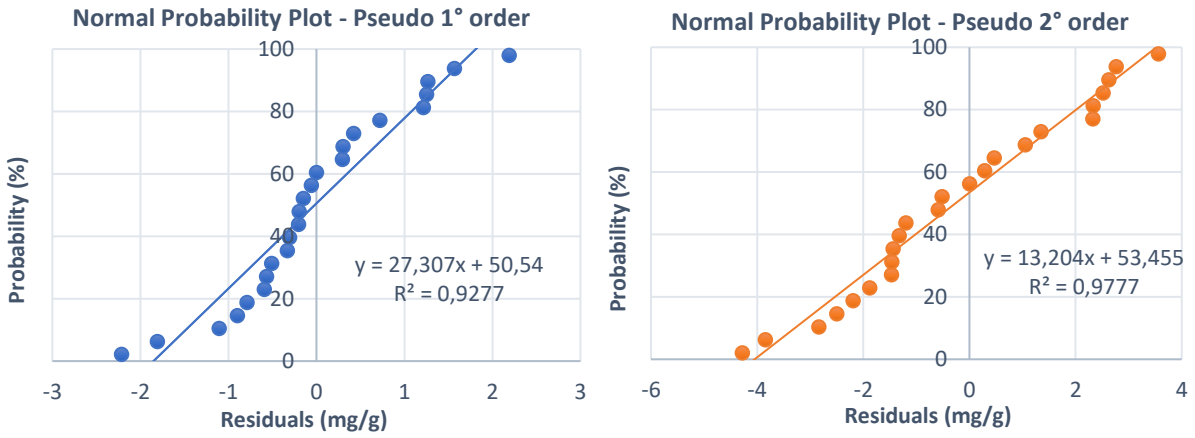

Figure 71: Normal probability plots for pseudo 1° and 2° order models – Activated carbon 0,5 g/L

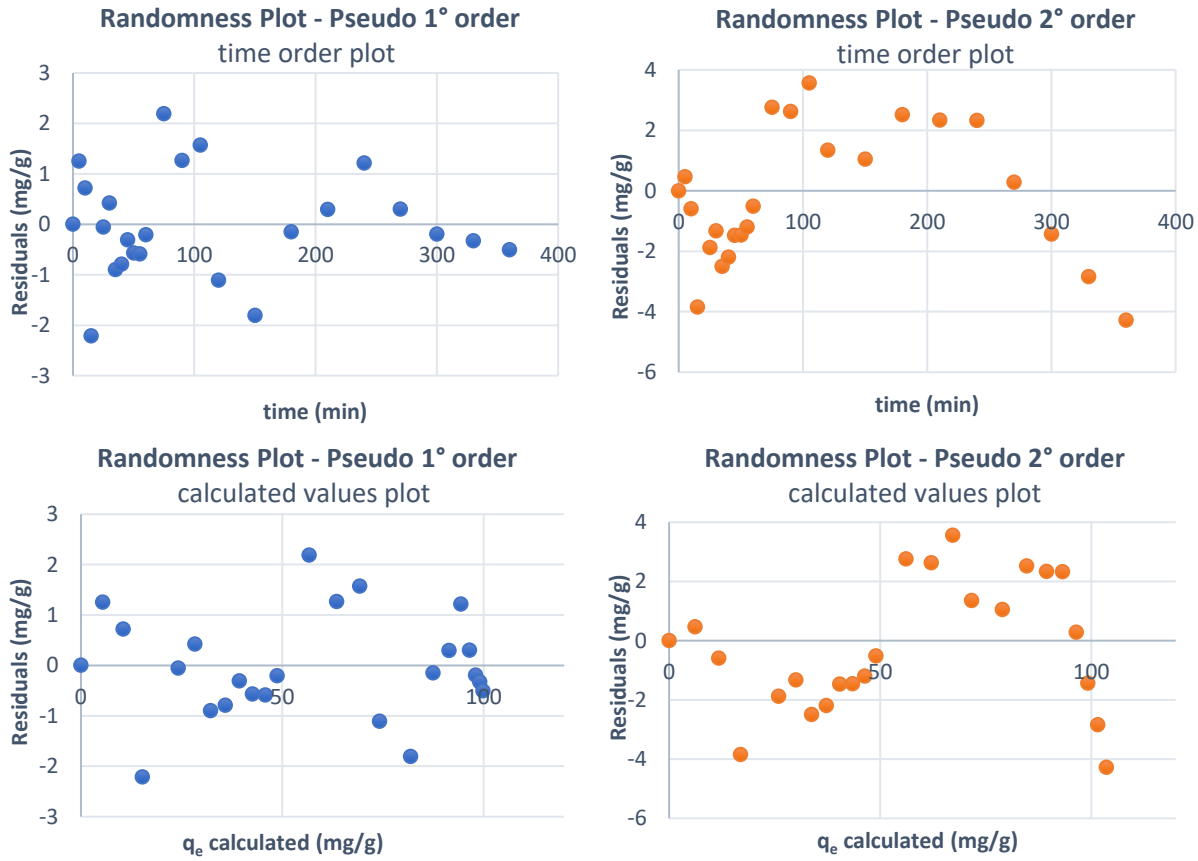

Figure 72: Randomness plots for pseudo 1° and 2° order models – Activated carbon 0,5 g/L

Activated Carbon 0,25 g/L

The pseudo first order model has a linear trend better than the pseudo second one, as it can be seen in *Figure 73*. Both models show a trend in the randomness plots (*Figure 74)*, but for PSO is more accentuated. Therefore, the best model is the PFO and it can be validated by these results.

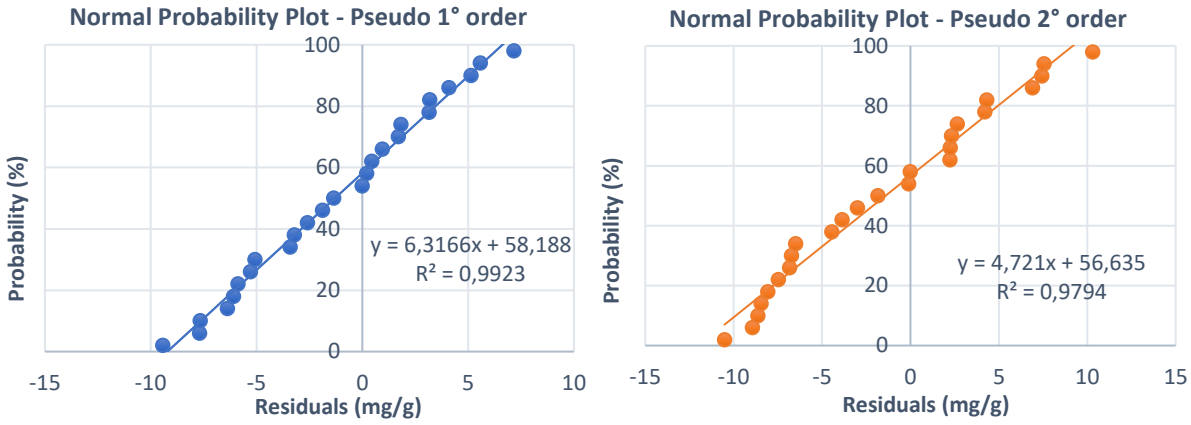

Figure 73: Normal probability plots for pseudo 1° and 2° order models – Activated carbon 0,25 g/L

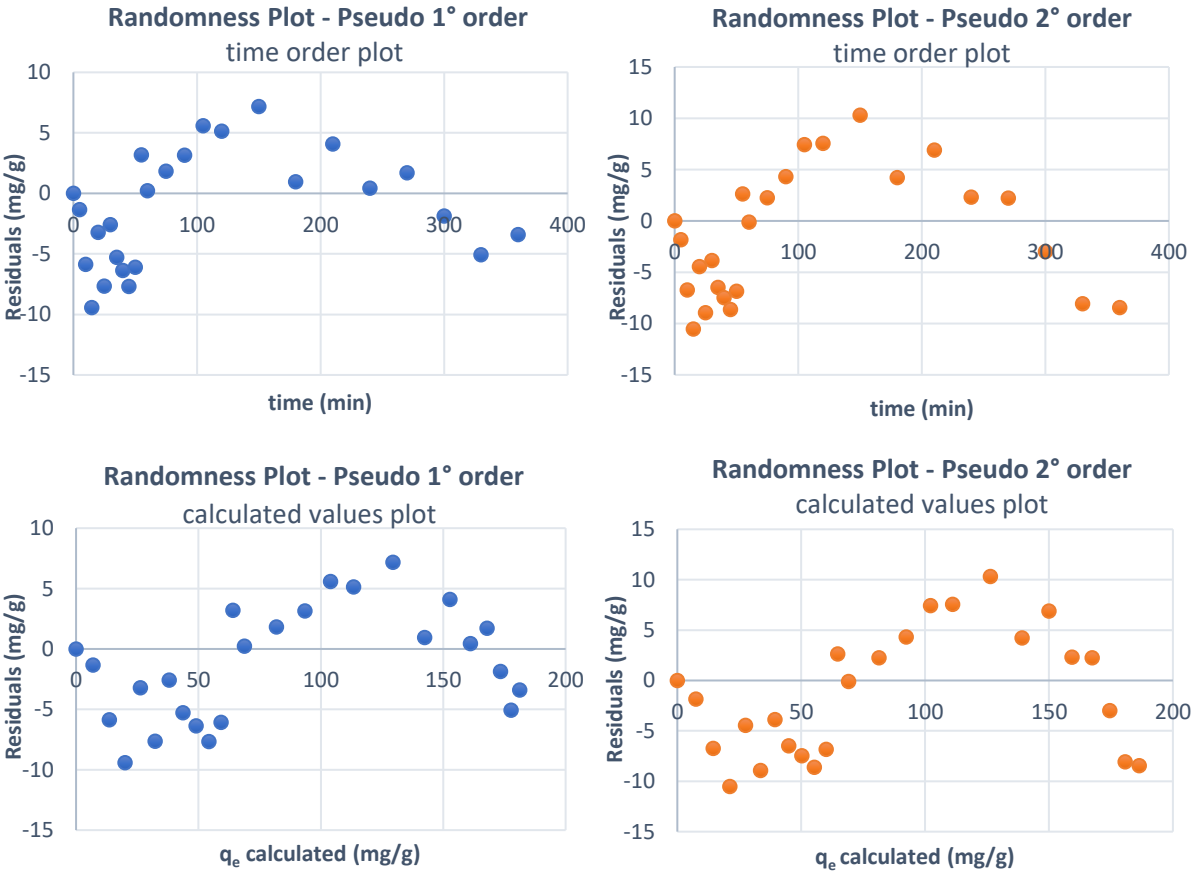

Figure 74: Randomness plots for pseudo 1° and 2° order models – Activated carbon 0,25 g/L

6.3.4 Thermodynamics

The thermodynamic analysis aims to identify the adsorption isotherm that best follows the trend of the experimental equilibrium adsorption capacity points (q_e). A comparison was made between the non-linearised Langmuir and Freundlich isotherms and the choice of the best approximating model was based on the value of the coefficient of determination R^2. The data analysis shows the following results (*Figure 75*):

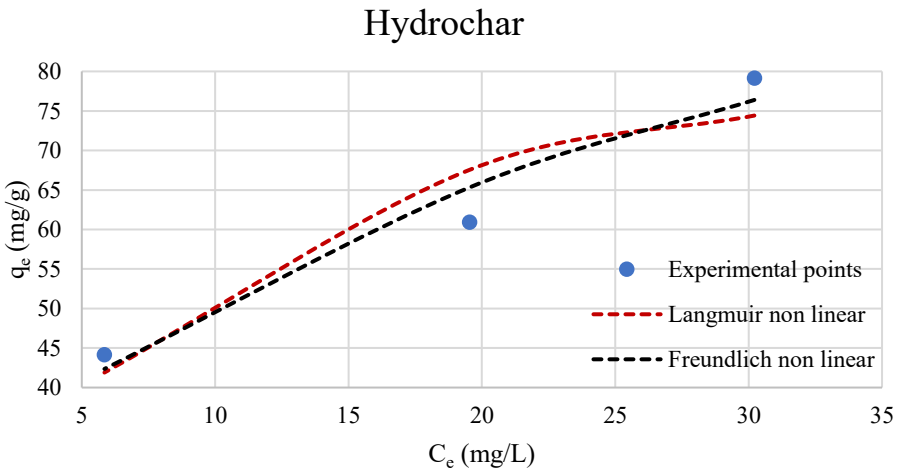

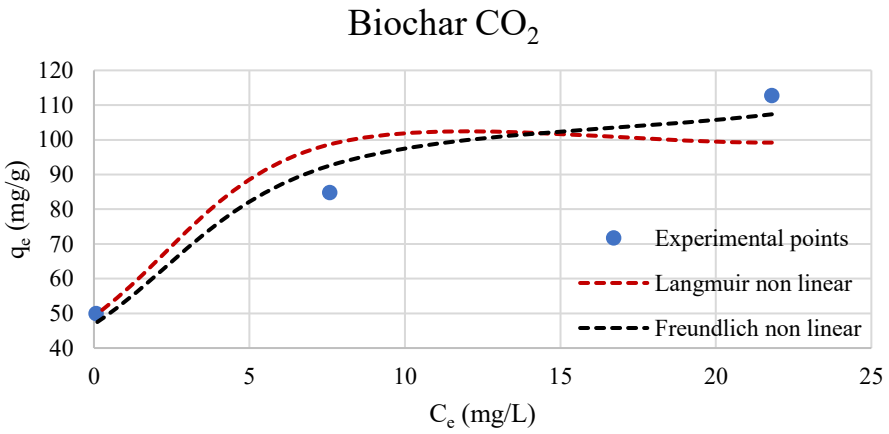

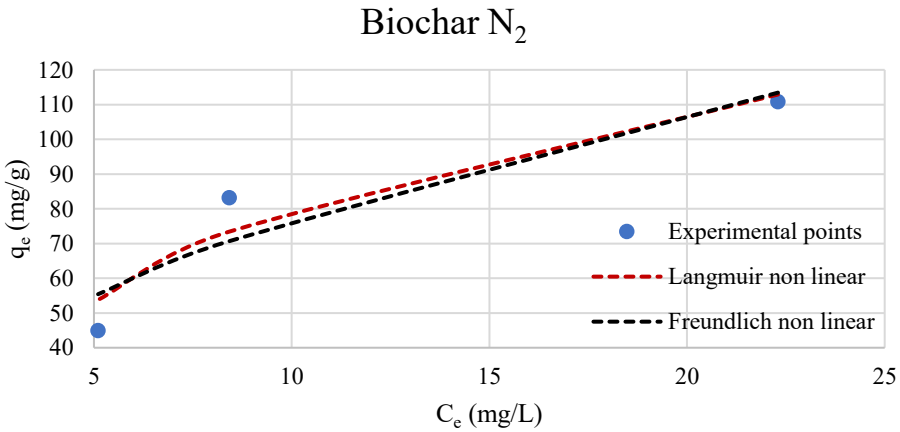

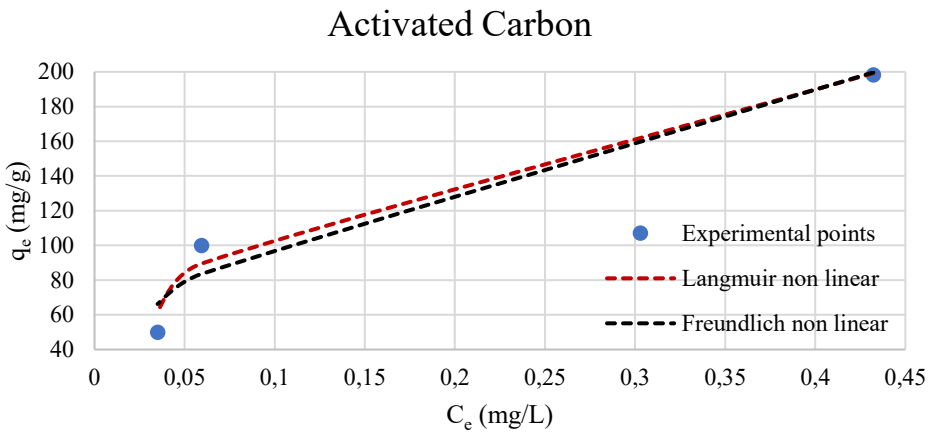

Figure 75: Fitting of experimental data by using Langmuir and Freundlich isotherms for all materials

As shown in *Table 13* and as can be seen from the graphs above, the Freundlich isotherm is a more accurate thermodynamic model for hydrochar and biochar CO_2. For biochar N_2 and activated carbon, on the other hand, the Langmuir isotherm model has R^2 values closer to 1.

Material	Langmuir Isotherm			Freundlich Isotherm		
	k_L (L/mg)	Qmax (mg/g)	R^2 (-)	k_F (mg/g)(L/mg)$^{1/n}$	n (-)	R^2 (-)
Hydrochar	0,1446	91,5	0,8790	22,4625	2,78	**0,9502**
Biochar CO_2	15,9558	99,5	0,7677	69,6645	7,13	**0,9508**
Biochar N_2	0,0926	167,6	**0,9016**	25,0994	2,06	0,8488
Activated Carbon	9,5290	247,6	**0,9762**	288,6651	2,28	0,9495

Table 13: Parameters estimation and model evaluation for Freundlich and Langmuir isotherms

The obtained data regarding Q_{max} (mg/g) can be compared to literature data as illustrated in *Table 14*. It could be useful also comparing the chosen models from kinetic and thermodynamic analysis with the ones found by performing a review of the existing literature on rice husk derived adsorbents.

However, it must be taken into account the fact that the results obtained from the experiments depends on the composition of the starting biomass, the operational conditions of the adsorption experiments and also the pyrolysis/HTC conditions.

Table 14: Literature comparison regarding max adsorption capacity and models

Reference	Material	Q_{max} (mg/g)	Kinetic model	Thermodynamic model
(Lang et al., 2021)	*Hydrochar*	12	Pseudo 2° order (Elovich)	Dubinin
(Chen et al., 2019)	*Biochar N_2*	23	Pseudo 2 °order	Langmuir
(Lang et al., 2021)	*Biochar N_2*	43	Pseudo 1° order (Elovich)	Langmuir
(Ahmad et al., 2020)	*Biochar N_2*	18	Pseudo 2° order	Langmuir
(Hamad & Idrus, 2022)	*Biochar N_2*	608	Pseudo 2° order	Langmuir
(Neolaka et al., 2023)	*Biochar N_2*	578	Pseudo 2° order	Langmuir
(Mahapatra et al., 2022)	*Activated Carbon*	225	Pseudo 1° order	Langmuir

In the specific case of biochar N_2, the data found in this study are almost all in agreement with the literature, both in terms of kinetic and thermodynamic models. Hydrochar and biochar CO_2, on the other hand, have been studied less, so only one example is given for hydrochar, which, however, was found to be following different models to that tested in this work. Activated carbon is also consistent with the analysed articles. Regarding the maximum adsorption capacity, as reported from (Hamad & Idrus, 2022), these values fall in the range of biochar that is between 2,06 and 1282,6 mg/g.

6.3.5 Comparison between materials

To complete the analysis of the materials, a comparison was conducted between them at the same initial adsorbent concentration. *Figure 76* shows that in all three cases at different concentrations, the best performing material is still commercial activated carbon. The other materials show a lower performance, although a good result is obtained from the biochar CO_2 at an initial concentration of 1 g/L. In this case, the curve for biochar CO_2 is very close to that of activated carbon throughout the experiment.

It can be noticed that, for all materials, the performance gap decreases as the concentration of adsorbent material increases (especially for biochar CO_2), as already shown in *Figure 34* on the Effect of adsorbent dosage of section *6.2.1*.

In all cases at different concentrations, the worst performance is shown by hydrochar. Very similar trends are followed by biochar N_2 which, unlike biochar CO_2, at C_0 = 1 g/L shows no improvement in performance and continues to be very similar to hydrochar.

In the case at lower concentration, the performance of hydrochar, biochar CO_2 and biochar N_2 are almost overlapping, with an inversion between biochar CO_2 and biochar N_2 compared to the other cases, as biochar N_2 now performs slightly better than biochar CO_2; this, however, is not at all observed in the cases at C_0 = 0,5 g/L and C_0 = 1 g/L where biochar CO_2 is the material that is closest to commercially available activated carbon.

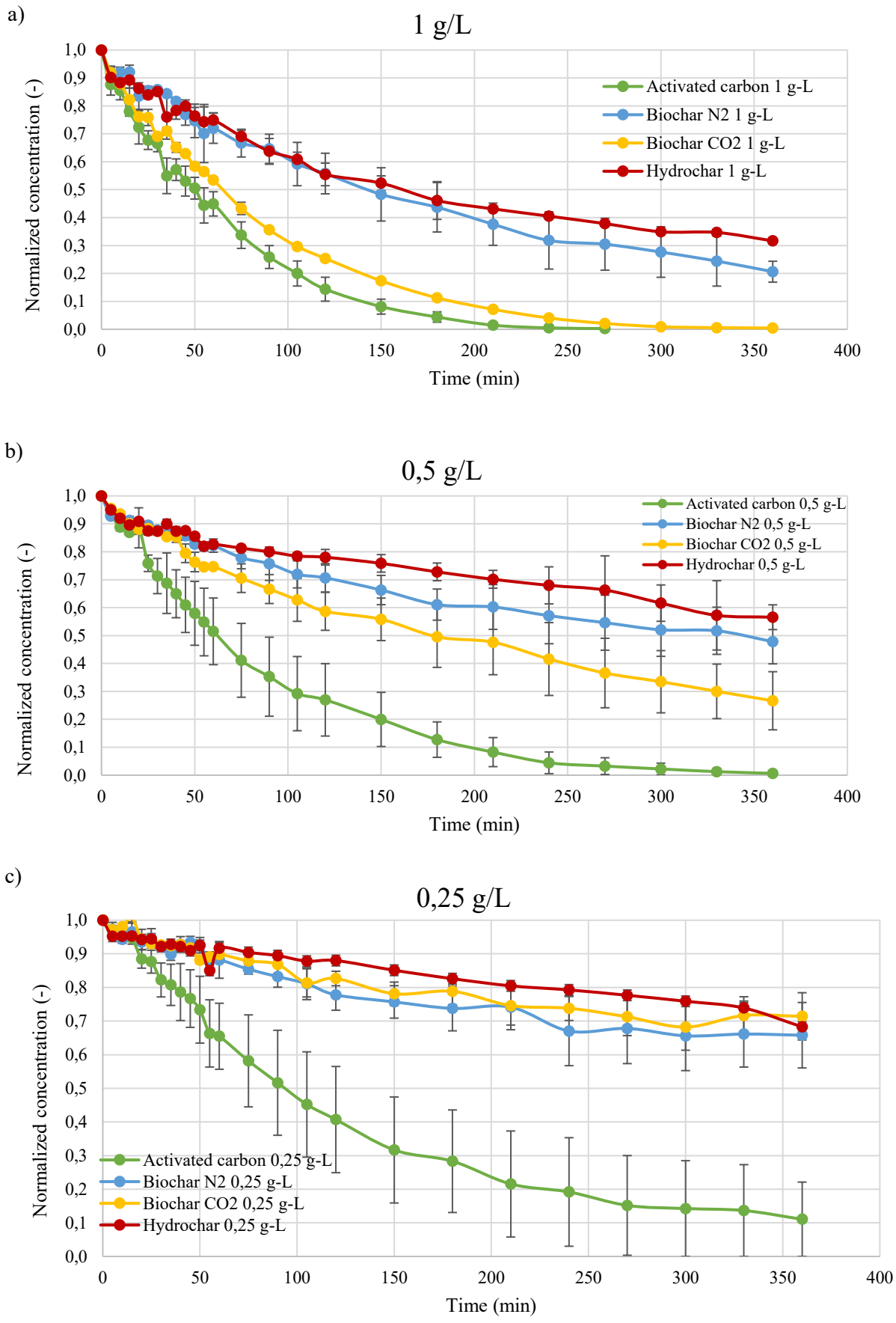

Figure 76: Comparison between different materials at same dosage a) 1 g/L b) 0,5 g/L c) 0,25 g/L

A further analysis can be conducted by comparing the curves referring to experiments conducted at C_0 = 0,5 g/L with those conducted at the same concentration, but with a pH of 11,5 (*Figure 77*), indicated with dotted lines.

It follows that the cases with a modified pH solution generally show a better performance. In particular, during the first 60 minutes of the experiment, biochar CO_2 shows a more pronounced MB removal than the standard material taken as reference, i.e. activated carbon, due to its lower curve. As time increases, this advantage is lost and biochar CO_2 achieves a slightly lower final concentration than hydrochar.

A particular trend is found in biochar N_2 with a solution at pH = 11,5: during the first hour, the slope of the curve is moderate, but then it shows an increase that leads this material to significantly outperform all the other materials; biochar N_2 under these conditions of modified pH manages to achieve complete removal of the pollutant around 200 minutes from the start of the experiment, showing a higher removal rate even than activated carbon, which tends to the asymptote of complete removal only around 6 hours into the experiment.

By varying the pH, therefore, biochar N_2 reveals performance comparable with the commercial standard of activated carbon.

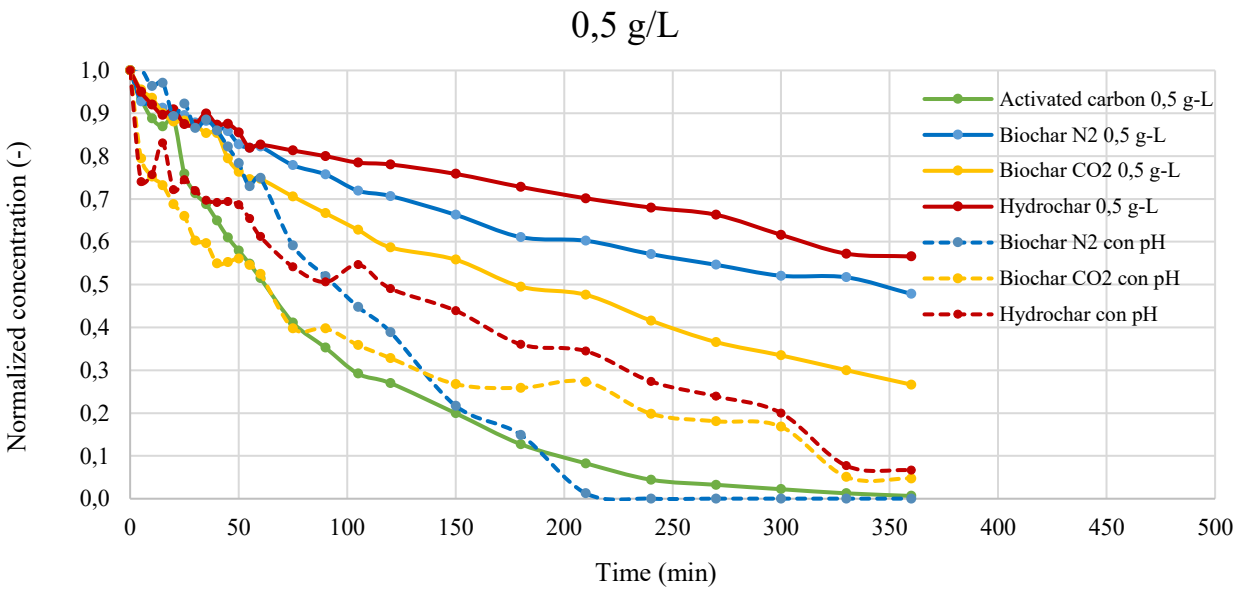

Figure 77: Comparison between different materials at dosage = 0,5 g/L, including the effect of pH = 11,5

The same information reported in these graphs can be summarized in *Table 15*, showing the removal efficiency of MB after 6 hours of contact time:

	Removal Efficiency (%)				
Material	**C_{ads} = 1 g/L**	**C_{ads} = 0,5 g/L**	**C_{ads} = 0,25 g/L**	**pH = 10**	**pH = 11,5**
Hydrochar	68,3	43,4	31,7	78,99	93,4
Biochar CO_2	99,5	73,4	28,6	72,8	95,3
Biochar N_2	79,4	52,2	34,2	-	99,9
Activated Carbon	99,8	99,4	88,9	-	-

Table 15: Comparison of removal efficiency between materials (pH-modified data are at C_{ads} = 0,5 g/L)

As a conclusion, increasing the pH has a beneficial effect on removal efficiency for all the materials thanks to the electrostatic forces, and the cases that show performances closer to the activated carbon are biochar CO_2 at high dosage and biochar N_2 at high pH.

6.4 Scale-up

For the design of a batch adsorber, the material balances and coefficients of the isotherms lead to the definition of the amount of adsorbent required for a certain volume of effluent, parameterised according to the removal efficiency to be achieved from an initial concentration of 50 mg/L of Methylene Blue.

In *Figure 78*, biochar CO_2 has been taken as an example due to its best performances (in the case of no pH modification) with respect to the other innovative materials. According to the thermodynamic study, it follows the Freundlich isotherm, so its equation was substituted in the mass balance of the pollutant. The graph shows different lines associated to different removal percentages, going from 70% to a maximum of 90%.

The batch adsorber is single-stage, so it assumes removal in a single step: for example, for a 90% removal of the input pollutant in a volume of 2000 to 20000 L, 1 to 10 kg of adsorbent material are required.

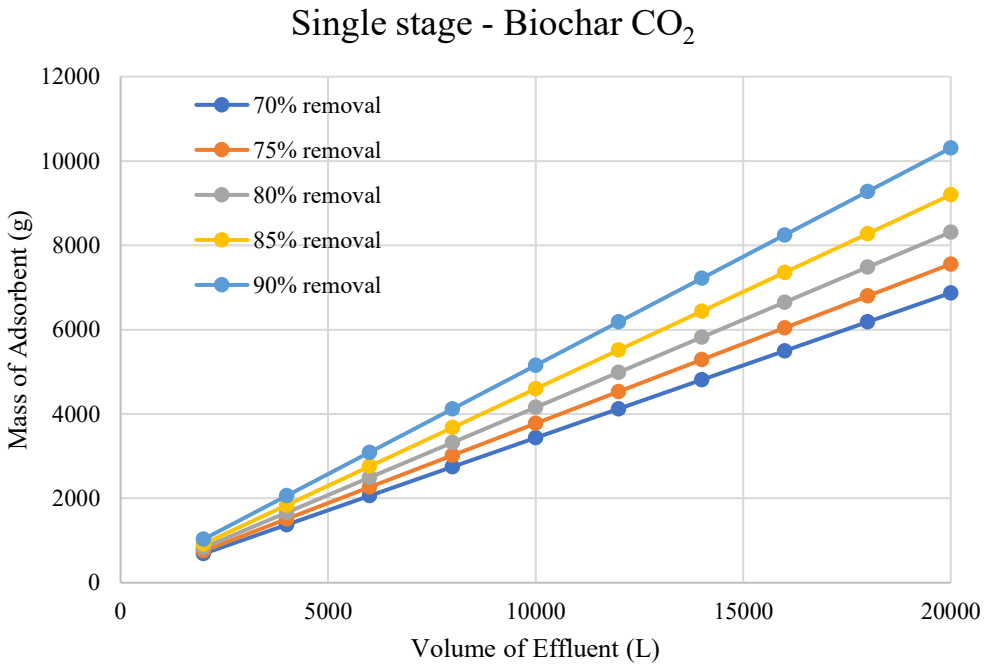

Figure 78: Design equation for a single-stage adsorber, referred to biochar CO_2

This result can be compared to that of activated carbon in *Figure 79*, which follows the Langmuir isotherm. For a removal of 90 % in a volume of at most 20000 L, it requires a lower mass (slightly more than half the amount) than biochar CO_2, equivalent to almost 4 kg of activated carbon.

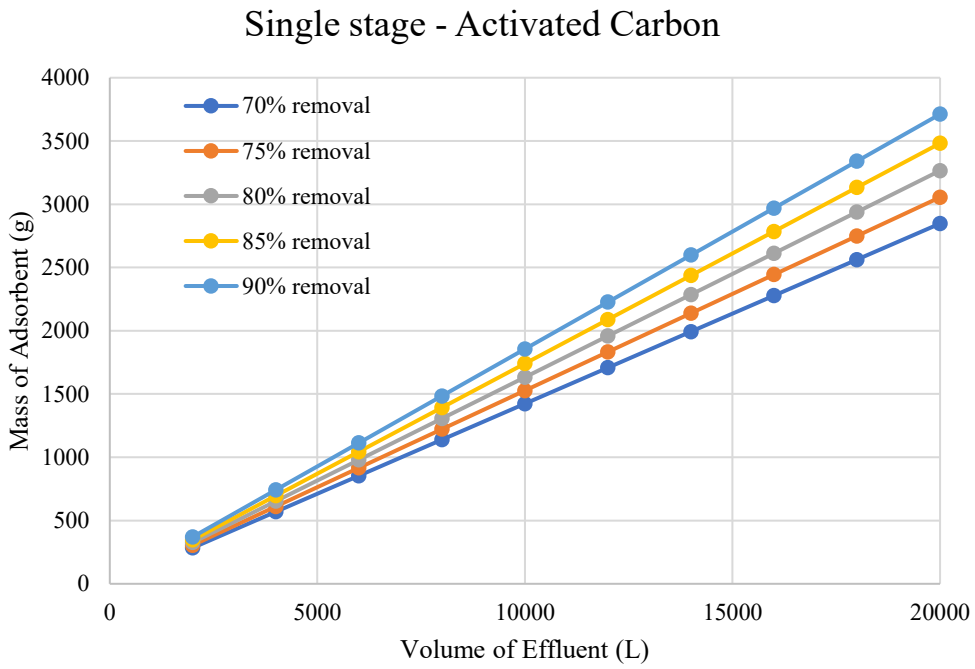

Figure 79: Design equation for a single-stage adsorber, referred to activated carbon

Finally, the graph including all analysed materials is shown (*Figure 81)*. The material that allows the MB removal with the lowest mass is definitely activated carbon.
On the other hand, with a slightly steeper slope there is biochar CO_2, which, almost like activated carbon, shows no particular differences in slope between the 70% removal case (bottom line) and the 90% removal case (top line).

In particular, it was noted that the 80% removal case is approximately overlapping with the 75% removal case for biochar N_2 (dotted line). Thus, for the same volume to be treated, the same amount of biochar CO_2 and biochar N_2 can be used, resulting in 80% and 75% pollutant removal, respectively.
The straight lines of biochar N_2 show varying slopes going from the minimum to the maximum removal, exactly as is the case with hydrochar, which, moreover, is the least efficient, needing a mass of more than 20 kg for a volume of 20000 L in the case of 90% removal efficiency.

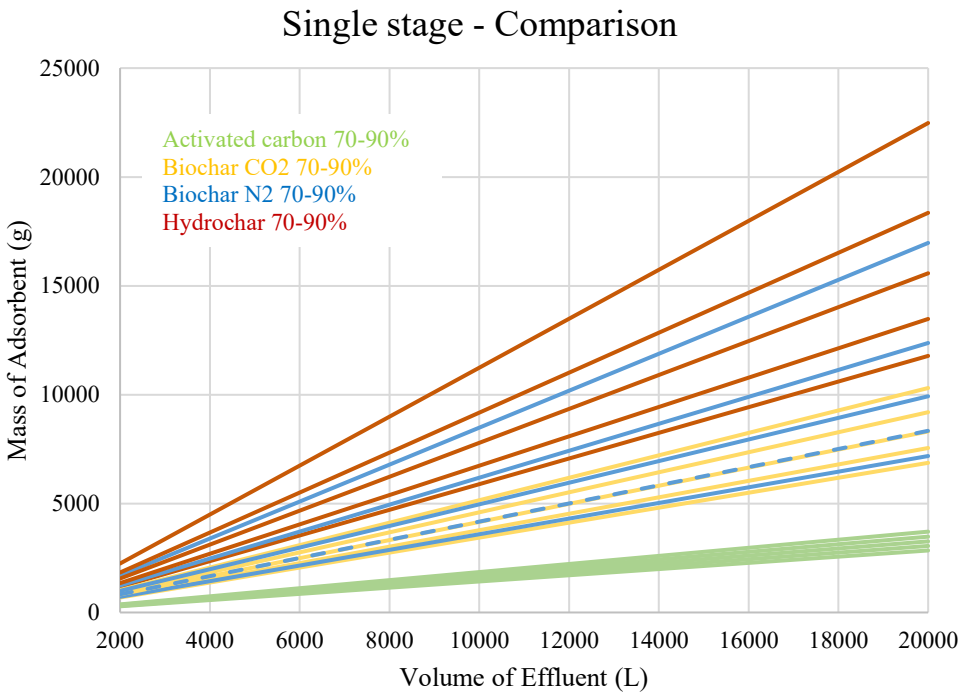

Figure 81: Comparison between design equations of different materials

7. Conclusions and Future Developments

From this thesis work, therefore, potential alternatives to activated carbon have been identified, such as biochar CO_2 and biochar N_2 under conditions of higher pH than its pH_{PZC}. These innovative adsorbent materials turn out to be efficient and renewable, since they are derived from waste materials of the rice processing industry, i.e. rice husk. Currently, rice husk is an agricultural waste and by-product of the rice milling industry with a total of 100 million tonnes per year (Rafatullah et al., 2010), so the use of this material as a new resource for the production of adsorbents is an advantage not only from the point of view of water treatment, but also for the disposal of this waste, which is avoided in this way, following circular economy perspective.

In the future, more in-depth studies are required to evaluate the most suitable biomass for this type of application and the relevant pyrolysis and/or hydrothermal carbonization conditions. In addition to this, an extension of the adsorption study is also required to take into account the effect of other operating conditions not analysed in the course of this thesis, the possible application on dyes of a different nature, e.g. of anionic origin, and an in-depth economic analysis to quantify the benefits introduced by the use of these emerging materials compared to the use of commercial activated carbon, with the aim of promoting their use on a larger scale. In a rough economic comparison, the production of adsorbent materials from agricultural waste for dye removal is approximately five times cheaper than the production of commercial activated carbon (CAC). Therefore, even in cases where low-cost adsorbents have lower adsorption capacities than activated carbon, as was the case with hydrochar in this study, they can still be applied as alternatives to CAC (Kannan & Sundaram, 2001).

The literature suggests that it is possible to further increase the removal efficiency of these low-cost adsorbents by also providing activation or modification steps for the material (Rafatullah et al., 2010).

This study, like most of the studies reported in the literature, was conducted in batch. Thus, in the future, the use of continuous flow systems may be considered, with application also at industrial level.

Furthermore, it is interesting and stimulating to study the possibility of regenerating the adsorbent material and recovering the MB. Regeneration requires desorption of the adsorbed substance: the most common methods include thermal, acid, vacuum, biological, organic solvent, microwave-assisted, ultrasonic, etc. desorption. To date, few studies in the literature deal comprehensively with the end-of-life of the adsorbent material and sustainable regeneration methods, which, however, are important to reduce process costs, recover the adsorbed pollutant and reduce the generation of waste for disposal.
After several cycles of adsorption followed by regeneration, the effectiveness of the material decreases and, at some point, it must be disposed of in a landfill, appropriately stabilized, or burnt. A more sustainable alternative lies in recycling for reuse in other applications, such as in the construction industry for the production of cement clinkers, bricks and roads, as a catalyst, fertilizer or for the manufacturing of ceramics (Hamad & Idrus, 2022).

A further field of study yet to be explored is the treatment of wastewater containing more than one pollutant, so as to make the system even more flexible and adaptable to the needs of the textile industry and beyond. These future developments could help spread and expand the use of adsorbents derived from waste biomass, which has proven to be an efficient, cost-effective and renewable alternative that can bring innovation to the field of water treatment.

References

Adam, O. (2016). Removal of Resorcinol from Aqueous Solution by Activated Carbon: Isotherms, Thermodynamics and Kinetics. *American Chemical Science Journal*, *16*(1), 1–13. https://doi.org/10.9734/acsj/2016/27637

Ahiduzzaman, M., & Sadrul Islam, A. K. M. (2016). Preparation of porous bio-char and activated carbon from rice husk by leaching ash and chemical activation. *SpringerPlus*, *5*(1). https://doi.org/10.1186/s40064-016-2932-8

Ahmad, A., Khan, N., Giri, B. S., Chowdhary, P., & Chaturvedi, P. (2020). Removal of methylene blue dye using rice husk, cow dung and sludge biochar: Characterization, application, and kinetic studies. *Bioresource Technology*, *306*. https://doi.org/10.1016/j.biortech.2020.123202

Ahmad, M., Rajapaksha, A. U., Lim, J. E., Zhang, M., Bolan, N., Mohan, D., Vithanage, M., Lee, S. S., & Ok, Y. S. (2014). Biochar as a sorbent for contaminant management in soil and water: A review. In *Chemosphere* (Vol. 99, pp. 19–33). Elsevier Ltd. https://doi.org/10.1016/j.chemosphere.2013.10.071

Akhtar, K., Khan, S. A., Khan, S. B., & Asiri, A. M. (2018). Scanning electron microscopy: Principle and applications in nanomaterials characterization. In *Handbook of Materials Characterization* (pp. 113–145). Springer International Publishing. https://doi.org/10.1007/978-3-319-92955-2_4

And, O. F. O., & Odebunmi E O. (2010). Freundlich and Langmuir Isotherms Parameters for Adsorption of Methylene Blue by Activated Carbon Derived from Agrowastes. *Advances in Natural and Applied Sciences*, *4*(3), 281–288. www.lenntech.com/feedbach_uk,

Assorbanza. (2023, November 28). Wikipedia. https://it.wikipedia.org/wiki/Assorbanza

Brewer, C. E., & Brown, R. C. (2012). 5.18 - Biochar. In *Comprehensive Renewable Energy* (pp. 357–384). Elsevier. https://doi.org/10.1016/B978-0-08-087872-0.00524-2

Cha, J. S., Park, S. H., Jung, S. C., Ryu, C., Jeon, J. K., Shin, M. C., & Park, Y. K. (2016). Production and utilization of biochar: A review. In *Journal of Industrial and Engineering Chemistry* (Vol. 40, pp. 1–15). Korean Society of Industrial Engineering Chemistry. https://doi.org/10.1016/j.jiec.2016.06.002

Chen, S., Qin, C., Wang, T., Chen, F., Li, X., Hou, H., & Zhou, M. (2019). Study on the adsorption of dyestuffs with different properties by sludge-rice husk biochar: Adsorption capacity, isotherm, kinetic, thermodynamics and mechanism. *Journal of Molecular Liquids*, *285*, 62–74. https://doi.org/10.1016/j.molliq.2019.04.035

CHNS MacroCube. (2023, November 14).

Draper, N. R., & Smith, H. (1998). *Applied Regression Analysis*.

El-Halwany, M. M. (2010). Study of adsorption isotherms and kinetic models for Methylene Blue adsorption on activated carbon developed from Egyptian rice hull (Part II). *Desalination*, *250*(1), 208–213. https://doi.org/10.1016/j.desal.2008.07.030

Ghaedi, M., Nasab, A. G., Khodadoust, S., Rajabi, M., & Azizian, S. (2014). Application of activated carbon as adsorbents for efficient removal of methylene blue: Kinetics and equilibrium study.

Journal of Industrial and Engineering Chemistry, *20*(4), 2317–2324. https://doi.org/10.1016/j.jiec.2013.10.007

Guilhen, S. N., Watanabe, T., Silva, T. T., Rovani, S., Marumo, J. T., Tenório, J. A. S., Mašek, O., & Araujo, L. G. de. (2022). Role of Point of Zero Charge in the Adsorption of Cationic Textile Dye on Standard Biochars from Aqueous Solutions: Selection Criteria and Performance Assessment. *Recent Progress in Materials*, *4*(2), 1–1. https://doi.org/10.21926/rpm.2202010

Gupta, M., Savla, N., Pandit, C., Pandit, S., Gupta, P. K., Pant, M., Khilari, S., Kumar, Y., Agarwal, D., Nair, R. R., Thomas, D., & Thakur, V. K. (2022). Use of biomass-derived biochar in wastewater treatment and power production: A promising solution for a sustainable environment. In *Science of the Total Environment* (Vol. 825). Elsevier B.V. https://doi.org/10.1016/j.scitotenv.2022.153892

Hamad, H. N., & Idrus, S. (2022). Recent Developments in the Application of Bio-Waste-Derived Adsorbents for the Removal of Methylene Blue from Wastewater: A Review. In *Polymers* (Vol. 14, Issue 4). MDPI. https://doi.org/10.3390/polym14040783

Huyen Thuong Bui, Phuong Thu Le, & Thu Phuong Nguyen. (2022). 9 -. *Vietnam Journal of Earth Sciences*, *44*(2), 273–285.

Ighalo, J. O., Rangabhashiyam, S., Dulta, K., Umeh, C. T., Iwuozor, K. O., Aniagor, C. O., Eshiemogie, S. O., Iwuchukwu, F. U., & Igwegbe, C. A. (2022). Recent advances in hydrochar application for the adsorptive removal of wastewater pollutants. *Chemical Engineering Research and Design*, *184*, 419–456. https://doi.org/10.1016/j.cherd.2022.06.028

Jian, X., Zhuang, X., Li, B., Xu, X., Wei, Z., Song, Y., & Jiang, E. (2018). Comparison of characterization and adsorption of biochars produced from hydrothermal carbonization and pyrolysis. *Environmental Technology and Innovation*, *10*, 27–35. https://doi.org/10.1016/j.eti.2018.01.004

Kambo, H. S., & Dutta, A. (2015). A comparative review of biochar and hydrochar in terms of production, physico-chemical properties and applications. In *Renewable and Sustainable Energy Reviews* (Vol. 45, pp. 359–378). Elsevier Ltd. https://doi.org/10.1016/j.rser.2015.01.050

Kannan, N., & Sundaram, M. M. (2001). *Kinetics and mechanism of removal of methylene blue by adsorption on various carbons-a comparative study*. www.elsevier.com/locate/dyepig

Karaca, S., Gürses, A., Açikyildiz, M., & Ejder (Korucu), M. (2008). Adsorption of cationic dye from aqueous solutions by activated carbon. *Microporous and Mesoporous Materials*, *115*(3), 376–382. https://doi.org/10.1016/j.micromeso.2008.02.008

Khan, I., Saeed, K., Zekker, I., Zhang, B., Hendi, A. H., Ahmad, A., Ahmad, S., Zada, N., Ahmad, H., Shah, L. A., Shah, T., & Khan, I. (2022). Review on Methylene Blue: Its Properties, Uses, Toxicity and Photodegradation. In *Water (Switzerland)* (Vol. 14, Issue 2). MDPI. https://doi.org/10.3390/w14020242

Kuang, Y., Zhang, X., & Zhou, S. (2020). Adsorption of methylene blue in water onto activated carbon by surfactant modification. *Water (Switzerland)*, *12*(2). https://doi.org/10.3390/w12020587

Kumar, K. V. (2006). Linear and non-linear regression analysis for the sorption kinetics of methylene blue onto activated carbon. *Journal of Hazardous Materials*, *137*(3), 1538–1544. https://doi.org/10.1016/j.jhazmat.2006.04.036

Lang, J., Matějová, L., Cuentas-Gallegos, A. K., Lobato-Peralta, D. R., Ainassaari, K., Gómez, M. M., Solís, J. L., Mondal, D., Keiski, R. L., & Cruz, G. J. F. (2021). Evaluation and selection of biochars and hydrochars derived from agricultural wastes for the use as adsorbent and energy storage materials. *Journal of Environmental Chemical Engineering*, *9*(5). https://doi.org/10.1016/j.jece.2021.105979

Le, P. T., Bui, H. T., Le, D. N., Nguyen, T. H., Pham, L. A., Nguyen, H. N., Nguyen, Q. S., Nguyen, T. P., Bich, N. T., Duong, T. T., Herrmann, M., Ouillon, S., & Le, T. P. Q. (2021). Preparation and Characterization of Biochar Derived from Agricultural By-Products for Dye Removal. *Adsorption Science and Technology*, *2021*. https://doi.org/10.1155/2021/9161904

Lin, L., Zhai, S. R., Xiao, Z. Y., Song, Y., An, Q. Da, & Song, X. W. (2013). Dye adsorption of mesoporous activated carbons produced from NaOH-pretreated rice husks. *Bioresource Technology*, *136*, 437–443. https://doi.org/10.1016/j.biortech.2013.03.048

Lonappan, L., Rouissi, T., Das, R. K., Brar, S. K., Ramirez, A. A., Verma, M., Surampalli, R. Y., & Valero, J. R. (2016). Adsorption of methylene blue on biochar microparticles derived from different waste materials. *Waste Management*, *49*, 537–544. https://doi.org/10.1016/j.wasman.2016.01.015

Mahapatra, U., Manna, A. K., & Chatterjee, A. (2022). A critical evaluation of conventional kinetic and isotherm modeling for adsorptive removal of hexavalent chromium and methylene blue by natural rubber sludge-derived activated carbon and commercial activated carbon. *Bioresource Technology*, *343*. https://doi.org/10.1016/j.biortech.2021.126135

Masoumi, S., Borugadda, V. B., Nanda, S., & Dalai, A. K. (2021). Hydrochar: A review on its production technologies and applications. In *Catalysts* (Vol. 11, Issue 8). MDPI. https://doi.org/10.3390/catal11080939

Montgomery, D. C. (2013). *Design and analysis of experiments* (2013th ed.).

Neolaka, Y. A. B., Riwu, A. A. P., Aigbe, U. O., Ukhurebor, K. E., Onyancha, R. B., Darmokoesoemo, H., & Kusuma, H. S. (2023). Potential of activated carbon from various sources as a low-cost adsorbent to remove heavy metals and synthetic dyes. *Results in Chemistry*, *5*. https://doi.org/10.1016/j.rechem.2022.100711

Nworie, *, Oti, W., & Nwali, A. (2019). REMOVAL OF METHYLENE BLUE FROM AQUEOUS SOLUTION USING ACTIVATED RICE HUSK BIOCHAR: ADSORPTION ISOTHERMS, KINETICS AND ERROR ANALYSIS. In *J. Chil. Chem. Soc* (Vol. 64, Issue 1).

Paluri, P., Khwaja, &, Ahmad, A., & Durbha, K. S. (n.d.). *Importance of estimation of optimum isotherm model parameters for adsorption of methylene blue onto biomass derived activated carbons: Comparison between linear and non-linear methods*. https://doi.org/10.1007/s13399-020-00867-y/Published

Pandey, D., Daverey, A., & Arunachalam, K. (2020). Biochar: Production, properties and emerging role as a support for enzyme immobilization. In *Journal of Cleaner Production* (Vol. 255). Elsevier Ltd. https://doi.org/10.1016/j.jclepro.2020.120267

Pellenz, L., de Oliveira, C. R. S., da Silva Júnior, A. H., da Silva, L. J. S., da Silva, L., Ulson de Souza, A. A., de Souza, S. M. de A. G. U., Borba, F. H., & da Silva, A. (2023). A comprehensive guide for characterization of adsorbent materials. In *Separation and Purification Technology* (Vol. 305). Elsevier B.V. https://doi.org/10.1016/j.seppur.2022.122435

Phuong, H. T., Uddin, M. A., & Kato, Y. (2015). Characterization of biochar from pyrolysis of rice husk and rice straw. *Journal of Biobased Materials and Bioenergy*, *9*(4), 439–446. https://doi.org/10.1166/jbmb.2015.1539

Pier Luca Maffettone. (2009). Metodi di Analisi dei Dati Sperimentali. In *Università di Napoli*. http://wpage.unina.it/p.maffettone/Didattica/Mads/Lezione7.pdf

Pirolisi e pirogassificazione delle biomasse. (2023, November 14). Università Degli Studi Di Cagliari.

Prof. M. Vanni. (2023). *Applied Physycal Chemistry*.

Quansah, J. O., Hlaing, T., Lyonga, F. N., Kyi, P. P., Hong, S. H., Lee, C. G., & Park, S. J. (2020). Nascent rice husk as an adsorbent for removing cationic dyes from textile wastewater. *Applied Sciences (Switzerland)*, *10*(10). https://doi.org/10.3390/app10103437

Rafatullah, M., Sulaiman, O., Hashim, R., & Ahmad, A. (2010). Adsorption of methylene blue on low-cost adsorbents: A review. In *Journal of Hazardous Materials* (Vol. 177, Issues 1–3, pp. 70–80). https://doi.org/10.1016/j.jhazmat.2009.12.047

Raja, P. M. V, & Barron, A. R. (2023). *PHYSICAL METHODS IN CHEMISTRY AND NANO SCIENCE*. https://LibreTexts.org

Revellame, E. D., Sharp, W., Hernandez, R., & Zappi, M. (2020). *Validation Method for Modeling Adsorption Kinetics using Pseudo First Order and Pseudo Second Order Rate Laws*.

Hagos F. M., Qian H., Di J., Shan S.,Yang R., Li Y., Gai X. (2022), Rice Husk Hydrochars Prepared with Different Posttreatment Methods for the Adsorption of Dyes and Antibiotics. In BioResources 17(1), 725-749, hhttps://doi.org/10.15376/biores.17.1.725-749

S, R., & P, B. (2019). The potential of lignocellulosic biomass precursors for biochar production: Performance, mechanism and wastewater application—A review. In *Industrial Crops and Products* (Vol. 128, pp. 405–423). Elsevier B.V. https://doi.org/10.1016/j.indcrop.2018.11.041

Senthil Kumar, P., Abhinaya, R. V., Gayathri Lashmi, K., Arthi, V., Pavithra, R., Sathyaselvabala, V., Dinesh Kirupha, S., & Sivanesan, S. (2011). Adsorption of methylene blue dye from aqueous solution by agricultural waste: Equilibrium, thermodynamics, kinetics, mechanism and process design. *Colloid Journal*, *73*(5), 651–661. https://doi.org/10.1134/S1061933X11050061

Sharma, P., Kaur, R., Baskar, C., & Chung, W. J. (2010). Removal of methylene blue from aqueous waste using rice husk and rice husk ash. *Desalination*, *259*(1–3), 249–257. https://doi.org/10.1016/j.desal.2010.03.044

Singh Karam, D., Nagabovanalli, P., Sundara Rajoo, K., Fauziah Ishak, C., Abdu, A., Rosli, Z., Melissa Muharam, F., & Zulperi, D. (2022). An overview on the preparation of rice husk biochar, factors

affecting its properties, and its agriculture application. In *Journal of the Saudi Society of Agricultural Sciences* (Vol. 21, Issue 3, pp. 149–159). King Saud University. https://doi.org/10.1016/j.jssas.2021.07.005

Spettrofotometria. (2023, November 14). Wikipedia. https://it.wikipedia.org/wiki/Spettrofotometria

Thompson Michael. (2008). *CHNS Elemental Analysers*. www.rsc.org/amc

Vadivelan, V., & Vasanth Kumar, K. (2005). Equilibrium, kinetics, mechanism, and process design for the sorption of methylene blue onto rice husk. *Journal of Colloid and Interface Science*, *286*(1), 90–100. https://doi.org/10.1016/j.jcis.2005.01.007

Wang, S., Zhu, Z. H., Coomes, A., Haghseresht, F., & Lu, G. Q. (2005). The physical and surface chemical characteristics of activated carbons and the adsorption of methylene blue from wastewater. *Journal of Colloid and Interface Science*, *284*(2), 440–446. https://doi.org/10.1016/j.jcis.2004.10.050

Wang, Y., & Liu, R. (2017). Comparison of characteristics of twenty-one types of biochar and their ability to remove multi-heavy metals and methylene blue in solution. *Fuel Processing Technology*, *160*, 55–63. https://doi.org/10.1016/j.fuproc.2017.02.019

Yagub, M. T., Sen, T. K., Afroze, S., & Ang, H. M. (2014). Dye and its removal from aqueous solution by adsorption: A review. In *Advances in Colloid and Interface Science* (Vol. 209, pp. 172–184). Elsevier. https://doi.org/10.1016/j.cis.2014.04.002

Zhou, F., Bi, H., & Huang, F. (2021). Ultra-large Specific Surface Area Activated Carbon Synthesized from Rice Husk with High Adsorption Capacity for Methylene Blue. *Wuji Cailiao Xuebao/Journal of Inorganic Materials*, *36*(8), 893–900. https://doi.org/10.15541/jim20200632